

MAGNUS III: Mild evolution of the total density slope in massive early-type galaxies since $z \sim 1$ from dynamical modeling of MUSE integral-field stellar kinematics

PRITOM MOZUMDAR ,^{1,*} MICHELE CAPPELLARI ,² CHRISTOPHER D. FASSNACHT ,³ AND TOMMASO TREU ,¹

¹*Department of Physics and Astronomy, University of California, Los Angeles, CA 90095, USA*

²*Sub-Dep. of Astrophysics, Dep. of Physics, University of Oxford, Denys Wilkinson Building, Keble Road, Oxford, OX1 3RH, UK*

³*Department of Physics and Astronomy, University of California, Davis, CA 95616, USA*

ABSTRACT

We investigate the total mass density slope evolution in massive early-type galaxies (ETGs) over the last 6.5 billion years ($0 < z < 0.75$). We perform a detailed dynamical analysis of approximately 200 ETGs spanning the redshift range $0.24 < z < 0.75$, utilizing spatially resolved stellar kinematics derived from high signal-to-noise ratio (S/N) MUSE-DEEP spectroscopy and surface brightness models from high-resolution HST imaging. We constrain mass distributions using the Jeans Anisotropic Modeling (JAM) technique coupled with Multi-Gaussian Expansion (MGE) method. To rigorously constrain evolutionary trends, we combine this intermediate-redshift dataset with a local ETG sample ($z \sim 0.05$) from the MaNGA survey. We adopt dynamical constraints for the local sample derived using an identical homogeneous methodology, ensuring a strictly consistent comparison. We found that the total density profiles of the intermediate-redshift ETG sample are approximately isothermal and exhibit a median mass-weighted total density slope, $\langle \gamma_T \rangle = 2.19 \pm 0.01$ at $\langle z \rangle = 0.44$, which is shallower than the local baseline of $\langle \gamma_T \rangle = 2.26 \pm 0.01$ at $\langle z \rangle = 0.04$. This structural shift corresponds to a redshift gradient of $d\gamma_T/dz \approx -0.20 \pm 0.03$, detected at $\sim 5\sigma$ significance. We demonstrate that this trend is robust against model assumptions and persists even when restricting the analysis to high-velocity dispersion systems ($\sigma_e > 150 \text{ km s}^{-1}$). Our findings are consistent with previous lensing-based studies and in tension with cosmological simulations. The observed steepening suggests that dissipative processes, such as gas-rich accretion and mergers, must play a non-negligible role in the late-stage assembly of massive ETGs.

Keywords: Galaxy evolution — total density slope — resolved kinematics — Jeans' anisotropic modeling

1. INTRODUCTION

Galaxies form within dark matter (DM) halos as baryonic matter cools and condenses at their centers (e.g., S. D. M. White & C. S. Frenk 1991). The combined distribution of baryonic and dark matter determines the total mass profile, which is effectively described by a power-law radial density distribution, $\rho(r) \propto r^{-\gamma_T}$ (in this work we adopt the convention $\gamma_T > 0$) (e.g. T. Treu & L. V. E. Koopmans 2002, 2004). The interplay between these components dictates the internal structure of galaxies, which evolves over cosmic time driven by physical processes such as mergers, gas accretion, and environmental interactions (e.g., T. Naab & J. P. Ostriker 2017). Consequently, the total density slope serves as a fundamental diagnostic for constraining the mechanisms of galaxy formation and evolution.

The assembly of the mass distribution within massive galaxies is theorized to proceed broadly in two phases (e.g., L. Oser et al. 2010; P. G. van Dokkum et al. 2015). During the first phase ($z \gtrsim 2$), cold gas collapses toward the center and triggers intense *in situ* star formation, causing the central region to become denser and the total density slope to steepen with decreasing redshift. Subsequently, as *in situ* star formation is quenched, the mass distribution evolves primarily through mergers and accretion (e.g., T. Naab et al. 2009; P. G. van Dokkum et al. 2010). In this second phase, two scenarios generally diverge based on the gas content of the interactions. Gas-poor (dry) minor mergers tend to deposit mass in the galaxy outskirts, causing the total density slope to become shallower over cosmic time (T. Naab et al. 2009; M. Hilz et al. 2013). Conversely, gas-rich (wet) mergers or accretion events can channel mass toward the central regions, maintaining or even steepening the density profile (J. E. Barnes & L. E. Hernquist 1991; P. F. Hopkins et al. 2009). Given that galaxies may experience a combination of these processes, the resulting mass assembly history is often complex. There-

* corresponding author:pmozumdar@astro.ucla.edu

fore, investigating the evolution of the total density slope since $z \sim 1$ is crucial for disentangling these mechanisms. In this context, massive early-type galaxies (ETGs) are of particular interest, as they represent the end-products of these evolutionary tracks and encapsulate the cumulative history of galaxy formation.

Cosmological simulations generally predict that the total mass density slope of massive ETGs evolves toward isothermality, converging to $\gamma_T \approx 2$ by the present epoch ($z = 0$). However, the predicted evolutionary pathways to this state differ significantly depending on the simulation suite. For instance, the IllustrisTNG simulations (A. Pillepich et al. 2018) suggest that the average slope decreases from $\gamma_T \approx 2.2$ at $z = 2$ to $\gamma_T \approx 2.0$ at $z = 0$, with mild evolution (i.e., $d\gamma_T/dz \sim 0$) below $z < 1$ (Y. Wang et al. 2019). Similarly, the Magneticum simulations (K. Dolag 2015) exhibit a flattening trajectory, with the slope decreasing from $\gamma_T \approx 2.3$ to $\gamma_T \approx 2.0$ between $z = 1$ and $z = 0$ (i.e., $d\gamma_T/dz > 0$) (R.-S. Remus et al. 2017). In contrast, the Horizon-AGN simulations (S. Peirani et al. 2019) predict a continuous steepening of the total density slope from $z = 2$ to $z = 0$, albeit still converging to an isothermal profile ($\gamma_T \approx 2.0$) at the present day (i.e., $d\gamma_T/dz < 0$). This diversity in predicted trends highlights the profound sensitivity of the total density slope to the specific implementation of sub-grid baryonic physics, such as gas cooling, stellar winds, and active galactic nucleus (AGN) feedback (Y. Wang et al. 2020; S. Mukherjee et al. 2021).

Observational studies in the local Universe ($z \sim 0$) consistently indicate that massive ETGs possess total density profiles that are, on average, slightly steeper than the isothermal prediction. M. Cappellari et al. (2015) analyzed a sample of 14 fast rotator ETGs from the ATLAS^{3D} survey (M. Cappellari et al. 2011) and found that their density profiles are consistent with a single power-law from $R_e/10$ to $4R_e$. They measured an average slope of $\gamma_T = 2.19 \pm 0.03$ with very small intrinsic scatter, which is significantly steeper than the isothermal value. Remarkably, this characteristic value of $\gamma_T \approx 2.2$ has been confirmed with high precision by subsequent studies using various samples and data qualities, demonstrating the robustness and reproducibility of this kind of measurements. For example, analyzing a sample of 142 ETGs from the ATLAS^{3D} survey with stellar velocity dispersion $\lg(\sigma_e/\text{km s}^{-1}) > 2.1$, A. Poci et al. (2017) found a median slope of $\gamma_T = 2.19 \pm 0.02$ with an intrinsic scatter of 0.17. Importantly, starting with A. Poci et al. (2017), subsequent studies (e.g. R. Li et al. 2019; K. Zhu et al. 2024) also revealed a clear break in $\lg(\sigma_e/\text{km s}^{-1}) \approx 2.1$ below which the total slope becomes less steep. Further supporting these results, S. Bellstedt et al. (2018) extended the analysis of M. Cappellari et al. (2015) using similar data for 21 fast rotators out to $4R_e$, measuring $\gamma_T = 2.25 \pm 0.05$. Simi-

larly, R. Li et al. (2019) utilized a sample of 2000 galaxies from the MaNGA survey (K. Bundy et al. 2015) to derive a median $\gamma_T = 2.24$ within $1R_e$ for ETGs with $\lg(\sigma_e/\text{km s}^{-1}) > 2$. More recently, using the final MaNGA sample of 10,000 galaxies, K. Zhu et al. (2024, fig. 8) measured $\gamma_T \approx 2.18$ within $1R_e$ for galaxies above a characteristic velocity dispersion of $\lg(\sigma_e/\text{km s}^{-1}) \gtrsim 2.2$. All of these studies consistently relied on the Jeans Anisotropic Modeling (JAM) approach (M. Cappellari 2008, 2020) to constrain the total density slope by fitting observed two-dimensional stellar kinematic maps.

Observational studies at intermediate redshifts also present a conflicting picture compared to theoretical predictions, with different methodologies yielding divergent evolutionary trends. Most studies utilizing strong gravitational lensing indicate that the total density slopes of massive ETGs were shallower in the past and have steepened over cosmic time (i.e., $d\gamma_T/dz < 0$). For instance, measurements of lens galaxies from the Lenses Structure and Dynamics (LSD) survey, Sloan Lens ACS Survey (SLACS), Strong Lenses in the Legacy Survey (SL2S), and BOSS Emission-Line Lens Survey (BELLS) consistently find that γ_T is systematically steeper at lower redshifts (e.g., L. V. E. Koopmans et al. 2006; M. W. Auger et al. 2010; A. J. Ruff et al. 2011; A. S. Bolton et al. 2012; A. Sonnenfeld et al. 2013; R. Li et al. 2018).

Distinct from both the lensing results and the simulation predictions, recent dynamical modeling studies do not detect evolution. C. Derkenne et al. (2021) and C. Derkenne et al. (2023), analyzing spatially resolved kinematics of quiescent galaxies at $z \sim 0.35$, suggest that the total density slope has remained constant relative to local baselines (i.e., $d\gamma_T/dz \approx 0$). In conclusion, there is potentially a three-way disagreement regarding the evolution of the total density slope in massive ETGs since $z \sim 1$: broadly, simulations predict a decrease, lensing suggests an increase, and stellar dynamics are consistent with stability. However, it is important to note that for both observational approaches, the available statistical samples of ETGs are relatively small beyond $z > 0.4$. Therefore, their uncertainties are relatively large and insufficient to detect mild evolution if present.

In this third paper of the MAGNUS ('MUSE-deep Analysis of Galaxy kinematics and dyNamical evolution across redShift') series, we aim to reach a conclusive observational answer. To meet this goal, we measure the total density slope for a substantial sample of more than 200 ETGs (hereafter the MAGNUS sample) at intermediate redshifts ($0.24 < z < 0.75$) and constrain the $\gamma_T - z$ relation over the range of $0 < z < 1$ by comparing these data with a statistically matched local ETG sample from the MaNGA survey (K. Bundy et al. 2015). We utilize the Jeans Anisotropic Mod-

eling (JAM) approach, a technique extensively validated in both local and intermediate-redshift studies (e.g., [M. Cappellari et al. 2015](#); [A. Poci et al. 2017](#); [J. van Hout et al. 2021](#); [C. Derkenne et al. 2021, 2023](#); [K. Zhu et al. 2023](#)). To robustly characterize the redshift evolution of γ_T , it is essential to utilize a statistically significant sample with comparable data quality distributed evenly across the redshift baseline, analyzed via a homogeneous methodology. This work satisfies these requirements, providing a complementary perspective to previous lensing and dynamical studies. Furthermore, to quantify potential systematics, we employ six distinct dynamical model variations, exploring different assumptions regarding the mass distribution and the orientation of the velocity ellipsoid (spherical versus cylindrical alignment). Finally, we contextualize our findings by comparing our measurements with other samples available in the literature.

The paper is organized as follows. In [section 2](#), we describe the sample selection and data extraction processes for both the MAGNUS and MaNGA datasets. [section 3](#) presents the theoretical framework of the Jeans Anisotropic Modeling (JAM) technique and the Multi-Gaussian Expansion (MGE) parameterization of surface brightness. This section also details the adopted dynamical models, the fitting methodology, and the measurement of the total density slope. In [section 4](#), we present the results and an analysis of systematic uncertainties for the MAGNUS and MaNGA samples. We compare our measurements with literature samples and discuss their physical implications in [section 5](#). Finally, we summarize our key conclusions in [section 6](#). Throughout this study, we assume a flat Λ CDM cosmology with $H_0 = 70.0 \text{ km s}^{-1} \text{ Mpc}^{-1}$ and $\Omega_m = 0.3$.

2. DATA

In the first paper of the MAGNUS series ([P. Mozumdar et al. 2025a](#), hereafter MAGNUS I), we introduced the sample and detailed the extraction of spatially resolved stellar kinematics and morphological properties from the MUSE DEEP data cubes. In this work, we utilize this sample along with the kinematic maps and photometric data products derived in MAGNUS I. Below, we provide a brief summary of the sample selection and the relevant data products utilized for the dynamical modeling.

2.1. MAGNUS sample

MUSE is an integral-field spectrograph mounted on the Very Large Telescope (VLT) of the European Southern Observatory (ESO). In its wide-field mode, the instrument provides a spatial sampling of $0.2''$ over a $1' \times 1'$ field-of-view (FOV), often assisted by an adaptive optics (AO) system ([R. Bacon et al. 2010](#)). It covers a wavelength range of $4800 - 9300 \text{ \AA}$ with a spectral sampling of 1.25 \AA , yielding an average spectral resolution of $R \sim 2000$. This corresponds to an

instrumental dispersion of $\sigma_{\text{inst}} \sim 65 \text{ km s}^{-1}$ at $\sim 5000 \text{ \AA}$. The MUSE-DEEP data release ([European Southern Observatory \(ESO\) 2017](#)) combines observations from single or multiple MUSE programs targeting specific sky locations into deep IFU data cubes, achieving significant effective exposure times. Leveraging these high quality data, MAGNUS I compiled a sample of 212 ETGs from 35 data cubes within the redshift range $0.24 < z < 0.75$, featuring spatially resolved stellar kinematics extending to several effective radii. For a detailed description of the selection process, we refer the reader to MAGNUS I.

The selected data cubes cover a diverse set of fields, including five of the six Frontier Fields galaxy clusters: Abell S1063, Abell 2744, Abell 370, MACS J0416, and MACS J1149 ([J. M. Lotz et al. 2017](#)). The sample also encompasses parts of the Hubble Ultra Deep Field (HUDF; [R. Bacon et al. 2017](#)) and the COSMOS field ([N. Scoville et al. 2007](#)). Additional well-known clusters and fields covered by the data set include Abell 1835, Abell 2895, the Bullet Cluster, MACS J0257, MACS J0940, MACS J1206, MACS J2129, MACS J2214, MS 0451-03, RX J1347-1145, RX J2129+0005, SDSS J1029+2623, and SMACS 2131. The complete list of target fields, corresponding ESO archive IDs, original MUSE program IDs, effective exposure times, number of selected galaxies per cube, and catalog references are reported in Table 1 of MAGNUS I. We note that several data cubes utilized in this study were previously analyzed by [C. Derkenne et al. \(2021\)](#) to measure the total density slopes of intermediate-redshift ETGs. However, due to distinct selection criteria, there is only a partial overlap ($\sim 20\%$) between the two ETG samples.

The MAGNUS sample consists primarily of massive, luminous ETGs. The integrated velocity dispersion, σ_e , spans a range of approximately $100 - 300 \text{ km s}^{-1}$ with a median of 180 km s^{-1} . The median surface brightness in the HST F814W band is $18.27 \text{ mag arcsec}^{-2}$, ranging from $16.62 - 20.34 \text{ mag arcsec}^{-2}$. In terms of physical size, the semi-major axis, R_e^{maj} ranges from 0.6 kpc to $\sim 10 \text{ kpc}$; the majority of the sample ($\sim 80\%$) lies between 1 and 4 kpc , with a median of 2.2 kpc . Similarly, the stellar mass, $\log_{10}(M_*/M_\odot)$, ranges from 10.5 to 12.0 , with a median value of 11.15 . The coordinates, redshifts, and other derived morphological and stellar population properties for individual galaxies are available in MAGNUS I.

2.2. Stellar kinematics and photometry

While MAGNUS I provides a detailed description of the derivation of the 2D kinematic maps and photometry, we summarize the key data reduction steps here. The MUSE-DEEP collection consists of reduced 3D data and variance cubes processed via the standard MUSE data reduction pipeline ([P. M.](#)

Weilbacher et al. 2020). This pipeline⁴ corrects for instrumental signatures and sky background, then resamples and combines observations into a final data cube. Subsequently, individual data cubes for each target galaxy were extracted from the parent MUSE-DEEP cubes.

To measure spatially resolved kinematics, we first isolated the target galaxy signal from the background. Spaxels exceeding a S/N threshold were selected, where the S/N for each spaxel was calculated as the mean value within the rest-frame wavelength range of $3990 - 4190$ Å. The selection threshold was determined for each galaxy, typically corresponding to a median S/N of ~ 1 per pixel (ranging from 0.5 to 5.5 depending on the depth of the observations). We then performed Voronoi binning on the selected spaxels using the VorBIN Python package (M. Cappellari & Y. Copin 2003). Given the varying data quality across the sample, we adopted target S/N values empirically for each galaxy, ranging from 5 to 25 per Å. This ensured that key absorption features remained measurable in the binned spectra while minimizing spatial over-smoothing. In general, we enforced a minimum target $S/N \geq 5$ for low-S/N galaxies to ensure the resulting Voronoi map contained at least ~ 10 spatial bins. For high-S/N galaxies, we utilized higher target thresholds to maximize spectral quality while limiting the total number of bins.

Using the derived Voronoi tessellation, spectra were co-added to produce a single high-S/N spectrum per bin. Stellar kinematics were extracted using the penalized pixel-fitting code pPXF (M. Cappellari 2017, 2023) within the rest-frame wavelength range of $3780 - 4600$ Å. The blue-side cutoff of this range was constrained by the instrument coverage and galaxy redshift, while the red-side cutoff was imposed to avoid contamination from strong sky lines beyond 8000 Å in the observed frame.

Using a high-S/N subset of the MAGNUS sample, S. Knabbel et al. (2025, hereafter KM25) demonstrated that defective stellar templates—such as those suffering from flux calibration errors or inaccurate telluric corrections—can introduce significant bias into kinematic measurements. Furthermore, independent analyses by both KM25 and P. Mozumdar et al. (2025c) identified template mismatch as the dominant source of systematic uncertainty in the stellar kinematics of ETGs. To mitigate these effects, we employed three distinct stellar template libraries: Indo-US (F. Valdes et al. 2004), MILES (A. Beifiori et al. 2011), and the X-shooter Spectral Library (XSL; K. Verro et al. 2022). For each library, we restricted our template selection to the ‘clean’ subsets identified by KM25, resulting in final libraries containing 989, 789, and 462 templates for Indo-US, MILES, and XSL, respectively.

To minimize bin-to-bin scatter, we did not fit the full ‘clean’ library to every spatial bin. Instead, for each galaxy and each library, we constructed an optimal template subset. This subset was generated by fitting the high-S/N central spectrum of the galaxy using the full clean library and retaining only those templates assigned non-zero weights in the fit. During the kinematic fitting process, we included additive and multiplicative Legendre polynomials of degree 4 and 2, respectively, to correct for the continuum shape. Following the methodology of KM25, the final mean velocity, \bar{v} , and velocity dispersion, $\bar{\sigma}_v$, along with the associated systematic ($\Delta\bar{\sigma}_v$) and statistical ($\delta\bar{\sigma}_v$) uncertainties, were defined as the equally weighted average of the measurements obtained from the three independent libraries. In this work, we employ both the spatially resolved kinematic maps and the integrated velocity dispersions (σ_e) extracted via this process. Visualizations of these kinematic maps and the corresponding HST image cutouts described below are available in MAGNUS I.

Individual galaxy cutouts, typically spanning dimensions of $10 - 15''$, were extracted from HST imaging covering the same fields as the MUSE-DEEP data cubes. We primarily utilized images taken with the F814W filter; in cases where F814W data were unavailable, we substituted observations in the F555W or F606W bands. A detailed summary of the archival HST data, including instrument setups, filters, and exposure times, is provided in Table 2 of MAGNUS I. For each cutout, the background level was estimated and subtracted. These sky-subtracted images served as inputs to model the surface brightness distribution as a series of 2D Gaussian profiles (see subsection 3.2), implemented using the MGEFit Python package (M. Cappellari 2002). For each galaxy, we utilized the local FWHM PSF estimates provided in the datacube headers rather than a single global value to account for the complex construction of the MUSE-DEEP mosaic. Since the final datacube is a co-addition of observations spanning multiple programs, epochs, and atmospheric conditions, the effective seeing varies significantly across the field of view. The list of the FWHM PSF used for the MAGNUS sample are available in P. Mozumdar et al. (2025b, hereafter MAGNUS II).

Previous studies have established that the total density slope strongly correlates with the integrated velocity dispersion (σ_e) below a specific threshold while the correlation is mild above this threshold (e.g., A. Poci et al. 2017; R. Li et al. 2019; S. Li et al. 2024). The observed trends suggest the γ_T flattens as σ_e decreases. A. Poci et al. (2017) and R. Li et al. (2019) identified this transition at approximately 100 km s $^{-1}$ using the ATLAS^{3D} and MaNGA samples, respectively. However, using the latest MaNGA data release, S. Li et al. (2024) recently suggested that for ETGs, this threshold may be closer to 150 km s $^{-1}$. To minimize σ_e as a confounding factor in the evolutionary analysis while maximizing sample statistics,

⁴ For more details, see <https://www.eso.org/rm/api/v1/public/releaseDescriptions/102>

we adopted a conservative lower limit of $\sigma_e \geq 100 \text{ km s}^{-1}$. This selection criterion reduces the final MAGNUS sample to 198 ETGs. We also explored the implications of a more stringent constraint ($\sigma_e > 150 \text{ km s}^{-1}$); while this stricter cut reduces the MAGNUS sample size by approximately 20%, the qualitative results regarding the density slope evolution remain unchanged (see [subsection 5.1](#)).

2.3. Comparison sample: MaNGA

The MaNGA survey provides spatially resolved spectral measurements for approximately 10,000 nearby galaxies in the redshift range $0.01 < z < 0.15$ ([K. Bundy et al. 2015](#)). The observations cover a spatial extent of up to 2.5 effective radii (R_e) ([D. A. Wake et al. 2017](#)). The spectroscopic data span a wavelength range of $\lambda = 3600 - 10000 \text{ \AA}$ with a spectral resolution of $R \approx 2000$, corresponding to an instrumental dispersion $\sigma_{\text{inst}} \approx 72 \text{ km s}^{-1}$ ([D. R. Law et al. 2016](#)). The final data cubes were generated from spectrophotometrically calibrated raw data using the MaNGA Data Reduction Pipeline (DRP; [D. R. Law et al. 2016](#)). To derive stellar kinematic maps, the data cubes were Voronoi-binned to a target S/N of 10 and fitted using pPXF. These steps were performed using the official MaNGA Data Analysis Pipeline (DAP; [K. B. Westfall et al. 2019](#)).

[K. Zhu et al. \(2023\)](#), hereafter DynPop I) conducted detailed dynamical modeling of these high-quality resolved kinematics by solving the axisymmetric Jeans equations using JAMPy Python package ([M. Cappellari 2008, 2020](#)). Their analysis employed four distinct mass models and two orientations of the velocity ellipsoid (cylindrically and spherically aligned), assuming a constant anisotropy in the ratio of radial-to-tangential velocity dispersion. Model parameters were constrained by comparing the observed second velocity moments, V_{rms} , to model predictions within a Bayesian framework. The JAM approach requires the surface brightness distribution of the galaxy to serve as the tracer density ζ and DynPop I utilized SDSS r -band images to model this distribution via the MGE formalism ([E. Emsellem et al. 1994](#); [M. Cappellari 2002](#)). For each model configuration, the mass-weighted total density slope was derived from the best-fit parameters.

In this work, we adopt an identical methodology for the MAGNUS sample, employing the MGE formalism to model the surface brightness (see [subsection 3.2](#)) and JAMPy for modeling the observed V_{rms} maps (see [subsection 3.1](#)). We utilize the same mass model parameterizations and velocity ellipsoid orientations, and measure γ_T as the mass-weighted average within one effective radius ($1R_e$), identical to the definition used in DynPop I. Given that the data reduction, analysis pipelines, and derivation techniques are consistent between the two datasets, we adopt the dynamical quantities reported by DynPop I and utilize the MaNGA dataset as our

primary comparison sample from the local Universe. We retrieved the relevant galaxy properties from the DynPop I catalog⁵, including redshifts, JAM model quality flags, integrated velocity dispersions (σ_e), and the mass-weighted total density slopes (γ_T) for the four model variants utilized in this study. Additionally, we obtained stellar mass measurements (M_*) for the MaNGA sample from [S. Lu et al. \(2023\)](#). These masses were derived by fitting FSPS ([C. Conroy et al. 2009](#); [C. Conroy & J. E. Gunn 2010](#)) stellar population templates, generated with a Salpeter Initial Mass Function (IMF; [E. E. Salpeter 1955](#)), to the integrated spectra within one effective radius using pPXF. The stellar masses of the MAGNUS sample were also measured in a similar fashion (for details check MAGNUS I).

The full MaNGA survey includes both early-type (e.g., E and S0) and late-type (e.g., spiral) galaxies. Since the MAGNUS sample is comprised exclusively of massive ETGs, we restricted the MaNGA comparison sample to ETGs only. The morphological selection criteria for these ETGs are detailed in MAGNUS II. To ensure a fair comparison, we required that the ETGs of the comparison sample have $\log(M_*/M_\odot) \geq 10.5$ and $\sigma_e \geq 100 \text{ km s}^{-1}$. These criteria correspond to the lower bounds of the MAGNUS sample for the respective properties. Furthermore, following the recommendations of DynPop I, we excluded galaxies with a quality flag (Qual) < 1 , as their derived dynamical quantities are considered unreliable due to poor data quality or model fits. These criteria yielded a final sample of 1,794 ETGs from the original 3,294 ETGs in the full MaNGA catalog. The median redshift of this MaNGA sample is $z \sim 0.06$. This MaNGA ETG sample effectively populates the epoch $z < 0.1$, serving as a complementary anchor to the MAGNUS data. Together, they provide an excellent opportunity to precisely constrain the evolution of γ_T since $z < 1$, leveraging a homogeneously analyzed dataset across cosmic time.

3. ANALYSIS METHOD

In this section, we present the dynamical modeling framework used to constrain the total mass distributions of the MAGNUS sample. We base our analysis on the JAM technique, which predicts the galaxy's spatially resolved second velocity moments (V_{rms}) by solving the axisymmetric Jeans equations. We first outline the mathematical formalism of these equations in [subsection 3.1](#). Since this approach requires an analytical parameterization of the stellar tracer density, we subsequently describe the MGE modeling of the observed surface brightness in [subsection 3.2](#). Finally, we detail the adopted mass models and anisotropy profiles ([subsection 3.3](#)), the Bayesian parameter estimation strategy ([subsection 3.4](#)), and the results of the dynamical modeling ([subsection 3.5](#)).

⁵ <https://zenodo.org/records/8381999>

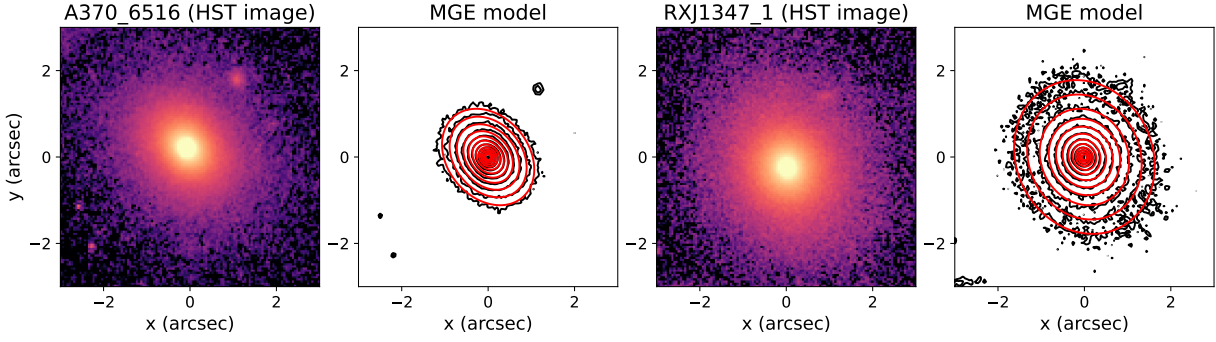


Figure 1. Representative MGE surface brightness models for the MAGNUS sample. The first and third panel display the sky-subtracted HST images. The second and fourth panel show the observed surface brightness isophotes (black contours) overlaid with the best-fit MGE model (red contours). Galaxy IDs are indicated above the corresponding HST images. The MGE models for the remaining galaxies in the sample are provided in Appendix C.

tion 3.4), and the methodology for deriving the mass-weighted total density slope (subsection 3.5).

3.1. Jeans anisotropic modelling

The orbital dynamics of a steady-state, collisionless stellar system are governed by the collisionless Boltzmann equation (CBE; [J. Binney & S. Tremaine 1987](#), Eq. 4-13b). This fundamental equation describes the evolution of the phase-space distribution function, $f(\mathbf{x}, \mathbf{v})$, within a total gravitational potential, Φ , and is expressed as:

$$\sum_{i=1}^3 \left(v_i \frac{\partial f}{\partial x_i} - \frac{\partial \Phi}{\partial x_i} \frac{\partial f}{\partial v_i} \right) = 0 \quad (1)$$

However, without further assumptions and simplifications, we can not practically use this equation. Assuming an axisymmetric stellar system (i.e., $\partial \Phi / \partial \phi = \partial f / \partial \phi = 0$), we obtain the following Jeans equations in cylindrical coordinates, (R, z, ϕ) ([J. Binney & S. Tremaine 1987](#), eq. 4-29 a,c) as

$$\begin{aligned} \frac{\zeta (\overline{v_R^2} - \overline{v_\phi^2})}{R} + \frac{\partial (\zeta \overline{v_R^2})}{\partial R} + \frac{\partial (\zeta \overline{v_R v_z})}{\partial z} &= -\zeta \frac{\partial \Phi}{\partial R}, \\ \frac{\zeta \overline{v_R v_z}}{R} + \frac{\partial (\zeta \overline{v_z^2})}{\partial z} + \frac{\partial (\zeta \overline{v_R v_z})}{\partial R} &= -\zeta \frac{\partial \Phi}{\partial z}, \end{aligned} \quad (2)$$

where ζ is the number density of the tracer population from which one measures the kinematics such that

$$\zeta \overline{v_k v_j} \equiv \int v_k v_j f \, d^3 v \quad (3)$$

This set of equations is general, relying only on the assumptions of steady-state equilibrium and axial symmetry. However, because the system is not closed—containing more unknowns than independent equations—additional constraints on the velocity ellipsoid are required to obtain a unique solution. Following [M. Cappellari \(2008\)](#), we assume that the velocity ellipsoid is aligned with the cylindrical coordinate

system (R, z, ϕ) , which implies that the off-diagonal moment vanishes (i.e., $\overline{v_R v_z} = 0$). Furthermore, we assume that the velocity anisotropy in the meridional plane, β_z , is constant, defined as:

$$\beta_z \equiv 1 - \frac{\overline{v_z^2}}{\overline{v_R^2}} = 1 - \frac{\sigma_z^2}{\sigma_R^2} = 1 - \frac{1}{b} \quad (4)$$

then the above equation set reduces to ([M. Cappellari 2008](#), eq. 8 and 9)

$$\begin{aligned} \frac{\zeta (b \overline{v_z^2} - \overline{v_\phi^2})}{R} + \frac{\partial (\zeta \overline{v_z^2})}{\partial R} &= -\zeta \frac{\partial \Phi}{\partial R} \\ \frac{\partial (\zeta \overline{v_z^2})}{\partial z} &= -\zeta \frac{\partial \Phi}{\partial z}, \end{aligned} \quad (5)$$

This equation set can be solved to yield unique solutions for $\overline{v_z^2}$ and $\overline{v_\phi^2}$ under the boundary condition $\zeta \overline{v_z^2} = 0$ as $z \rightarrow \infty$.

Similarly, if one assumes that the velocity ellipsoid is aligned with the spherical coordinates (r, θ, ϕ) and the velocity anisotropy is defined as

$$\beta_r \equiv 1 - \frac{\overline{v_\theta^2}}{\overline{v_r^2}} = 1 - \frac{\sigma_\theta^2}{\sigma_r^2} \quad (6)$$

then Jeans equations transform to the following equations ([M. Cappellari 2020](#), eq. 7)

$$\begin{aligned} \frac{\partial (\zeta \overline{v_r^2})}{\partial r} + \frac{(1 + \beta_r) \zeta (\overline{v_r^2} - \overline{v_\phi^2})}{r} &= -\zeta \frac{\partial \Phi}{\partial r} \\ (1 - \beta_r) \frac{\partial (\zeta \overline{v_r^2})}{\partial \theta} + \frac{(1 - \beta_r) \zeta (\overline{v_r^2} - \overline{v_\phi^2})}{\tan \theta} &= -\zeta \frac{\partial \Phi}{\partial \theta} \end{aligned} \quad (7)$$

As before these equations could be solved for unique solutions of $\overline{v_r^2}$ and $\overline{v_\phi^2}$ under the boundary condition $\zeta \overline{v_r^2} = 0$ as $r \rightarrow \infty$.

Consequently, for a given gravitational potential Φ , tracer density distribution ζ , and velocity anisotropy (β_z or β_r for cylindrically or spherically aligned ellipsoids, respectively), the intrinsic second velocity moments—either $(\overline{v_z^2}, \overline{v_\phi^2})$ or $(\overline{v_r^2}, \overline{v_\phi^2})$ —can be derived by solving respective equations. In practice, we adopt a specific mass density profile and anisotropy model corresponding to the chosen velocity ellipsoid orientation, while the tracer density is directly constrained by the galaxy’s observed surface brightness. The projected line-of-sight (LOS) second velocity moment is then calculated as:

$$\langle v_{\text{los}}^2 \rangle S(x, y) = \int_{-\infty}^{\infty} dz \zeta \langle v_z^2 \rangle. \quad (8)$$

where $S(x, y)$ is the surface density of the luminous dynamical tracer. The luminosity-weighted observed LOS velocity dispersion is given by

$$[\langle v_{\text{los}}^2 \rangle]_{\text{obs}} = \frac{\int_{\text{ap}} dx dy I \langle v_{\text{los}}^2 \rangle \otimes \text{PSF}}{\int_{\text{ap}} dx dy I \otimes \text{PSF}}, \quad (9)$$

where the symbol “ $\otimes \text{PSF}$ ” denotes a convolution with the PSF. The surface brightness profile, $I(x, y)$ of the dynamical tracer works as a substitute for the surface density $S(x, y)$, since they are related only by a constant factor that cancels out in this expression.

The model-predicted $\langle v_{\text{los}}^2 \rangle$ is directly comparable to the observed root-mean-square velocity, defined as $V_{\text{rms}} \equiv \sqrt{V^2 + \sigma_v^2}$, where V and σ_v represent the observed stellar velocity and velocity dispersion, respectively. By optimizing the agreement between the predicted and observed V_{rms} maps, we constrain the model parameters and derive the total density slope, γ_T . To perform this analysis, we utilize the **JAMPY** package, applying three distinct mass density models and assuming a spatially constant velocity anisotropy. To ensure the robustness of our derived quantities against structural assumptions, we adopt both cylindrically and spherically aligned velocity ellipsoid configurations, as the **JAMPY** framework accommodates both geometries. A fundamental prerequisite for this technique is an analytical description of the stellar tracer density, which serves as the input for the Jeans equations. To achieve this, we model the galaxy surface brightness using the MGE formalism, which we detail in the following section.

3.2. Multi-Gaussian expansion

We model the observed surface brightness distribution of each galaxy by performing a MGE fit to the high-resolution HST imaging. In this formalism, the surface brightness $\Sigma(x', y')$ is parameterized as a sum of N two-dimensional Gaussian components:

$$\Sigma(x', y') = \sum_{k=1}^N \frac{L_k}{2\pi\sigma_k^2 q'_k} \exp \left[-\frac{1}{2\sigma_k^2} \left(x'^2 + \frac{y'^2}{q'_k^2} \right) \right] \quad (10)$$

where L_k , σ_k , and q'_k represent the total luminosity, dispersion, and observed axial ratio of the k -th Gaussian component, respectively, and (x', y') define the coordinates on the sky plane. A primary advantage of this parameterization is its analytical tractability: operations such as convolution with a PSF and deprojection can be performed independently on each Gaussian component and linearly combined. While the deprojection of a 2D surface brightness profile into a 3D intrinsic density is mathematically non-unique, a unique solution can be obtained by imposing geometric constraints. Under the standard assumption of oblate axisymmetry, the 2D MGE models can be analytically deprojected. In cylindrical coordinates (R, z) , the intrinsic luminosity density is given by (M. Cappellari 2008, Eq. 8):

$$v(R, z) = \sum_{k=1}^N \frac{L_k}{\left(\sqrt{2\pi} \sigma_k \right)^3 q_k} \exp \left[-\frac{1}{2\sigma_k^2} \left(R^2 + \frac{z^2}{q_k^2} \right) \right] \quad (11)$$

where the luminosity L_k and dispersion σ_k are conserved from the 2D MGE, while q_k represents the intrinsic 3D axial ratio of the k -th Gaussian component, defined as:

$$q_k = \frac{\sqrt{q'_k^2 - \cos^2 i}}{\sin i}. \quad (12)$$

This deprojection depends on the galaxy inclination i (where $i = 90^\circ$ corresponds to an edge-on orientation). For the intrinsic model to be physically valid, the argument of the square root must be non-negative for all components. Consequently, the inclination is constrained by the flattest observed component, $q_{\min} = \min(q'_k)$, and the assumed intrinsic minimum axial ratio, $q_{\min} = \min(q_k)$. The inclination is related to these extrema via:

$$\tan^2 i = \frac{1 - q_{\min}^2}{q_{\min}^2 - q_{\min}^2}. \quad (13)$$

We generated the MGE models using the **MGEFit** Python package. First, we determined the galaxy centroid, position angle (PA), and ellipticity using the **FIND_GALAXY** routine. We then adapted our modeling approach based on the galaxy’s morphology. For galaxies without isophotal twists, we sampled the surface brightness using **SECTORS_PHOTOMETRY** and performed a regularized fit using the **MGE_FIT_SECTORS_REGULARIZED** routine. This sector-based sampling effectively mitigates local irregularities, such as dust lanes, while preserving the global isophotal structure and the regularization minimizes the number of Gaussian components and suppresses unphysical oscillations in the axial ratio distribution. Conversely, for galaxies exhibiting isophotal twists, we utilized **SECTORS_PHOTOMETRY_TWIST** followed by the **MGE_FIT_SECTORS_TWIST** routine to explicitly

Table 1. Summary of the dynamical model parameterizations employed in this study. For each model configuration, we list the free parameters and the corresponding prior distributions or boundary constraints applied during the Bayesian inference. The notations JAM_{cyl} and JAM_{sph} denote models assuming cylindrically and spherically aligned velocity ellipsoids, respectively.

Model	Fitted parameters with prior					
	q_{\min}	$\frac{\sigma_z}{\sigma_R}$ or $\frac{\sigma_\theta}{\sigma_r}$	$\log \left[\frac{M}{L} \right] \left[\frac{M_\odot}{L_\odot} \right]$	ρ_s	f_{DM}	γ
JAM_{cyl} : power-law	$[0.05, q'_{\min}]$	$\mathcal{N}(1.0, 0.07)$, $\frac{\sigma_z}{\sigma_R} \leq 1$	-	$[0, 4]$	-	$[1.5, 2.5]$
JAM_{sph} : power-law	$[0.05, q'_{\min}]$	$\mathcal{N}(1.0, 0.07)$	-	$[0, 4]$	-	$[1.5, 2.5]$
JAM_{cyl} : Stars + NFW	$[0.05, q'_{\min}]$	$\mathcal{N}(1.0, 0.07)$, $\frac{\sigma_z}{\sigma_R} \leq 1$	$[-2, 2]$	-	$[0, 1]$	-
JAM_{sph} : Stars + NFW	$[0.05, q'_{\min}]$	$\mathcal{N}(1.0, 0.07)$	$[-2, 2]$	-	$[0, 1]$	-
JAM_{cyl} : Stars + gNFW	$[0.05, q'_{\min}]$	$\mathcal{N}(1.0, 0.07)$, $\frac{\sigma_z}{\sigma_R} \leq 1$	$[-2, 2]$	-	$[0, 1]$	$[0, 1.6]$
JAM_{sph} : Stars + gNFW	$[0.05, q'_{\min}]$	$\mathcal{N}(1.0, 0.07)$	$[-2, 2]$	-	$[0, 1]$	$[0, 1.6]$

model the position angle variations. In all cases, we restricted the measurements to regions where the flux exceeded 2σ above the background. The intrinsic MGE models were analytically convolved with the PSF, derived from a non-saturated star in the same field, and optimized to match the observed surface brightness. Figure 1 shows the HST images for two representative galaxies from the sample, comparing the observed surface brightness contours with the best-fitting MGE model reconstructions. The MGE models for the remaining galaxies in the sample are provided in Appendix C.

While the absolute scaling of the luminous tracer is not strictly required to measure the mass-weighted slope of the total density profile, it is essential for constraining dynamical mass-to-light ratios (M/L). We normalized the total counts (C_k) of each Gaussian component to a peak surface brightness (I_k) via:

$$I_k = \frac{C_k}{2\pi\sigma_k^2 q_k}.$$

Simultaneously, the dispersion σ_k was converted from pixels to arcseconds using the instrument pixel scale. To recover the intrinsic luminosity density, we converted the MGE surface brightness profiles to AB magnitudes and corrected for Galactic extinction. We then applied a scaling factor of $(1+z)^3$ to account for cosmological surface brightness dimming and the bandwidth effects inherent to the AB system. Finally, to express the luminosity in solar units (L_\odot), we performed a K-correction (D. W. Hogg et al. 2002). We determined the reference solar magnitude for the specific HST bandpass used to observe the galaxy (typically F814W) using the `SPS_UTIL.SOLAR_MAG` routine from the pPXF package. This function computes the magnitude of the Sun as observed through a given filter at the specific redshift of the galaxy.

3.3. Mass models and kinematic anisotropy

3.3.1. Constant anisotropy

We adopted a spatially constant velocity anisotropy for both the cylindrically and spherically aligned velocity ellipsoid configurations, hereafter denoted as JAM_{cyl} and JAM_{sph} , respectively. The anisotropy parameter, β is parameterized by the ratio of the principal velocity dispersion components: σ_z/σ_R for the JAM_{cyl} case and σ_θ/σ_r for the JAM_{sph} case.

In our primary analysis, we imposed a Gaussian prior on these ratios, centered at isotropy: $\mathcal{N}(1.0, 0.07)$. For the JAM_{cyl} configuration, we additionally enforced an upper bound of unity ($\sigma_z/\sigma_R \leq 1$), as standard practice to avoid the inclination-anisotropy degeneracy of these models (M. Cappellari 2008, sec. 4.3), effectively adopting a half-Gaussian prior. This choice is motivated by two key factors. First, the intrinsic degeneracy between mass and anisotropy can lead to unphysical solutions when using uninformative (flat) priors, often resulting in models with negligible dark matter content compensated by extreme tangential anisotropy. Since the kinematic data alone are insufficient to break this degeneracy, an informed prior is required to exclude these non-physical regions of parameter space. Second, this prior is empirically grounded in high-resolution dynamical studies of local galaxies. Using Schwarzschild orbit-superposition models for a diverse sample of nearby fast- and slow-rotator ETGs, M. Cappellari (2026a) demonstrated that the radial anisotropy profiles are nearly isotropic ($\sigma_r/\sigma_{\text{tang}} \approx 1$). Accordingly, we centered our prior on isotropy (mean = 1.0). The adopted standard deviation of 0.07 corresponds to the scatter of the mean anisotropy $\sigma_r/\sigma_{\text{tang}}$ of the 13 galaxies in M. Cappellari (2026a, fig. 10), each first independently averaged over the range $R_e/30 < r < R_e$.

For comparison, we also tested a flat prior configuration following the approach of DynPop I, where the anisotropy ratios were bounded by $\mathcal{R}(q) < \sigma_z/\sigma_R < 1$ and $\mathcal{R}(q) < \sigma_\theta/\sigma_r <$

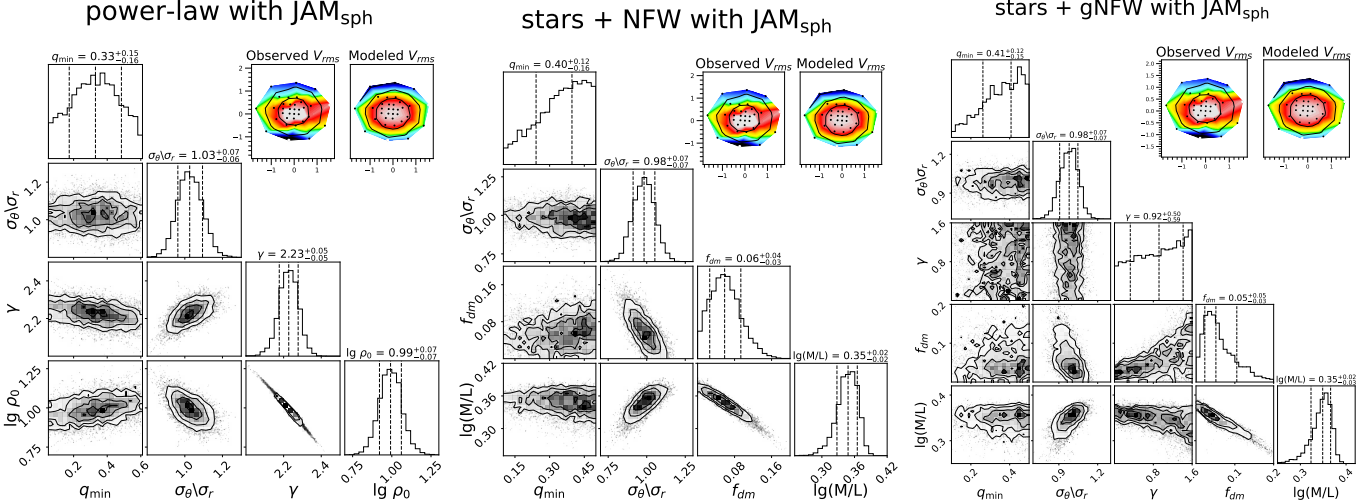


Figure 2. Posterior probability distributions for a representative galaxy (ID = ‘A2744_4423’) derived using three distinct mass models with spherical velocity ellipsoid alignment (JAM_{sph}). The panels correspond to the Power-Law (left), stars+NFW (middle), and stars+gNFW (right) parameterizations. The diagonal subplots display the marginalized 1D distributions, where vertical dashed lines indicate the median and the 16th/84th percentiles. The off-diagonal subplots show the covariances between model parameters. In the top-right corner of each panel display the observed root-mean-square velocity field (V_{rms}) compared with the prediction from the respective best-fit model. The observed and best-fit V_{rms} maps for the entire sample are presented in Appendix C.

2, with the lower bound defined as $\mathcal{R}(q) = \sqrt{0.3 + 0.7q}$ (where q is the intrinsic axial ratio). We found that while the choice of prior influences the specific best-fit anisotropy and mass parameters, it has a negligible impact on the derived total density slope. In Appendix A, we demonstrate that the γ_T values measured using these two different anisotropy priors are statistically consistent.

3.3.2. Power-law Total-density model

In this model, the total mass density distribution, $\rho(r)$, is parameterized as a single power-law profile of the form:

$$\rho(r) = \rho_s \left(\frac{r}{r_s} \right)^{-\gamma},$$

where r is the spherical radius, γ is the constant logarithmic slope of the density profile, and r_s serves as a fixed reference radius determining the normalization density ρ_s . This parameterization effectively captures the combined gravitational potential of the baryon-dominated center and the dark matter-dominated halo. Following previous dynamical studies (e.g., M. Cappellari et al. 2013a; S. Bellstedt et al. 2018; C. Derkenne et al. 2021), we fixed the reference radius to $r_s = 20$ kpc, as this parameter has a negligible impact on the dynamical analysis. Consequently, this model comprises four free parameters: (1) $\frac{\sigma_z}{\sigma_R}$ for JAM_{cyl} case (or $\frac{\sigma_\theta}{\sigma_r}$ for JAM_{sph}), (2) the intrinsic axial ratio (q_{min}) of the flattest gaussian in the MGE, (3) the total density slope (γ), and (4) the density normalization (ρ_s).

For this and all subsequent models, the analytic 1D mass density profiles were converted into gravitational potentials by fitting with an MGE using the `MGE_FIT_1D` procedure in

the `MGEFit` package, enabling computation of the model-predicted second velocity moments via the JAM framework.

3.3.3. Composite model: Stars with NFW dark halo

This composite model offers greater flexibility than the single power-law profile by explicitly decomposing the total mass distribution into stellar and dark matter components. The intrinsic stellar mass density was derived by scaling the MGE luminosity density with a constant dynamical mass-to-light ratio, M/L , thereby assuming that the stellar mass distribution strictly traces the light with no radial gradients in the stellar population. The dark matter component is parameterized as a spherical halo following the Navarro-Frenk-White (NFW) profile (J. F. Navarro et al. 1996), defined as:

$$\rho_{DM}(r) = \rho_s \left(\frac{r}{r_s} \right)^{-1} \left(\frac{1}{2} + \frac{1}{2} \frac{r}{r_s} \right)^{-2},$$

where r denotes the spherical radius. In this specific parameterization, ρ_s represents the characteristic density at the break radius, r_s (i.e., $\rho_{DM}(r_s) = \rho_s$). Following previous dynamical modeling studies of massive ETGs, we fixed the break radius to $r_s = 20$ kpc (e.g. M. Cappellari et al. 2015; A. Poci et al. 2017; S. Bellstedt et al. 2018; C. Derkenne et al. 2021, 2023). Systematic tests by S. Bellstedt et al. (2018) demonstrated that leaving the break radius as a free parameter yields total density slopes consistent with those derived using a fixed 20 kpc value. Furthermore, C. Derkenne et al. (2023) showed that while adopting a significantly smaller break radius (~ 10 kpc) can artificially bias the results toward steeper slopes, increasing r_s beyond 20 kpc has no significant effect on the derived parameters.

While the halo normalization is formally set by ρ_s , this parameter is degenerate with the stellar mass. To facilitate robust parameter estimation, we re-parameterize the normalization using the dark matter fraction, f_{DM} (calculated within the effective radius). This approach allows us to impose precise physical bounds ($0 < f_{\text{DM}} < 1$) and sample the dark matter content more intuitively. The reduced covariance also allow for a more efficient sampling of the model posterior during the MCMC. Consequently, this model comprises four free parameters: (1) $\frac{\sigma_z}{\sigma_R}$ for JAM_{cyl} case (or $\frac{\sigma_\theta}{\sigma_r}$ for JAM_{sph}), (2) the minimum intrinsic axial ratio (q_{\min}), (3) the stellar mass-to-light ratio (M/L), and (4) the dark matter fraction (f_{DM}).

3.3.4. Composite model: Stars with gNFW dark halo

Finally, to allow for a more complex interplay between dark and baryonic matter, we adopt a composite model utilizing a generalized NFW (gNFW; J. S. B. Wyithe et al. 2001) halo profile. We still assume no M/L gradient for the stars, identical to the NFW model described above. However, unlike the standard NFW halo which enforces a fixed inner slope ($\gamma = 1$), the gNFW profile treats the inner logarithmic density slope (γ) as a free parameter. This added flexibility enables the model to account for the dynamical response of the dark matter halo to baryonic assembly processes, such as adiabatic contraction (which steepens the profile; e.g. G. R. Blumenthal et al. 1986; O. Y. Gnedin et al. 2004) or feedback-driven expansion (which flattens it; e.g. F. Governato et al. 2010). The dark matter density distribution is described as:

$$\rho_{\text{DM}}(r) = \rho_s \left(\frac{r}{r_s} \right)^{-\gamma} \left(\frac{1}{2} + \frac{1}{2} \frac{r}{r_s} \right)^{\gamma-3},$$

where the standard NFW profile is recovered for $\gamma = 1$. Similar to the NFW model, we fixed the break radius to $r_s = 20$ kpc and constrained the halo density normalization, ρ_s , via the dark matter fraction (f_{DM}). Consequently, this model depends on five free parameters: (1) $\frac{\sigma_z}{\sigma_R}$ for JAM_{cyl} case (or $\frac{\sigma_\theta}{\sigma_r}$ for JAM_{sph}), (2) the minimum intrinsic axial ratio (q_{\min}), (3) the stellar mass-to-light ratio (M/L), (4) the dark matter fraction (f_{DM}), and (5) the inner dark matter slope (γ).

For all dynamical models employed in this study, we assumed a central supermassive black hole mass of zero. Given the redshift range and spatial resolution of our data, the sphere of influence of the central black hole is unresolved and thus has a negligible effect on the global kinematic fit. A summary of the adopted models, including the parameter priors and boundaries, is presented in [Table 1](#).

3.4. Fitting procedure

The parameter estimation is performed in two stages. First, we employed an iterative outlier-rejection scheme to identify and exclude spurious Voronoi bins. We fitted a preliminary

Mass-Follows-Light (MFL) model with cylindrical alignment (JAM_{cyl}) to the observed kinematics, utilizing the non-linear least-squares routine `SCIPY.OPTIMIZE.LEAST_SQUARES`. The model has three free parameters: the stellar mass-to-light ratio (M/L), $\frac{\sigma_z}{\sigma_R}$, and the minimum intrinsic axial ratio (q_{\min}). At each iteration, we computed the logarithmic residuals between the data and model, and quantified the scatter of these residuals (σ_{scatter}) using a robust bi-weight estimator (D. C. Hoaglin et al. 1983). Any Voronoi bin with an absolute residual exceeding $3\sigma_{\text{scatter}}$ was flagged as an outlier and excluded from the next iteration. This process was repeated until convergence, defined as the point where no new bins were rejected. To ensure consistency, the final mask of valid bins was applied uniformly across all subsequent dynamical model fits.

Next, we utilized a Bayesian inference framework to constrain the parameters of the six dynamical models and quantify their uncertainties. We sampled the posterior probability distributions using the Affine Invariant Markov chain Monte Carlo (MCMC) ensemble sampler implemented in the `EMCEE` Python package (D. Foreman-Mackey et al. 2013). The posterior probability of the model parameters θ , conditioned on the observed data D , is given by Bayes' theorem:

$$P(\theta | D) \propto P(D | \theta)P(\theta)$$

where $P(\theta)$ represents the prior probability and $P(D | \theta)$ is the likelihood function. Assuming Gaussian uncertainties for the kinematic measurements, the likelihood is proportional to $\exp(-\chi^2/2)$, with the χ^2 statistic defined as:

$$\chi^2 = \sum_j \left(\frac{\sqrt{v_{\text{los},j}^2} - V_{\text{rms},j}}{\varepsilon_{V_{\text{rms},j}}} \right)^2$$

Here, $\sqrt{v_{\text{los},j}^2}$ denotes the model-predicted line-of-sight RMS velocity, while $V_{\text{rms},j}$ and $\varepsilon_{V_{\text{rms},j}}$ represent the observed RMS velocity and its associated measurement uncertainty in the j -th Voronoi bin, respectively. The summation extends over all spatial bins retained after the outlier-rejection phase.

To sample the parameter space, we deployed 20 independent walkers evolving for 1,000 steps, generating a total of 20,000 posterior samples for each model. As discussed in [subsection 3.3](#), we applied the informative Gaussian priors to the anisotropy parameters, while adopting flat (uniform) priors for all other parameters within the physical boundaries specified in [Table 1](#). [Figure 2](#) displays representative corner plots showing the posterior distributions for three distinct JAM models fitted to the same galaxy.

3.5. Measuring dynamical quantities

From the posterior distributions of the model parameters, we derived the total enclosed mass, $M_{\text{T}}(< R_e)$, and the

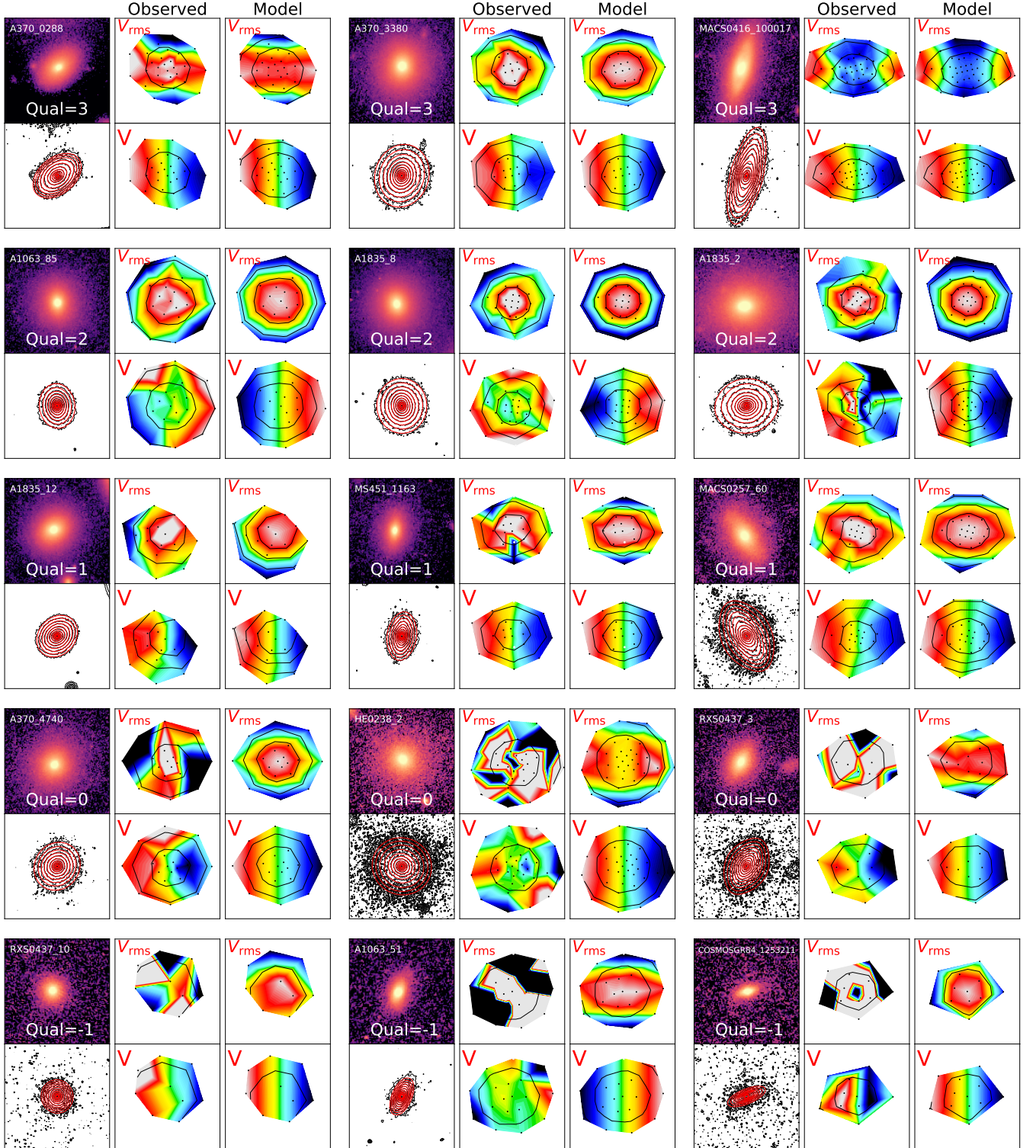


Figure 3. Example of visual assessment of the dynamical model fit quality. We present three galaxies for each quality class (defined in subsection 4.1). Each block of two rows corresponds to a specific quality class, displaying three galaxies arranged side-by-side. For an individual galaxy, the top row shows the HST image (labeled with the Galaxy ID and Quality flag), followed by the observed and modeled root-mean-square velocity (V_{rms}) maps. The bottom row displays the MGE fit, where black and red contours indicate the observed and modeled isophotes, respectively, followed by the observed and predicted mean velocity (V) fields. In the observed and fitted kinematic maps, the overlaid black contours trace the observed and modeled surface brightness distribution.

mass-weighted total density slope, γ_T , within the effective radius. The total mass was calculated analytically using the `MGE_RADIAL_MASS` routine within the `JAMPy` package. Following [A. A. Dutton & T. Treu \(2014\)](#), we defined γ_T as the mass-weighted average of the local logarithmic slope within R_e . This definition is robust against local fluctuations in the density profile and is expressed as:

$$\gamma_T = \frac{1}{M_T()} \int_0^{R_e} -\frac{d \log \rho_T}{d \log r} 4\pi r^2 \rho_T(r) dr = 3 - \frac{4\pi R_e^3 \rho_T(R_e)}{M_T()},$$

where $\rho_T(r)$ represents the spherically averaged total density profile. We computed this quantity analytically, on spherical shells, from the axisymmetric MGE densities utilizing the `MGE_WEIGHTED_SLOPE` function in `JAMPy`.

To quantify the statistical uncertainties, we generated posterior distributions for γ_T by propagating the MCMC samples from each JAM model. We first discarded the initial 100 steps (2,000 samples) as a burn-in phase to ensure chain convergence. The remaining chains were thinned by a factor of 2 to reduce autocorrelation, yielding a final set of 9,000 independent samples per model. We adopted the median of these derived distributions as our fiducial measurement, with the 16th and 84th percentiles defining the 1σ confidence intervals. This approach is superior to relying on a single best-fit solution or the medians of marginalized parameters, as it explicitly propagates the intrinsic covariances between model parameters into the final physical quantities.

4. RESULTS

In this section, we present the measurements of the total density slope derived from our dynamical analysis. We begin by assessing the reliability of the dynamical model fits and defining our quality control criteria in [subsection 4.1](#). We then evaluate the internal consistency of our measurements across different model assumptions (mass profiles and velocity ellipsoid alignments) in [subsection 4.2](#) and explore potential correlations with global galaxy properties in [subsection 4.3](#). The core evolutionary trends are presented in [subsubsection 4.4.1](#) for the MAGNUS sample alone, and in [subsubsection 4.4.2](#) for the combined dataset incorporating the local MaNGA baseline.

4.1. *Quality of dynamical modeling fits*

While the JAM formalism provides a robust method for recovering galaxy mass profiles, the reliability of the derived parameters depends critically on the model's ability to reproduce the observed kinematics. We found that in cases of low S/N or complex kinematic substructures, the models occasionally failed to converge to a physically meaningful solution. To quantify this, we performed a visual quality-of-fit assessment by comparing the observed velocity (V) and second moment (V_{rms}) maps with the model predictions. We observed a high degree of consistency across the different mass

models; specifically, if the data quality precluded a good fit for the most flexible model configuration (stars + gNFW with JAM_{sph}), the simpler model variants invariably failed as well. Consequently, we adopted the stars + gNFW with JAM_{sph} fit as a representative proxy to classify the entire sample. We used a classification scheme where a quality flag (Qual) ranging from -1 to 3 was assigned to each galaxy based on the following criteria (e.g. [M. Cappellari et al. 2013a](#); [A. Poci et al. 2017](#); [K. Zhu et al. 2023](#)):

- **Qual = 3 (Excellent):** The model accurately reproduces both the observed V and V_{rms} maps. These galaxies are typically fast rotators with best quality data.
- **Qual = 2 (Good):** The predicted V_{rms} maps are of high quality, comparable to Qual = 3, but the fit to the mean velocity field (V) shows minor discrepancies. This category is dominated by slow rotators, where the velocity maps lack clear rotation signal and thus intrinsically harder to constrain, yet the global mass distribution remains well-recovered via V_{rms} .
- **Qual = 1 (Marginal):** The modeled V_{rms} maps are less accurate than the higher quality tiers but still capture the essential radial and azimuthal features of the observed data. In these cases, the V maps are generally well-recovered, except for slow rotators.
- **Qual = 0 (Poor):** The model fails to capture the structure of the observed V_{rms} map, even if the V field is reasonably fitted.
- **Qual = -1 (Unreliable):** The model fails to reproduce both the observed V or V_{rms} maps significantly.

[Figure 3](#) presents representative examples of galaxies from each quality group. Of the 198 galaxies in the MAGNUS sample, 168 ($\sim 85\%$) were assigned a fit quality of $Qual \geq 1$. As the dynamical constraints for $Qual < 1$ galaxies are deemed unreliable, we excluded these 30 objects from all subsequent analyses. This exclusion is justified not only visually but also statistically. We found that the median relative uncertainty on the derived total density slope (γ_T) for the excluded group ($Qual < 1$) is approximately double that of the retained sample. For instance, using the stars+gNFW with JAM_{sph} model, the median uncertainty for $Qual \geq 1$ galaxies is 2.68% (with a standard deviation of 3.27%), compared to 4.85% (standard deviation 4.11%) for the low-quality fits. Furthermore, the retained sample typically exhibits reduced χ^2 values in the range of 1 – 2, confirming that the models provide a statistically satisfactory description of the data.

4.2. *Consistency of Total Density Slope Measurements*

To assess the robustness of our results, we first examined the sensitivity of the measured γ_T to the assumed geometry

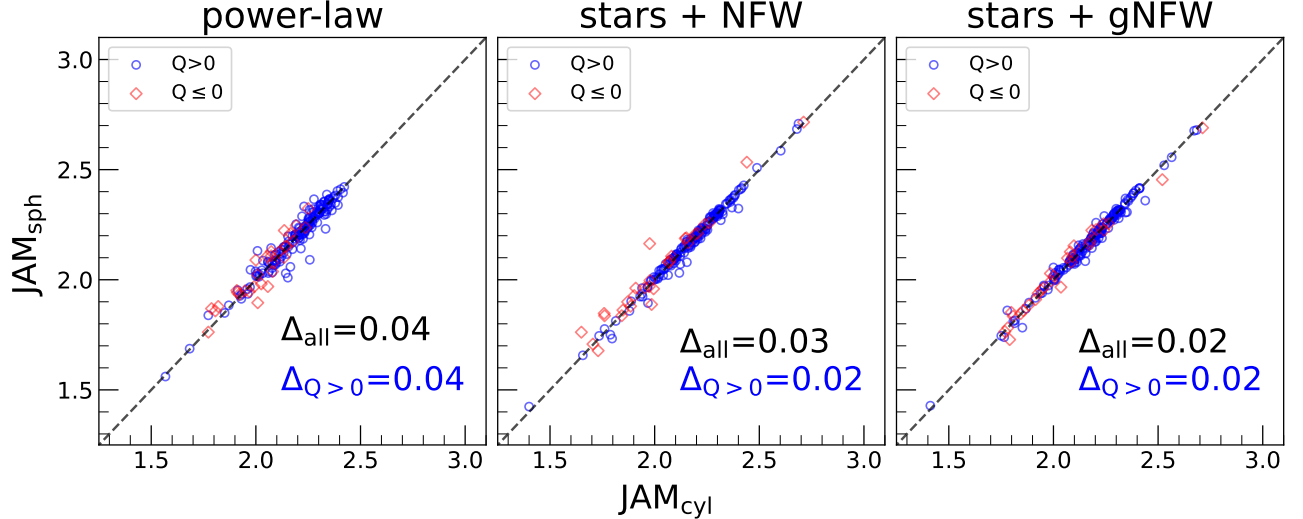


Figure 4. Comparison of the total density slope (γ_T) measured using cylindrically (JAM_{cyl}) versus spherically (JAM_{sph}) aligned velocity ellipsoids for same mass model. The three panels correspond to the power-Law (left), stars + NFW (middle), and stars + gNFW (right) mass models. Galaxies with reliable kinematic fits ($Qual > 0$) are plotted as blue circles, while those with poor or unreliable fits ($Qual \leq 0$) are marked with red diamonds. The black dashed line indicates the one-to-one relation. The intrinsic scatter (Δ) between the two orientations, quantified using the LrsFitt package, is reported within each panel for both the full sample and the high-quality subset.

of the velocity ellipsoid. In Figure 4, we compare the slopes derived using the same mass model but with different alignments (JAM_{cyl} vs. JAM_{sph}). We found that, for a fixed mass profile, the derived γ_T values are highly consistent regardless of the geometric assumption. This robustness is expected, as the imposition of a nearly isotropic prior on the velocity anisotropy effectively minimizes the impact of the velocity ellipsoid orientation. Using the LrsFitt Python package (M. Cappellari et al. 2013a) with a 5σ outlier clipping, we measured the intrinsic scatter (Δ) between the two orientations. For the power-law model, we found a negligible scatter of $\Delta = 0.04$, which remained constant even after excluding unreliable fits ($Qual \leq 0$). Similarly, the stars + NFW and stars + gNFW models exhibited very tight correlations with scatters of $\Delta = 0.03$ and $\Delta = 0.02$, respectively (improving to $\Delta = 0.02$ for the NFW case when excluding low-quality fits). These comparisons demonstrate that our measurements of γ_T are largely independent of the assumed velocity ellipsoid orientation.

Next, we evaluated the consistency of γ_T across the different mass density parameterizations (power-Law, stars + NFW, and stars + gNFW), considering only galaxies with reliable fits ($Qual \geq 1$). As shown in Figure 5, the NFW and gNFW models are in excellent agreement with each other, exhibiting a minimal intrinsic scatter of $\Delta = 0.02$ for both velocity ellipsoid configurations. This tight correlation is unsurprising given that the gNFW profile is a generalization of the NFW form; however, it confirms that the additional freedom in the inner halo slope of the gNFW model does not introduce significant instability in the recovered total density slope.

In contrast, the single power-law models exhibit larger scatter relative to the composite models, though with no systematic bias. Approximately 50% of the sample yields γ_T values agreeing within 1%, while deviations in the remainder are bidirectional. This increased dispersion most probably stems from the structural rigidity of the power-law parameterization, which enforces self-similarity unlike the radially varying slopes of the composite models. Nevertheless, the measurements remain statistically compatible, with an intrinsic scatter of ≈ 0.11 , consistent with typical measurement uncertainties.

4.3. Correlations with Galaxy Properties

Previous studies have suggested that the total density slope of early-type galaxies (ETGs) correlates with structural properties such as mass, size, and velocity dispersion. M. W. Auger et al. (2010) reported weak correlations between the slope and the effective radius (R_e) as well as the central mass density, while A. Sonnenfeld et al. (2013) found that the total slope correlates most strongly with the surface mass density. Early lensing-based results showed only weak trends, largely because lens galaxies preferentially inhabit the high- σ_e regime, where galaxies tend to have similar density slopes. However, when lower-mass systems from dynamical studies were included, significantly stronger correlations emerged. In particular, the strongest trend was found between the total density slope γ_T and the stellar velocity dispersion σ_e , or equivalently, a near constancy of the slope along lines of constant M/R_e (M. Cappellari 2016, fig. 22c; A. Poci et al. 2017). Extensions to dynamical samples from the MaNGA survey, spanning all morphological types and a wide range of

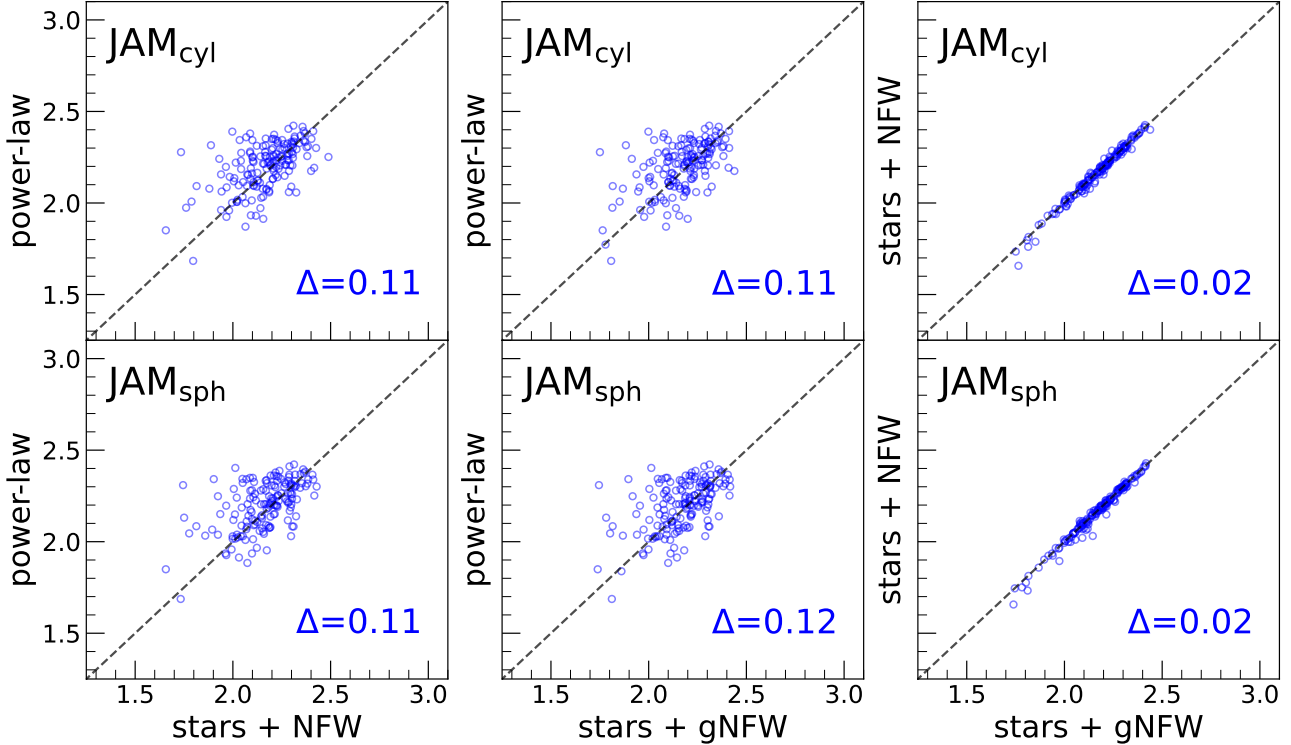


Figure 5. Comparison of the total density slopes (γ_T) derived using same velocity ellipsoid orientation but different mass models. This comparison is restricted to the subsample with reliable dynamical models ($\text{Qual} \geq 1$). The top and bottom rows display results for the cylindrically (JAM_{cyl}) and spherically (JAM_{sph}) aligned velocity ellipsoids, respectively. The black dashed line marks the one-to-one relation, and the intrinsic scatter (Δ) between the models is indicated in each panel.

stellar ages, further demonstrated that although σ_e remains the best predictor of the total density slope, at fixed σ_e the slope decreases systematically for younger galaxies (R. Li et al. 2019; K. Zhu et al. 2024, fig. 8). More recently, C. Derkenne et al. (2023) reported an additional dependence of γ_T on environment.

Quantifying these dependencies is critical for evolutionary studies, as any apparent redshift evolution in γ_T could potentially arise from the selection of galaxy samples with different structural properties across cosmic time. We examined the MAGNUS sample for linear relations between γ_T and four key parameters: central velocity dispersion (σ_e), effective radius (R_e), stellar mass (M_*), and surface mass density (Σ_*), defined as $\Sigma_* = \frac{M_*}{2\pi R_e^2}$. For this analysis, we utilized the γ_T measurements derived from the fiducial stars+gNFW with JAM_{sph} model. We parameterized the scaling relations as linear functions of the form $\gamma_T(x) = a + b_0(x - x_0)$, where a is the intercept, $b_0 = d\gamma_T/dx$ represents the slope (gradient), and x_0 is the sample median of the logarithmic galaxy property (x) under consideration. We performed robust linear fits using the LtsFit package, which provides the best-fit coefficients, intrinsic scatter, Pearson correlation coefficients (r), and associated p -values. The results are displayed in Figure 6.

Overall, we find that the total density slope of MAGNUS sample exhibits negligible to weak correlations with these global properties. For velocity dispersion, we measured a slope of $d\gamma_T/d\log_{10} \sigma_e = 0.07 \pm 0.10$ with an intrinsic scatter of 0.14. The Pearson coefficient ($r = 0.03$, $p = 0.72$) indicates no statistically significant correlation. Similarly, we found no significant trend with stellar mass, $d\gamma_T/d\log_{10} M_* = -0.07 \pm 0.03$. The effective radius (R_e) shows a weak negative correlation ($d\gamma_T/d\log_{10} R_e = -0.10 \pm 0.05$), suggesting that more compact galaxies tend to have slightly steeper density slopes, although the significance is marginal. Finally, the dependence on surface mass density is also statistically insignificant, with a gradient of $d\gamma_T/d\log_{10} \Sigma_* = 0.03 \pm 0.04$ ($p = 0.43$).

These observed trends remain consistent across other variations of our composite mass models. However, γ_T derived from power-law models exhibits a relatively stronger dependence on σ_e and Σ_* , while trends with R_e and M_* remain at the same level as the composite models. For velocity dispersion, the measured slope from the power-law + JAM_{cyl} model is $d\gamma_T/d\log_{10} \sigma_e = 0.35 \pm 0.08$ with an intrinsic scatter of 0.12. Although the Pearson coefficient ($r = 0.05$, $p = 0.5$) indicates no statistically significant correlation within the MAGNUS sample, the gradient is noticeably steeper. For the power-law + JAM_{sph} model, this

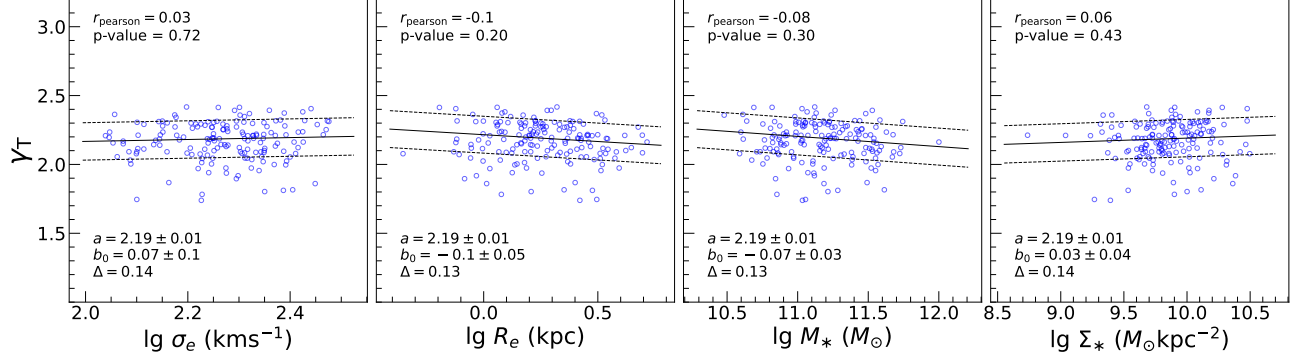


Figure 6. Correlations between the total density slope (γ_T) from stars+gNFW with JAM_{sph} model and global galaxy properties for the MAGNUS sample. From left to right, the panels display the dependence of γ_T on central velocity dispersion (σ_e), effective radius (R_e), stellar mass (M_*), and surface mass density (Σ_*). The black solid line represents the robust best-fit linear relation $\gamma_T = a + b(x - x_0)$, where x denotes the logarithmic galaxy property corresponding to each panel. The dashed lines indicate the 1σ intrinsic scatter. The best-fit coefficients and intrinsic scatter are reported at the bottom of each panel, with the Pearson correlation coefficient (r_{pearson}) and corresponding p -value displayed at the top.

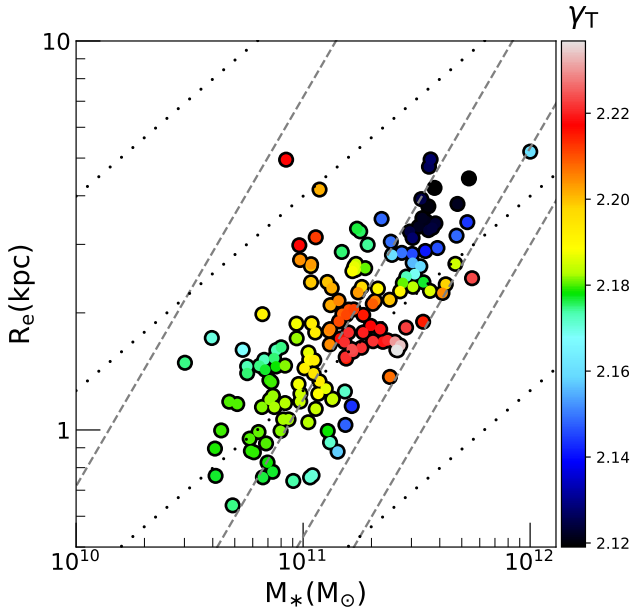


Figure 7. Distribution of the total density slope, γ_T , in the stellar mass–size plane. The γ_T values are derived using the fiducial stars+gNFW with JAM_{sph} model. The color map displays values smoothed via the Locally Weighted Regression method using the LOESS package (M. Cappellari et al. 2013b) to recover the underlying mean trends by suppressing intrinsic scatter. The gray dashed lines indicate contours of constant velocity dispersion ($\sigma_e = 100, 200, 300, \text{ and } 400 \text{ km s}^{-1}$, increasing from left to right), while the black dotted lines denote contours of constant surface mass density ($\Sigma_e = 10^8, 10^9, 10^{10}, \text{ and } 10^{11} M_\odot \text{kpc}^{-2}$, increasing from top to bottom).

gradient is $d\gamma_T/d\log_{10} \sigma_e = 0.15 \pm 0.09$, though still statistically insignificant ($r = 0.09$, $p = 0.26$). For surface mass density, both power-law models yield a gradient of $d\gamma_T/d\log_{10} \Sigma_* \approx 0.13 \pm 0.03$ ($p = 0.1$).

We also performed an identical analysis on the full local MaNGA comparison sample. While the full sample showed similarly weak trends, the MaNGA primary sample (see subsubsection 4.4.2) exhibits a relatively stronger trend with σ_e , comparable to the gradient observed in the MAGNUS power-law models. This trend is also visible in Fig. 11. Aside from velocity dispersion, the MaNGA samples show weak to no correlation with other galaxy properties. Given the lack of statistically significant correlations with structural parameters in either dataset, we proceed with determining the redshift evolution of γ_T without applying corrections for these galaxy properties.

In Fig. 7, we present the MAGNUS sample in the stellar mass–size plane, color-coded by the locally weighted mean total density slope. We utilize the 2D LOESS algorithm (W. S. Cleveland & S. J. Devlin 1988), implemented via the LOESS package (M. Cappellari et al. 2013b) with a smoothing fraction of $\text{frac} = 0.5$, to recover the underlying average trend by suppressing intrinsic scatter. This projection facilitates the simultaneous inspection of correlations between γ_T and four key structural parameters: M_* , R_e , σ_e , and Σ_* . Consistent with the individual correlations, this plot reveals no significant dependence of γ_{tot} on any of these properties within the MAGNUS sample. This lack of correlation reinforces our primary finding that the observed redshift evolution is likely intrinsic rather than driven by structural selection effects, justifying our decision to not apply corrections for these galaxy properties.

4.4. Redshift Evolution of the Total Density Slope

The evolution of the total density slope at intermediate redshifts remains a subject of debate, with cosmological simulations and lensing studies often yielding contradictory predictions (R.-S. Remus et al. 2017; N. Sahu et al. 2024). To

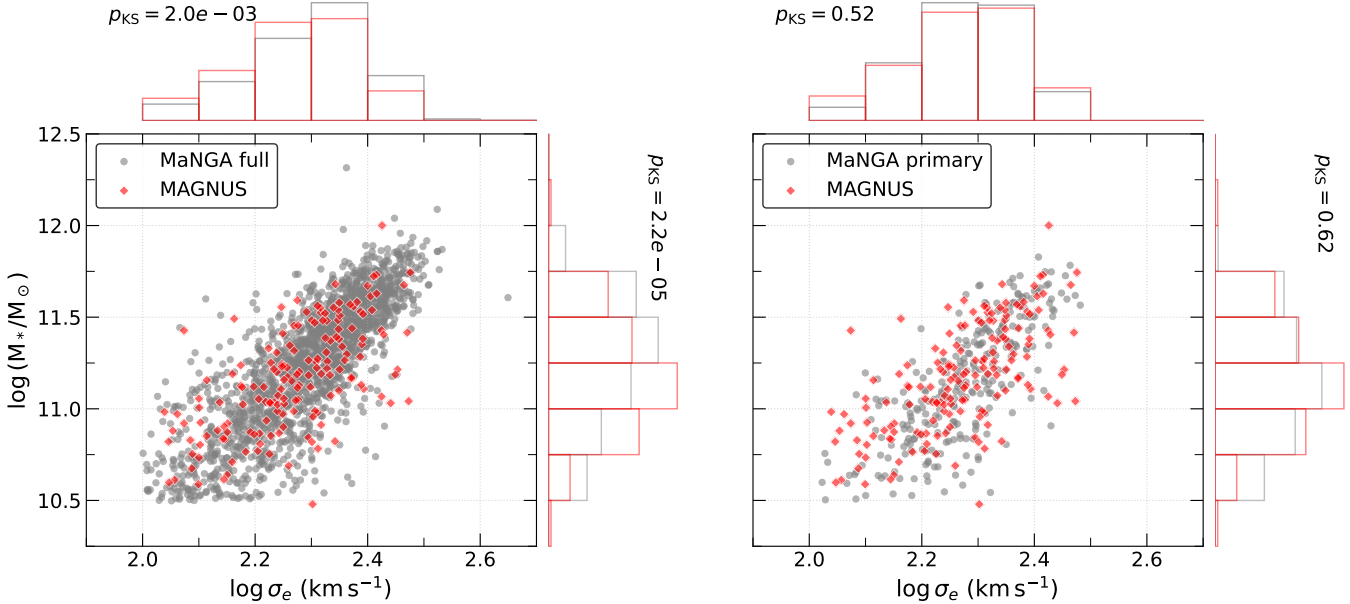


Figure 8. Distribution of the MAGNUS and MaNGA ETG sample in (σ_e, M_*) plane. The left panel displays the full MaNGA ETG parent sample (gray circles) compared with the MAGNUS sample (red diamonds). The right panel shows the MAGNUS sample against the statistically matched primary MaNGA subsample. Normalized histograms for each parameter, color-coded to match the corresponding sample markers, are attached to the axes illustrate the respective distributions. The p -values derived from two-sample Kolmogorov–Smirnov (K–S) tests are reported alongside the histograms, quantifying the statistical consistency of the distributions.

resolve this discrepancy, we quantified the evolutionary trend, $d\gamma_T/dz$, first within the MAGNUS sample alone and subsequently in combination with the local MaNGA ETG sample.

4.4.1. Evolution within the MAGNUS Sample

Empirical evidence indicates that massive ETGs rarely exhibit density slopes flatter than $\gamma_T = 1.5$ or steeper than $\gamma_T = 2.5$ (e.g. M. Cappellari 2026a, Fig. 11 left). We adopted this range as a prior for the power-law models, whereas for the composite models (stars+NFW and stars+gNFW), we applied this constraint posteriori. After excluding galaxies falling outside the range $1.5 \leq \gamma_T \leq 2.5$ and removing low-quality fits ($\text{Qual} \leq 0$), the final MAGNUS sample varies slightly by model choice where we retain 168 galaxies for the power-law models and 163 galaxies for the composite models. We found that the median total density slopes for the sample are $\gamma_T \approx 2.220 \pm 0.013$ for the power-law models and $\gamma_T \approx 2.187 \pm 0.013$ for the composite models, with uncertainties derived via bootstrap resampling. Although the statistical errors are small, these two medians are consistent within the estimated median systematic uncertainties ($\sigma_{\text{syst}} \sim 0.05$).

To characterize the redshift evolution, we performed a robust linear fit to the $\gamma_T - z$ relation using the LtsFit package. The relation is parameterized as $\gamma_T(z) = a + b_0(z - z_0)$, where z_0 is the median redshift of the sample, a is the normalization, and $b_0 \equiv d\gamma_T/dz$ represents the evolutionary gradient. We adopted the symmetrized 1σ measurement uncertainty for individual galaxies (mean of the upper and lower per-

centiles) and clipped outliers at the 3σ level. The resulting redshift gradients are summarized in Table 2. We found that the NFW and gNFW models yield comparable evolutionary trends, with a gradient of $d\gamma_T/dz \approx -0.21 \pm 0.07$ and an intrinsic scatter of ~ 0.14 . The power-law models suggest a somewhat shallower evolution, $d\gamma_T/dz \approx -0.10 \pm 0.07$, with similar intrinsic scatter. The redshift gradients from all six dynamical models are consistent within 1σ uncertainties and present a coherent qualitative picture: the total density slopes of massive ETGs are becoming steeper with decreasing redshift (significance ranging from 1.5σ to 3σ). This analysis represents the first dynamical study of such a large ETG sample over this redshift baseline to demonstrate that this observed trend is robust against the choice of mass model and velocity anisotropy. The steepening is mild, with the slope changing by only a few hundredths over several billion years. We visualize this evolution for the fiducial stars+gNFW with JAM_{sph} model in Figure 10.

4.4.2. Combined Analysis with the MaNGA Sample

Having quantified the evolutionary trend within the MAGNUS dataset, we now extend our analysis by incorporating the MaNGA ETG sample. Combining these datasets provides a long-baseline, enabling a significantly more precise constraint on the evolution of γ_T since $z < 1$.

Consistent with our treatment of the MAGNUS sample, we excluded MaNGA galaxies falling outside the physically motivated slope range ($1.5 \leq \gamma_T \leq 2.5$). This constraint

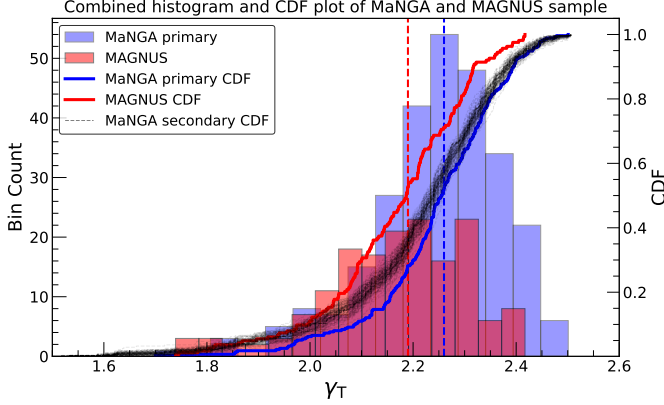


Figure 9. Distributions of the total density slope (γ_T) derived using the fiducial stars+gNFW with JAM_{sph} model. The γ_T distributions are presented as histograms for the intermediate-redshift MAGNUS sample (red) and the local primary MaNGA subsample (blue). Vertical dashed lines of the corresponding colors mark the median slope for each sample. The solid red and blue curves denote the Cumulative Distribution Functions (CDFs) for the MAGNUS sample and the primary MaNGA subsample, respectively. The set of black dashed curves displays the CDFs for the 100 importance-sampled secondary MaNGA sub-samples.

removed fewer than $\sim 2\%$ of the original 1,794 galaxies (the exact number varies slightly by mass model). To ensure a robust comparison, we employed a two-tiered strategy to select specific comparison sample from this filtered MaNGA catalog.

Primary Comparison Sample: First, we restricted the MaNGA dataset to include only those galaxies with high-quality dynamical fits ($\text{Qual} \geq 2$). This selection criterion naturally yields a subset of 277 ETGs (with a median redshift of $z \sim 0.044$) that closely matches the structural properties of the MAGNUS sample. Two-sample Kolmogorov–Smirnov (K–S) tests confirm that the stellar mass (M_*) and velocity dispersion (σ_e) distributions of this MaNGA subsample are statistically indistinguishable from those of the MAGNUS sample, yielding p -values of 0.62 and 0.52, respectively. Figure 8 illustrates this structural agreement. We adopt this high-quality, statistically matched subset as our primary comparison sample.

Secondary Comparison Sample: To verify that our results are not driven solely by the restriction to high-quality fits, we constructed a secondary comparison set drawn from the full MaNGA ETG parent sample ($\text{Qual} \geq 1$). Since the full sample distribution differs from MAGNUS significantly (see Fig. 8), we utilized an importance sampling technique (detailed in Appendix B) to generate 100 independent realizations, each consisting of 275 ETGs drawn without replacement. Each realization was constructed to be statistically matched to the MAGNUS sample in M_* and σ_e (verified via K–S tests with p -value < 0.01).

In the following analysis, we treat the results derived from the primary sample as our main findings. The analysis of the secondary samples serves as a robustness check, for which, we report the ensemble average of the results derived from the 100 independent realizations.

The total density slopes for the MaNGA sample were adopted from DynPop I. Since DynPop I did not employ a single power-law mass model, we restrict this comparative analysis to the four composite models (stars+NFW and stars+gNFW with cylindrical and spherical alignments). Although DynPop I does not provide individual measurement uncertainties for γ_T , it estimates systematic errors based on the RMS scatter between γ_T values from these four model assumptions (see Table 3 from DynPop I). We adopt these quality-dependent error values as our uncertainties and assign errors of $\sigma_{\gamma_T} \approx 0.035, 0.024$, and 0.056 to galaxies with quality flags (Qual) of 3, 2, and 1, respectively.

For the primary MaNGA subsample, we measured median slopes of $\gamma_T \approx 2.260 \pm 0.013$ across all four composite models (ranging from 2.25 to 2.27). Similarly, the ensemble average of the median slopes for the 100 secondary subsamples is $\gamma_T = 2.240 \pm 0.009$ (for the fiducial stars+gNFW with JAM_{sph} model). Comparing these local baselines to the MAGNUS medians derived in subsubsection 4.4.1 ($\gamma_T \approx 2.19$), we observe a systematic offset, with the local galaxies exhibiting steeper density profiles.

This evolutionary shift is small but statistically significant. We compared the cumulative distribution functions (CDFs) of the MAGNUS and MaNGA datasets using both the two-sample Kolmogorov–Smirnov (K–S) test and the Anderson–Darling (A–D) test, the latter being particularly sensitive to deviations in the distributional tails. For all four dynamical models and both MaNGA comparison sets (primary and secondary), the tests strongly reject the null hypothesis that the samples are drawn from the same underlying distribution ($p \leq 0.01$). Figure 9 displays the combined histograms and CDFs for the stars+gNFW with JAM_{sph} model, illustrating the clear distributional shift toward steeper slopes in the local Universe.

To quantify the cosmic evolution of the total density slope, we performed robust linear fits to the γ_T – z relation for the combined datasets. For the primary analysis (MAGNUS + Primary MaNGA), we fitted all four composite dynamical models. For the secondary analysis, we performed 100 independent fits, each combining MAGNUS with one of the importance-sampled MaNGA realizations, focusing on the fiducial stars+gNFW with JAM_{sph} model. We utilized the LtsFit package to determine the best-fit parameters, employing the same linear parameterization defined in subsubsection 4.4.1 and applying a 3σ outlier clipping threshold. The results from the combined primary dataset are consistent

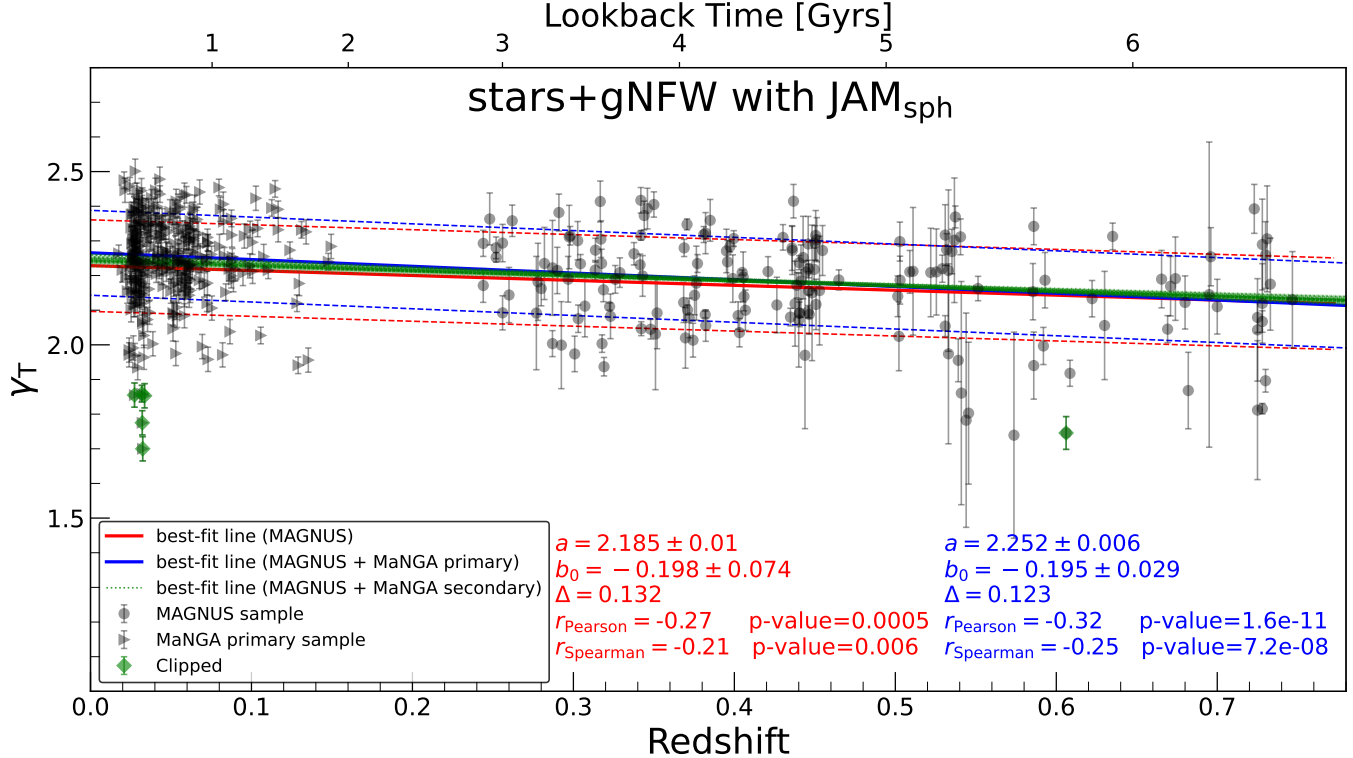


Figure 10. Evolution of the total mass density slope (γ_T) as a function of redshift. The γ_T for both sample are measured using the fiducial stars+gNFW with JAM_{sph} dynamical model. The linear trends were determined using the LtsFit package according to the parameterization $\gamma_T = a + b_0(z - z_0)$, where z_0 represents the median redshift of the sample, a is the intercept, and b_0 quantifies the redshift gradient ($d\gamma_T/dz$). The red solid line delineates the best-fit relation for the MAGNUS sample alone, while the blue solid line represents the fit to the combined dataset (MAGNUS + primary MaNGA subsample). The surrounding dashed lines of similar color mark the 1σ intrinsic scatter for the respective relations. The ensemble of green lines displays the fits derived from combining MAGNUS with each of the 100 importance-sampled secondary MaNGA sub-samples. The derived best-fit coefficients, intrinsic scatter (Δ), and correlation statistics (Pearson and Spearman coefficients with associated p -values) are reported within the panel, color-coded in red and blue to correspond with the MAGNUS-only and combined MAGNUS+MaNGA primary sample, respectively.

across all NFW and gNFW model variants, yielding a global redshift gradient of $d\gamma_T/dz \approx -0.20 \pm 0.03$ with an intrinsic scatter of $\sigma_{\text{int}} \approx 0.12$. This result implies a statistically significant ($\sim 6\sigma$) steepening of the density profile over cosmic time. The steepening is mild in amplitude and it is only detected thanks to our large sample of high quality data.

The secondary analysis reinforces this finding. Across the 100 importance-sampled realizations, we recovered a mean gradient of $\langle d\gamma_T/dz \rangle = -0.150$ with a standard deviation of 0.017. While slightly shallower than the primary result, it robustly confirms the trend of the evolution. Figure 10 illustrates these findings, where the solid red line denotes the fit to the primary combined sample, while the faint green lines show fits for the secondary realizations. The fit parameters for the combined MAGNUS + MaNGA primary sample are detailed in Table 2. In summary, the inclusion of the local baseline significantly reduces the statistical uncertainty on the evolutionary gradient compared to the MAGNUS-only measurement. Both the primary and secondary combined

analyses provide compelling evidence that the total density slopes of massive ETGs have mildly steepened over the last 6-7 billion years ($z < 1$).

Finally, we tested whether the observed redshift evolution is a global trend or if it is driven by specific kinematic regimes. To verify this, we binned both the MAGNUS and MaNGA datasets by velocity dispersion (σ_e) using a fixed bin width of 40 km s^{-1} . For each bin, we computed the median γ_T and associated bootstrap uncertainties using the fiducial stars+gNFW with JAM_{sph} model. Figure 11 presents these binned trends as a function of $\log \sigma_e$. Comparing the MAGNUS sample with the primary MaNGA subsample, we observe that the high-redshift galaxies display systematically lower median γ_T values across nearly the entire dynamic range of velocity dispersion. On average, the MAGNUS bins are offset by approximately 3% compared to their local counterparts, a difference consistent with the global ensemble offset mentioned above. This confirms that the steepening of the

density slope is a pervasive feature of the population and persists after controlling for σ_e .

We repeated this test using the secondary MaNGA subsamples. In this case, we observe a partial overlap between the high- and low-redshift populations in the lowest velocity dispersion bin, however, a clear separation emerges for $\log(\sigma_e/\text{km s}^{-1}) > 2.15$. Notably, the MAGNUS sample exhibits a flattening of the $\gamma_T - \sigma_e$ relation above a threshold of $\log \sigma_e \approx 2.2$ ($\sigma_e \approx 150 \text{ km s}^{-1}$), where the median slope remains roughly constant. While this feature is less distinct in the primary MaNGA subsample, it is reproduced at the ensemble level in the secondary MaNGA realizations. This behavior mirrors findings in local ETG studies, which have identified a break in the structural scaling relations at $\sigma_e \approx 100 - 150 \text{ km s}^{-1}$ (e.g., A. Poci et al. 2017; R. Li et al. 2019; K. Zhu et al. 2024; S. Li et al. 2024). Importantly, varying the bin width or the specific binning scheme does not alter our qualitative conclusion that at fixed σ_e , massive ETGs at $z \sim 0.5$ have shallower density profiles than those at $z \sim 0$.

Collectively, these results provide a robust evidence that massive ETGs have experienced a gradual though mild evolution since $z \sim 1$, characterized by a steepening of their total density slopes with decreasing redshift. A critical strength of this analysis is the homogeneity of the methodology, the galaxy properties for both the MAGNUS and MaNGA samples were derived using identical kinematic extraction techniques, surface brightness parameterizations, and dynamical modeling assumptions. Consequently, potential systematics associated with the JAM formalism or tracer definitions are minimized, or expected to impact both epochs equally. This differential robustness strongly supports the interpretation that the observed shift in γ_T is a genuine physical signature of galaxy assembly over the last 6-7 billion years.

5. DISCUSSION

5.1. Robustness against Velocity Dispersion Selection

As discussed in [subsubsection 4.4.2](#), the total density slope flattens above a characteristic velocity dispersion threshold. While our sample selection process adopted $\sigma_e \geq 100 \text{ km s}^{-1}$, recent work by K. Zhu et al. (2024) and S. Li et al. (2024) suggests this structural break may occur at $\sigma_e \approx 150 \text{ km s}^{-1}$. To ensure our evolutionary trends are not driven by galaxies below this threshold, we repeated our analysis using this stricter selection criterion.

Before performing the analysis, we can anticipate the outcome based on the binned trends shown in [Figure 11](#). For the MAGNUS sample, the median γ_T remains effectively constant at $\log(\sigma_e/\text{km s}^{-1}) > 2.2$ ($\sigma_e > 150 \text{ km s}^{-1}$). In contrast, the median slope for the primary MaNGA subsample increases slightly in this regime, while the secondary MaNGA subsamples remain flat at the ensemble level. Cru-

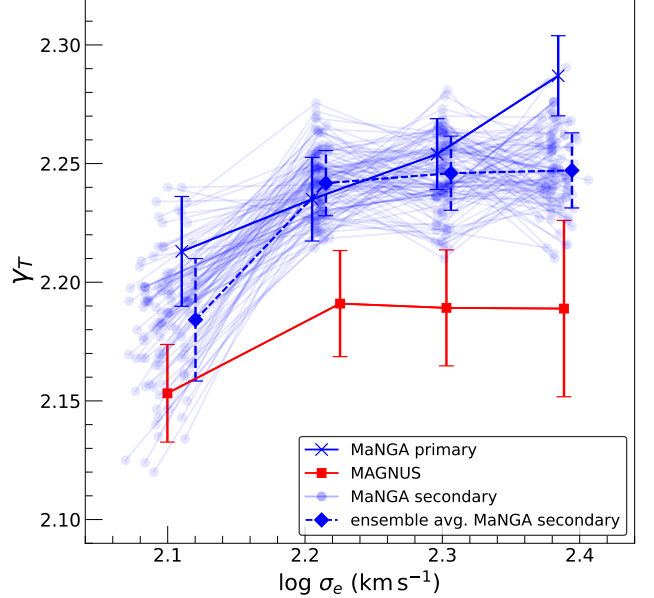


Figure 11. Comparison of the total mass density slope (γ_T) as a function of central velocity dispersion (σ_e). The galaxies were grouped into fixed velocity dispersion bins of width 40 km s^{-1} , with γ_T values derived from the fiducial stars+gNFW with JAM_{sph} model. The red squares (connected by a solid red line) and blue crosses (connected by a solid blue line) display the median values for the MAGNUS sample and the primary MaNGA subsample, respectively. To illustrate the variation within the local baseline, the light blue circles represent the binned medians for the individual importance-sampled secondary MaNGA sub-samples. The blue diamonds connected by a blue dashed line trace the ensemble average of these secondary sets. Error bars indicating bootstrap uncertainties are plotted for the MAGNUS, primary MaNGA, and secondary ensemble average.

cially, even above this higher threshold, the distributions of the high- and low-redshift samples remain distinct. Consequently, we expect that the CDFs will retain their separation and the qualitative trend of redshift evolution will persist.

Applying the stricter cut of $\sigma_e \geq 150 \text{ km s}^{-1}$ reduces the MAGNUS and full MaNGA ETG samples to 130 and 1,537 galaxies (decreases of 20% and 14%, respectively). The primary MaNGA subsample decreases by 14% to 235 ETGs. Despite these reductions, the median γ_T values remain robust. For the stars+gNFW with JAM_{sph} model, the MAGNUS median is 2.188 ± 0.015 , identical to the baseline result. Similarly, the primary MaNGA median (2.260 ± 0.015) and the secondary ensemble mean (2.241 ± 0.009) are unchanged. K-S and A-D tests also confirm that the populations remain statistically distinguishable ($p \ll 0.01$).

Consistent with our anticipation, the inferred redshift evolution not only persists but strengthens in this high-mass region. For the MAGNUS-only sample, the gradient for the composite models steepens to $d\gamma_T/dz \approx -0.27 \pm 0.08$. A similar steepen-

Table 2. List of best-fit parameters characterizing the redshift evolution of the total density slope (γ_T) for various dynamical models. The evolutionary trends were quantified using the linear relation $\gamma_T = a + b_0(z - z_0)$, where z_0 represents the median redshift of the sample and b_0 denotes the redshift gradient ($d\gamma_T/dz$). We report the best-fit coefficients, and the intrinsic scatter (Δ) derived from the fit. Results are presented for both the MAGNUS sample alone and the combined MAGNUS + MaNGA primary dataset.

Models	MAGNUS only			MAGNUS and MaNGA primary		
	a	$b_0 = \frac{d\gamma_T}{dz}$	Δ	a	$b_0 = \frac{d\gamma_T}{dz}$	Δ
JAM _{cyl} : power-law	2.237 ± 0.008	-0.076 ± 0.062	0.122			
JAM _{sph} : power-law	2.232 ± 0.009	-0.115 ± 0.069	0.124			
JAM _{cyl} : Stars + NFW	2.182 ± 0.010	-0.235 ± 0.076	0.138	2.262 ± 0.006	-0.216 ± 0.029	0.121
JAM _{sph} : Stars + NFW	2.182 ± 0.010	-0.192 ± 0.074	0.136	2.249 ± 0.007	-0.192 ± 0.030	0.125
JAM _{cyl} : Stars + gNFW	2.185 ± 0.010	-0.209 ± 0.075	0.132	2.264 ± 0.006	-0.213 ± 0.028	0.117
JAM _{sph} : Stars + gNFW	2.185 ± 0.010	-0.198 ± 0.074	0.134	2.252 ± 0.006	-0.195 ± 0.029	0.123

ing is observed in the combined analysis, where the gradient for the MAGNUS + primary MaNGA sub-sample increases to $d\gamma_T/dz \approx -0.225 \pm 0.030$, and the mean gradient from the secondary MaNGA realizations shifts to $\langle d\gamma_T/dz \rangle = -0.160$ (standard deviation 0.015). Across all cases, the magnitude of the evolutionary gradient increases by approximately 10% compared to the baseline analysis, while maintaining similar statistical precision. These results confirm that the observed steepening of the total density slope is not a selection artifact of lower-dispersion galaxies.

5.2. Comparison with previous dynamical studies

In this section, we place our results in the context of previous dynamical studies of redshift evolution of the total slope at $z < 1$. C. Derkenne et al. (2021) analyzed 90 ETGs in the Frontier Fields ($z \sim 0.35$) using archival MUSE data. Although the MAGNUS sample incorporates data from six of the seven fields utilized in that study, only ~ 20 galaxies overlap due to differences in selection criteria. While the Frontier Fields sample shares a similar velocity dispersion distribution (median $\sigma_e \approx 175 \text{ km s}^{-1}$) with MAGNUS, it is statistically distinct in terms of total dynamical mass (median $\log_{10} M_{\text{dyn}}/M_{\odot} = 10.82$). Using a stars+gNFW with JAM_{cyl} model and defining the total density slope as the mean logarithmic gradient ($\Delta \log \rho/\Delta \log r$) over $\sim 3R_e$, they reported a median slope of $\gamma_T = 2.11 \pm 0.03$ (standard deviation 0.23). Comparing this result to the full ATLAS^{3D} sample ($\gamma_T \approx 2.14$), they concluded that there was no significant evolution over the last 4 – 6 Gyr.

Subsequently, C. Derkenne et al. (2023) modeled 28 galaxies (including 20 ETGs) from the MAGPI survey ($z \sim 0.3$), which match the mass and σ_e range of the MAGNUS sample. Employing a stars+gNFW with JAM_{cyl} model, they measured the total density slope as the mean logarithmic slope over the radial range $[0.1R_e, 2R_e]$. To evaluate the γ – z evolution, they

homogenized the comparison by re-measuring the slopes of the Frontier Fields and ATLAS^{3D} samples (using results from C. Derkenne et al. 2021 and A. Poci et al. 2017, respectively) within the same radial aperture, while excluding galaxies with $\sigma_e < 100 \text{ km s}^{-1}$. They found that the median slope of the MAGPI sample is $\gamma_T = 2.22 \pm 0.05$, consistent with the homogenized measurement of the ATLAS^{3D} sample (median $\gamma_T \approx 2.25$), and suggested that the total density slope has remained constant over the past 3 – 4 Gyr. However, they noted that the derived slope is sensitive to the radial aperture: when measured within $1R_e$, the median MAGPI slope becomes 2.19. This is identical to our measurement for the MAGNUS sample ($\gamma_T = 2.19 \pm 0.01$). Notably, they found that the re-measured Frontier Fields sample exhibits a significantly shallower median slope of $\gamma_T = 2.01 \pm 0.04$. They attributed the discrepancy between the steeper MAGPI/ATLAS^{3D} slopes and the shallower Frontier Fields slopes to environmental effects, as the Frontier Fields galaxies reside in dense cluster cores while MAGPI targets diverse environments. While investigating environmental dependencies is beyond the scope of this work, evaluating this aspect using the combined MAGNUS and MaNGA datasets remains a compelling avenue for future research.

In the local Universe ($z \sim 0$), A. Poci et al. (2017) analyzed 260 ETGs from the ATLAS^{3D} survey using three different mass models, including the stars+gNFW with JAM_{cyl} parameterization ('Model I'). The ATLAS^{3D} sample typically has lower mass (median $\log_{10} M_{\text{dyn}}/M_{\odot} = 10.58$) and velocity dispersion (median 130 km s^{-1}) than MAGNUS. For the gNFW+JAM_{cyl} model, they found a median slope within $1R_e$ of 2.19 ± 0.02 (intrinsic scatter 0.17) for the 142 ETGs with $\sigma_e > 125 \text{ km s}^{-1}$. If we further restrict this sample to ETGs with reliable quality flags ($\text{Qual} \geq 1$) and slopes within the physical range $1.5 \leq \gamma_T \leq 2.5$, the subsample (115 ETGs) yields a median $\gamma_T = 2.20 \pm 0.01$. While this value is flatter

than our primary MaNGA baseline (2.26 ± 0.01), it is steeper than the full ATLAS^{3D} population (2.14), consistent with the known positive correlation between γ_T and σ_e . [R. Li et al. \(2019\)](#) analyzed an earlier release of MaNGA (~ 2000 galaxies) using JAM, finding a mean slope of $\gamma_T = 2.24 \pm 0.22$ for galaxies with $\sigma_e > 100 \text{ km s}^{-1}$. This is fully consistent with the results from our primary and secondary MaNGA subsamples. Similar results, all consistent with a local $\gamma_T \approx 2.2$ above the break in σ_e have been reported in other local dynamical studies (e.g., [M. Cappellari et al. 2015](#); [A. Yildirim et al. 2017](#); [S. Bellstedt et al. 2018](#)), as reviewed in our [section 1](#). Collectively, these comparisons indicate that while differences in sample selection and slope definitions exist, our findings fit consistently within the broader landscape of dynamical results, bridging the gap between specific intermediate-redshift surveys and large local catalogs.

5.3. Comparison with Gravitational Lensing Studies

Studies utilizing strong gravitational lensing provide an independent probe of the total density slope over cosmic time. Generally, these investigations use a joint “Lensing and Dynamics” (L&D) analyses and report a non-negligible redshift gradient ($d\gamma_T/dz < 0$), indicating that ETGs become structurally steeper at lower redshifts. This method combines the robust projected mass constraint from lensing with the stellar velocity dispersion by solving the Jeans equations (typically assuming a spherical symmetry). In this way, the L&D method effectively constrains the global mass-weighted density slope within the effective radius ([L. V. E. Koopmans et al. 2006](#); [A. A. Dutton & T. Treu 2014](#)) which is physically comparable to the dynamical slopes derived in our work.

Early L&D analyses consistently pointed toward a steepening mass profile. [L. V. E. Koopmans et al. \(2006\)](#) analyzed 15 lens galaxies from the SLACS survey ($0.06 < z < 0.33$) combined with 5 higher-redshift systems ([T. Treu & L. V. E. Koopmans 2004](#)), measuring an evolutionary gradient of $d\gamma_T/dz \approx -0.23 \pm 0.16$ and an average slope of $\gamma_T \approx 2.01$. Expanding the sample to 73 SLACS lenses, [M. W. Auger et al. \(2010\)](#) reported a slightly steeper average slope of 2.08 ± 0.03 . Subsequent studies incorporating higher-redshift samples reinforced this evolutionary trend. By combining SLACS with the SL2S and LSD surveys (extending to $z \sim 1$), [A. J. Ruff et al. \(2011\)](#) measured a gradient of $d\gamma_T/dz \approx -0.25 \pm 0.11$. Similarly, [A. S. Bolton et al. \(2012\)](#), adding the intermediate-redshift BELLS sample, reported a significantly stronger evolution of $d\gamma_T/dz \approx -0.60 \pm 0.15$ over the interval $0.1 < z < 0.6$.

Consistent results were also reported by [R. Li et al. \(2018\)](#) using a combined sample of SL2S, BELLS, and GALLERY lenses. More refined analyses distinguishing between population-level evolution and individual galaxy evolution have also been conducted. [A. Sonnenfeld et al. \(2013\)](#)

measured a population gradient of $d\gamma_T/dz = -0.31 \pm 0.10$ for the combined SLACS and SL2S sample. After accounting for the size-mass growth of ETGs, they inferred an intrinsic evolutionary rate for individual galaxies of $d\gamma_T/dz = -0.10 \pm 0.12$.

While recent studies comparing methodology suggest discrepancies when using lensing-only constraints ([A. Etherington et al. 2023](#); [N. Sahu et al. 2024](#)), the L&D results from the same works remain broadly consistent with the dynamical picture. Lensing-only approaches fit a mass profile directly to the distorted image configuration; while precise, they are sensitive to the local density slope at the Einstein radius and can be affected by the mass-sheet degeneracy (MSD) if the profile deviates from a simple power law (e.g., [C. Y. Tan et al. 2024](#)).

Overall, the evolutionary trends derived from lensing ETG samples are remarkably consistent with the results presented in this work. Our measured gradients for the combined MAGNUS+MaNGA dataset ($d\gamma_T/dz \approx -0.19$ to -0.22) fall squarely within the range reported by L&D studies (-0.10 to -0.31). This agreement is particularly significant given that lens ETG galaxies mostly overlap with respect to stellar mass and velocity dispersion with our sample. The convergence of these two independent methods—pure dynamics and joint lensing+dynamics—provides compelling evidence that the steepening of the total density slope is a fundamental feature of massive galaxy evolution since $z \sim 1$. To rigorously quantify any residual systematic discrepancies, a combined SLACS and SL2S sample augmented with spatially resolved kinematics offers an ideal testbed. By applying an identical mass and anisotropy parameterizations to model the resolved velocity fields of these lens galaxies, we could decisively test the consistency between lensing, dynamical, and joint L&D analyses.

5.4. Comparison with Cosmological Simulations

Comparing our observational constraints with predictions from cosmological hydrodynamical simulations reveals significant tensions regarding the evolution of the total density slope at $z < 1$. However, it is important to note that the comparison is limited by differences in sample selection, as the simulated catalogs may not fully reproduce the specific combination of stellar mass and velocity dispersion characterizing our sample. The **Magneticum** Pathfinder simulations ([R.-S. Remus et al. 2017](#)) predict a monotonic shallowing of the density profile, with γ_T decreasing from ~ 2.3 at $z = 1$ to an isothermal value (~ 2.0) at $z = 0$. Similarly, the **IllustrisTNG** suite ([Y. Wang et al. 2019](#)) predicts a multi-phase evolutionary history where the density slope stabilizes below $z < 1$, maintaining a nearly constant isothermal profile ($\gamma_T \approx 2.0$) during this epoch. Both of these predictions con-

flicts with the statistically significant gradient measured in our combined MAGNUS+MaNGA sample.

Qualitatively, the **Horizon-AGN** simulations (S. Peirani et al. 2019) offer a closer match to our findings, predicting a continuous steepening of the total density slope from $z = 2$ to $z = 0$. However, a quantitative discrepancy remains. While Horizon-AGN predicts slopes converging to $\gamma_T \approx 2.0$ at the present day, our dynamical measurements indicate that massive ETGs are super-isothermal ($\gamma_T \approx 2.26$) at $z \sim 0$.

The diversity in simulated trends—ranging from shallowing to steepening—highlights the sensitivity of the total density slope to sub-grid physics implementation, particularly AGN feedback and its coupling to the dark matter halo (S. Peirani et al. 2019; Y. Wang et al. 2020; S. Mukherjee et al. 2021). The fact that most current simulations converge toward $\gamma_T \approx 2.0$, whereas observational studies (both ours and previous lensing-based results) consistently find $\gamma_T \geq 2.1$, suggests that current models may overestimate the efficiency of feedback in expanding the central mass distribution or underestimate the baryon concentration in the cores of massive ellipticals.

5.5. Physical Implications for Galaxy Assembly

The prevailing “two-phase” formation scenario posits that massive ETGs assemble the bulk of their central mass at high redshift ($z > 2$) via dissipative processes, followed by a protracted phase of accretion dominated by dissipationless (dry) mergers (L. Oser et al. 2010; P. G. van Dokkum et al. 2015; T. Naab & J. P. Ostriker 2017). Dry mergers deposit material in the galaxy outskirts, driving significant size growth and causing the total density profile to become shallower over time (M. Hilz et al. 2013; P. G. van Dokkum et al. 2010).

Our finding that the total density slope has *steepened* (or at least remained super-isothermal) since $z \sim 1$ stands in tension with a purely dissipationless merger history. The observed steepening ($d\gamma_T/dz < 0$) therefore implies that dissipative processes must play a non-negligible role even in the late-stage assembly of massive ETGs. This interpretation is consistent with theoretical constraints suggesting that dry mergers alone cannot fully account for the structural scaling relations of present-day ETGs (C. Nipoti et al. 2009b,a). Mechanisms such as the accretion of gas-rich satellites or adiabatic contraction can channel baryons to the galaxy center. The dominant old stellar populations of these galaxies (S. Lu et al. 2023; P. Mozumdar et al. 2025a) rule out major starbursts at $z < 1$, but a “drizzle” of gas-rich minor mergers could provide sufficient dissipation to counteract the shallowing effect of dry accretion without significantly altering the global stellar ages. Furthermore, cosmological simulations often produce shallower, near-isothermal profiles due to strong AGN feedback expanding the central mass distribution (S. Peirani et al. 2019; Y. Wang et al. 2020; S. Mukherjee et al.

2021). Our results suggest that feedback coupling in the most massive ETGs might be weaker or less efficient at rearranging the central potential than currently predicted by these models.

Alternatively, the mild increase in γ_T may be intrinsic to the dry merger scenario itself, driven by the non-homologous growth of massive galaxies. Observations indicate that the size evolution of ETGs outpaces their mass accumulation below $z \sim 2$, following a scaling relation of $\Delta \log R_e \sim 2\Delta \log M_*$ (P. G. van Dokkum et al. 2010; S. G. Patel et al. 2013; P. G. van Dokkum et al. 2015). It is plausible that while mass is being accreted onto the outskirts, it is insufficient to “keep up” with the rapid expansion of the physical scale of the effective radius. Consequently, as the measurement aperture (R_e) encompasses these diffuse outer regions, the mass-weighted average slope may appear to steepen (or fail to shallow as predicted by homologous growth models), reflecting the preservation of the dense core relative to the growing envelope.

To summarize, the observed evolution, while statistically significant, is mild in magnitude. This implies that the fundamental mass structure of massive ETGs was already largely established by $z \sim 1$, with the near-isothermal density profile being in place well before this epoch. Our findings suggest a scenario where dry mergers dominate the size growth, but dissipative processes—or inefficient feedback mechanisms—cannot be neglected, as they appear necessary to maintain the steep total density slopes observed over the last 7 billion years.

6. SUMMARY AND CONCLUSION

In this work, the third installment of the MAGNUS series, we investigated the total density slope evolution of massive ETGs over the last 6 billion years ($z < 1$). We performed a detailed dynamical analysis of the full MAGNUS sample (212 ETGs; $0.25 < z < 0.75$), constraining their mass distributions by applying the Jeans Anisotropic Modeling (JAM) technique to spatially resolved stellar kinematics derived from high-S/N MUSE-DEEP data cubes. This analysis relied on Multi-Gaussian Expansion (MGE) models of the surface brightness constructed from high-resolution HST imaging. After applying quality control and physically motivated constraints, we obtained a final sample of ~ 165 galaxies. To constrain the evolution of γ_T across cosmic time, we combined this intermediate-redshift dataset with a local Universe sample ($z \sim 0.05$) of 1794 ETGs from the MaNGA survey. We adopted the dynamical properties for these local ETGs from the DynPop catalogue of K. Zhu et al. (2023), specifically because that study utilized an identical JAM and MGE framework, thereby ensuring a strictly homogeneous comparison between the two samples.

To ensure the robustness of our results against model assumptions, we explored six distinct dynamical parameteri-

zations for the MAGNUS sample, varying the mass profile (power-Law, stars+NFW, stars+gNFW) and the alignment of the velocity ellipsoid (cylindrical vs. spherical). However, for the comparative analysis with MaNGA, we focused on the four composite models common to both datasets. Furthermore, to account for selection effects in the local baseline, we employed a two-tiered comparison strategy. We selected a primary MaNGA sample (277 ETGs) of high-quality fits ($\text{Qual} \geq 2$) that naturally matches the MAGNUS sample, and a secondary set of 100 importance-sampled realizations drawn from the full ETG sample. Our main conclusions are summarized as follows:

- We find that the total density slopes, γ_T of intermediate-redshift ETGs are systematically shallower than their local counterparts. The median slope for the MAGNUS sample is $\gamma_T \approx 2.190 \pm 0.013$, whereas for the local MaNGA baseline it is $\gamma_T \approx 2.260 \pm 0.013$. The γ_T distributions of the two epochs are also statistically distinct.
- Combining the MAGNUS sample with the primary MaNGA baseline, we measure a redshift gradient of $d\gamma_T/dz \approx -0.20 \pm 0.03$ (-0.19 to -0.22 depending on the model). Similarly, MAGNUS with 100 secondary importance-sampled realizations also yield a mean gradient of $\langle d\gamma_T/dz \rangle = -0.150 \pm 0.017$ for the stars+gNFW with JAM_{sph} model. Together, these results provide a $\sim 6\sigma$ evidence that the total density profiles of massive ETGs have steepened at level of $\sim 5\%$ over the last 6-7 billion years.
- Within the MAGNUS sample, the total density slope exhibits negligible correlations with stellar mass, effective radius, and surface mass density. This suggests that the observed redshift evolution is not driven by simple scaling relations with these parameters.
- We observed that the correlation between γ_T and velocity dispersion flattens above $\sigma_e \approx 150 \text{ km s}^{-1}$. Crucially, restricting our analysis to this high-dispersion regime ($\sigma_e > 150 \text{ km s}^{-1}$) yields evolutionary trends that are qualitatively identical to—and even slightly stronger than—those derived from the baseline $\sigma_e >$

A. ROBUSTNESS OF TOTAL DENSITY SLOPE TO ANISOTROPY PRIORS

In our dynamical modeling, the orbital anisotropy is parameterized by the ratio of the velocity dispersion components, σ_z/σ_R for the JAM_{cyl} case and σ_θ/σ_r for the JAM_{sph} case. In our primary analysis, we imposed a Gaussian prior on these

100 km s^{-1} selection. This confirms that the observed steepening of γ_T is not artifact of including lower-dispersion systems.

- The derived evolutionary trends are statistically consistent across power-law and composite models, regardless of the velocity ellipsoid alignment (cylindrical vs. spherical).

Galaxy evolution is a complex, multi-faceted process. As a result, a study regarding total density slope evolution is inevitably subject to challenges, such as sample selection, limited sample sizes, methodological systematics, progenitor bias, and the diversity of host environments etc.. Addressing all these factors simultaneously remains difficult. However, within the limitations of this study, this work provides the most precise estimate of γ_T evolution in massive ETGs since $z \sim 1$, to date.

Combining these results with the previous studies in the MAGNUS series offers a comprehensive view of the assembly history of massive ETGs since $z \sim 1$. In **MAGNUS I** (P. Mozumdar et al. 2025a), we established that the global scaling relations, morphologies, and stellar population properties were largely in place by $z \sim 1$. In **MAGNUS II** (P. Mozumdar et al. 2025b), we identified a kinematic evolution, characterized by a decrease in rotational support over cosmic time, consistent with a merger-driven history. In this work (**MAGNUS III**), we observed that this merger history may have also induced a subtle but significant steepening of the total mass profile. Together, these findings depict massive ETGs not as complete static relics, but as dynamically evolving systems well into the latter half of the Universe’s history.

ACKNOWLEDGMENTS

Software: MgeFit (M. Cappellari 2002), JamPy (M. Cappellari 2008, 2020, 2026b), pPXF (M. Cappellari 2017, 2023), loess (M. Cappellari et al. 2013b), emcee (D. Foreman-Mackey et al. 2013), NumPy (C. R. Harris et al. 2020), SciPy (P. Virtanen et al. 2020), Astropy (Astropy Collaboration 2013, 2018)

APPENDIX

ratios, centered at isotropy, $\mathcal{N}(1.0, 0.07)$. For the JAM_{cyl} configuration, we additionally enforced an upper bound of unity ($\sigma_z/\sigma_R \leq 1$), effectively adopting a half-Gaussian prior.

The motivations behind this choice of informed prior over an uniform or flat prior is described in Sect. 3.3.1. In contrast, the MaNGA sample analyzed in DynPop I where modeled

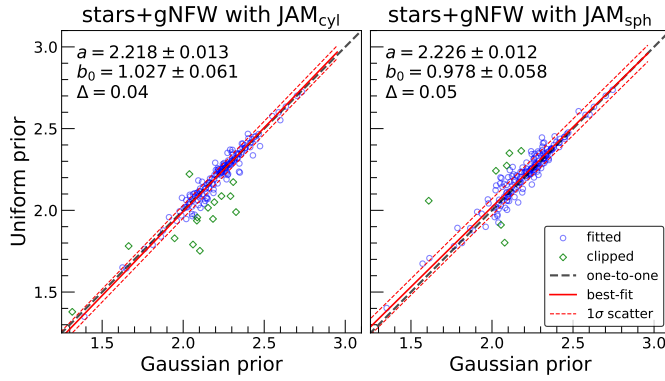


Figure 12. Effect of adopted anisotropy prior on measured γ_T from stars+gNFW model with JAM_{cyl} (left) and JAM_{sph} (right) orientation. For both case, the γ_T values are excluded at 3σ level and denoted by green diamond shape markers while the fitted values are marked as blue circle. Also for both case, the one-to-one lines (black dashed line) coincide with the best-fit lines (red solid line). Coefficients of the best-fit line and rms scatter are also shown for both model.

with an uniform prior on σ_z/σ_R and σ_θ/σ_r such that $\mathcal{R}(q) < \sigma_z/\sigma_R < 1$ and $\mathcal{R}(q) < \sigma_\theta/\sigma_r < 2$, where the lower bound is defined by the intrinsic axial ratio q as $\mathcal{R}(q) = \sqrt{0.3 + 0.7q}$.

To check the effect of these anisotropy priors on the measured γ_T and evaluate whether the observed evolutionary trends in γ_T are influenced by this difference in priors, we re-modeled the MAGNUS galaxies with ‘Qual’ ≥ 1 , using the same uniform prior adopted in the DynPop I. Everything else such as the priors on other model parameters and fitting procedure described in Sect. 3.4 etc., remain same.

Fig. 12 presents the comparison of γ_T with the Gaussian prior vs the flat prior for both stars+gNFW with JAM_{cyl} and JAM_{sph} models. The γ_T for each galaxy are measured from the best-fit models. We quantified the relationship between the two sets of measurements using the LtsFit package, performing a robust linear regression with outliers clipped at the 3σ level. We found that while the choice of prior influences the specific best-fit anisotropy and mass parameters, it has a negligible impact on the derived total density slope. For both case, the slope of the best-fit line is close to unity, and almost overlap with the one-to-one line with an small intrinsic scatter. For the NFW models, we also found similar results. However, for the power-law models, we observed more deviation of the best-fit line from the one-to-one relationship and the intrinsic scatter is slightly higher than the composite models. These results confirm that our γ_T measurements are robust to the specific choice of anisotropy prior and does not affect the measured evolutionary trend of γ_T .

B. IMPORTANCE SAMPLING METHOD

To ensure a robust comparison between our target sample (MAGNUS) and the underlying parent population (MaNGA),

we construct a control sample matched in stellar mass and velocity dispersion. We employ a 2D Sampling Importance Resampling (SIR) technique to select a subset of galaxies from the parent sample that reproduces the joint distribution of the target sample. We first discretize the 2D parameter space defined by the above two properties into a grid of 10×10 bins. For each galaxy k in the parent sample falling into the bin (i,j) , we assign a selection weight w_k proportional to the ratio of the number densities of the two samples in that bin:

$$w_k = \frac{N_{\text{target}}^{ij}}{N_{\text{parent}}^{ij}} \quad (\text{B1})$$

where N_{target}^{ij} and N_{parent}^{ij} represent the number of galaxies in the (i,j) -th bin for the target and parent samples, respectively. In bins where $N_{\text{parent}}^{ij} = 0$, the weight is set to zero and in bins where $N_{\text{target}}^{ij} = 0$, by construction, the weight is zero. This means all the galaxies in a particular bin, share the same selection weight factor. We then construct the matched control sample by drawing galaxies from the parent sample without replacement, where the probability P_k of selecting galaxy k is given by its normalized weight:

$$P_k = \frac{w_k}{\sum_{m \in S_{\text{parent}}} w_m} \quad (\text{B2})$$

where S_{parent} is the parent sample and m denotes each galaxy in the parent sample. This procedure ensures that the resulting control sample statistically shares the same 2D covariance structure as the target sample. We verify the quality of the match using a two-sample Kolmogorov-Smirnov (KS) test on the marginalized 1D distributions, requiring $p > 0.1$ to confirm that the control and target samples are drawn from effectively the same distribution.

C. MODELING RESULTS FOR INDIVIDUAL GALAXIES

In this appendix, we present the comprehensive modeling results for each galaxy in MAGNUS sample (198 in total). In Table 3, we present the total density slopes derived from six different dynamical models for a representative subset of 10 galaxies. This table is provided to illustrate the format and content of the results. The comprehensive catalog, containing the slope measurements for the entire MAGNUS sample, will be available in a machine-readable format in the online journal.

The figures below (Fig. 13 - 32) display the high-resolution HST imaging alongside the MGE surface brightness models, illustrating the accuracy of our photometric inputs. We further compare the spatially resolved observed V_{rms} maps with the predictions from our best-fitting stars+gNFW JAM_{sph} models to demonstrate the quality of the kinematic fits. Finally, we include the resulting posterior probability distribu-

tions for the total density slope from also the stars+gNFW

JAM_{sph} model to highlight the statistical constraints derived for individual systems.

REFERENCES

Astropy Collaboration. 2013, *A&A*, 558, A33, doi: [10.1051/0004-6361/201322068](https://doi.org/10.1051/0004-6361/201322068)

Astropy Collaboration. 2018, *AJ*, 156, 123, doi: [10.3847/1538-3881/aabc4f](https://doi.org/10.3847/1538-3881/aabc4f)

Auger, M. W., Treu, T., Bolton, A. S., et al. 2010, *ApJ*, 724, 511, doi: [10.1088/0004-637X/724/1/511](https://doi.org/10.1088/0004-637X/724/1/511)

Bacon, R., Conseil, S., Mary, D., Brinchmann, J., et al. 2017, *A&A*, 608, A1, doi: [10.1051/0004-6361/201731128](https://doi.org/10.1051/0004-6361/201731128)

Bacon, R., Accardo, M., Adjali, L., et al. 2010, in Society of Photo-Optical Instrumentation Engineers (SPIE) Conference Series, Vol. 7735, Ground-based and Airborne Instrumentation for Astronomy III, ed. I. S. McLean, S. K. Ramsay, & H. Takami, 773508, doi: [10.1117/12.856027](https://doi.org/10.1117/12.856027)

Barnes, J. E., & Hernquist, L. E. 1991, *ApJL*, 370, L65, doi: [10.1086/185978](https://doi.org/10.1086/185978)

Beifiori, A., Maraston, C., Thomas, D., & Johansson, J. 2011, *A&A*, 531, A109, doi: [10.1051/0004-6361/201016323](https://doi.org/10.1051/0004-6361/201016323)

Bellstedt, S., Forbes, D. A., Romanowsky, A. J., et al. 2018, *MNRAS*, 476, 4543, doi: [10.1093/mnras/sty456](https://doi.org/10.1093/mnras/sty456)

Binney, J., & Tremaine, S. 1987, Galactic dynamics

Blumenthal, G. R., Faber, S. M., Flores, R., & Primack, J. R. 1986, *ApJ*, 301, 27, doi: [10.1086/163867](https://doi.org/10.1086/163867)

Bolton, A. S., Brownstein, J. R., Kochanek, C. S., et al. 2012, *ApJ*, 757, 82, doi: [10.1088/0004-637X/757/1/82](https://doi.org/10.1088/0004-637X/757/1/82)

Bundy, K., Bershady, M. A., Law, D. R., et al. 2015, *ApJ*, 798, 7, doi: [10.1088/0004-637X/798/1/7](https://doi.org/10.1088/0004-637X/798/1/7)

Cappellari, M. 2002, *MNRAS*, 333, 400, doi: [10.1046/j.1365-8711.2002.05412.x](https://doi.org/10.1046/j.1365-8711.2002.05412.x)

Cappellari, M. 2008, *MNRAS*, 390, 71, doi: [10.1111/j.1365-2966.2008.13754.x](https://doi.org/10.1111/j.1365-2966.2008.13754.x)

Cappellari, M. 2016, *ARA&A*, 54, 597, doi: [10.1146/annurev-astro-082214-122432](https://doi.org/10.1146/annurev-astro-082214-122432)

Cappellari, M. 2017, *MNRAS*, 466, 798, doi: [10.1093/mnras/stw3020](https://doi.org/10.1093/mnras/stw3020)

Cappellari, M. 2020, *MNRAS*, 494, 4819, doi: [10.1093/mnras/staa959](https://doi.org/10.1093/mnras/staa959)

Cappellari, M. 2023, *MNRAS*, 526, 3273, doi: [10.1093/mnras/stad2597](https://doi.org/10.1093/mnras/stad2597)

Cappellari, M. 2026a, in Encyclopedia of Astrophysics, Volume 4, Vol. 4, 122–152, doi: [10.1016/B978-0-443-21439-4.00109-7](https://doi.org/10.1016/B978-0-443-21439-4.00109-7)

Cappellari, M. 2026b, arXiv e-prints, arXiv:2601.16179, doi: [10.48550/arXiv.2601.16179](https://doi.org/10.48550/arXiv.2601.16179)

Cappellari, M., & Copin, Y. 2003, *MNRAS*, 342, 345, doi: [10.1046/j.1365-8711.2003.06541.x](https://doi.org/10.1046/j.1365-8711.2003.06541.x)

Cappellari, M., Emsellem, E., Krajnović, D., et al. 2011, *MNRAS*, 413, 813, doi: [10.1111/j.1365-2966.2010.18174.x](https://doi.org/10.1111/j.1365-2966.2010.18174.x)

Cappellari, M., Scott, N., Alatalo, K., et al. 2013a, *MNRAS*, 432, 1709, doi: [10.1093/mnras/stt562](https://doi.org/10.1093/mnras/stt562)

Cappellari, M., McDermid, R. M., Alatalo, K., et al. 2013b, *MNRAS*, 432, 1862, doi: [10.1093/mnras/stt644](https://doi.org/10.1093/mnras/stt644)

Cappellari, M., Romanowsky, A. J., Brodie, J. P., et al. 2015, *ApJL*, 804, L21, doi: [10.1088/2041-8205/804/1/L21](https://doi.org/10.1088/2041-8205/804/1/L21)

Cleveland, W. S., & Devlin, S. J. 1988, *Journal of the American Statistical Association*, 83, 596, <https://api.semanticscholar.org/CorpusID:14960635>

Conroy, C., & Gunn, J. E. 2010, *ApJ*, 712, 833, doi: [10.1088/0004-637X/712/2/833](https://doi.org/10.1088/0004-637X/712/2/833)

Conroy, C., Gunn, J. E., & White, M. 2009, *ApJ*, 699, 486, doi: [10.1088/0004-637X/699/1/486](https://doi.org/10.1088/0004-637X/699/1/486)

Derkenne, C., McDermid, R. M., Poci, A., et al. 2021, *MNRAS*, 506, 3691, doi: [10.1093/mnras/stab1996](https://doi.org/10.1093/mnras/stab1996)

Derkenne, C., McDermid, R. M., Poci, A., et al. 2023, *MNRAS*, 522, 3602, doi: [10.1093/mnras/stad1079](https://doi.org/10.1093/mnras/stad1079)

Dolag, K. 2015, *IAU General Assembly*, 29, 2250156

Dutton, A. A., & Treu, T. 2014, *MNRAS*, 438, 3594, doi: [10.1093/mnras/stt2489](https://doi.org/10.1093/mnras/stt2489)

Emsellem, E., Monnet, G., & Bacon, R. 1994, *A&A*, 285, 723

Etherington, A., Nightingale, J. W., Massey, R., et al. 2023, *MNRAS*, 521, 6005, doi: [10.1093/mnras/stad582](https://doi.org/10.1093/mnras/stad582)

European Southern Observatory (ESO). 2017, MUSE reduced data obtained by standard ESO pipeline processing, co-added across multiple observations, European Southern Observatory (ESO), doi: [10.18727/ARCHIVE/42](https://doi.org/10.18727/ARCHIVE/42)

Foreman-Mackey, D., Hogg, D. W., Lang, D., & Goodman, J. 2013, *PASP*, 125, 306, doi: [10.1086/670067](https://doi.org/10.1086/670067)

Gnedin, O. Y., Kravtsov, A. V., Klypin, A. A., & Nagai, D. 2004, *ApJ*, 616, 16, doi: [10.1086/424914](https://doi.org/10.1086/424914)

Governato, F., Brook, C., Mayer, L., et al. 2010, *Nature*, 463, 203, doi: [10.1038/nature08640](https://doi.org/10.1038/nature08640)

Harris, C. R., Millman, K. J., van der Walt, S. J., et al. 2020, *Nature*, 585, 357, doi: [10.1038/s41586-020-2649-2](https://doi.org/10.1038/s41586-020-2649-2)

Hilz, M., Naab, T., & Ostriker, J. P. 2013, *MNRAS*, 429, 2924, doi: [10.1093/mnras/sts501](https://doi.org/10.1093/mnras/sts501)

Hoaglin, D. C., Mosteller, F., & Tukey, J. W. 1983, Understanding robust and exploratory data analysis

Hogg, D. W., Baldry, I. K., Blanton, M. R., & Eisenstein, D. J. 2002, arXiv e-prints, astro, doi: [10.48550/arXiv.astro-ph/0210394](https://doi.org/10.48550/arXiv.astro-ph/0210394)

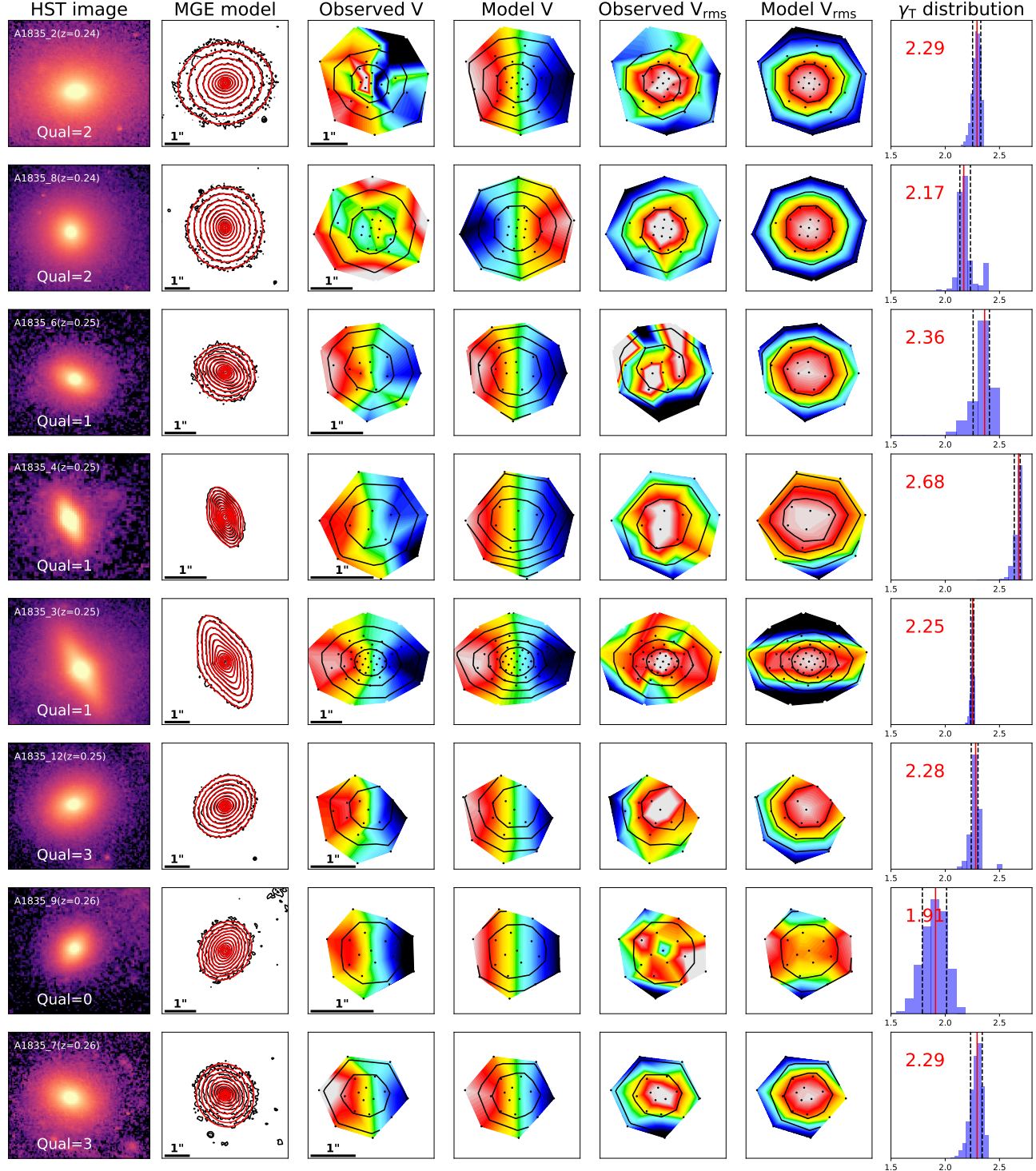


Figure 13. Spatially resolved modeling results for the MAGNUS sample using the stars+gNFW withJAM_{sph} model. Each row corresponds to one galaxy and displays, from left to right: (1) HST imaging, with the galaxy ID and redshift (z) indicated at the top and the visual quality assessment of the dynamical model at the bottom; (2) Multi-Gaussian Expansion (MGE) fit, where black and red contours represent the observed and modeled surface brightness, respectively; (3–6) Observed and modeled stellar kinematics, showing the mean velocity (V) and root-mean-square velocity (V_{rms}) fields. All kinematic maps are rotated to align the major axis with the x -direction. Black contours in the kinematic panels trace the surface brightness isophotes of the corresponding data (observed or modeled), while white circles denote clipped bins excluded from the JAMPY fit. A $1''$ scale bar is provided in the MGE panel (for imaging) and the observed velocity panel (for kinematics); (7) Posterior probability distribution of the total density slope, γ_T . The solid red line and numerical value indicate the median slope, while vertical black dashed lines mark the 16th and 84th percentiles.

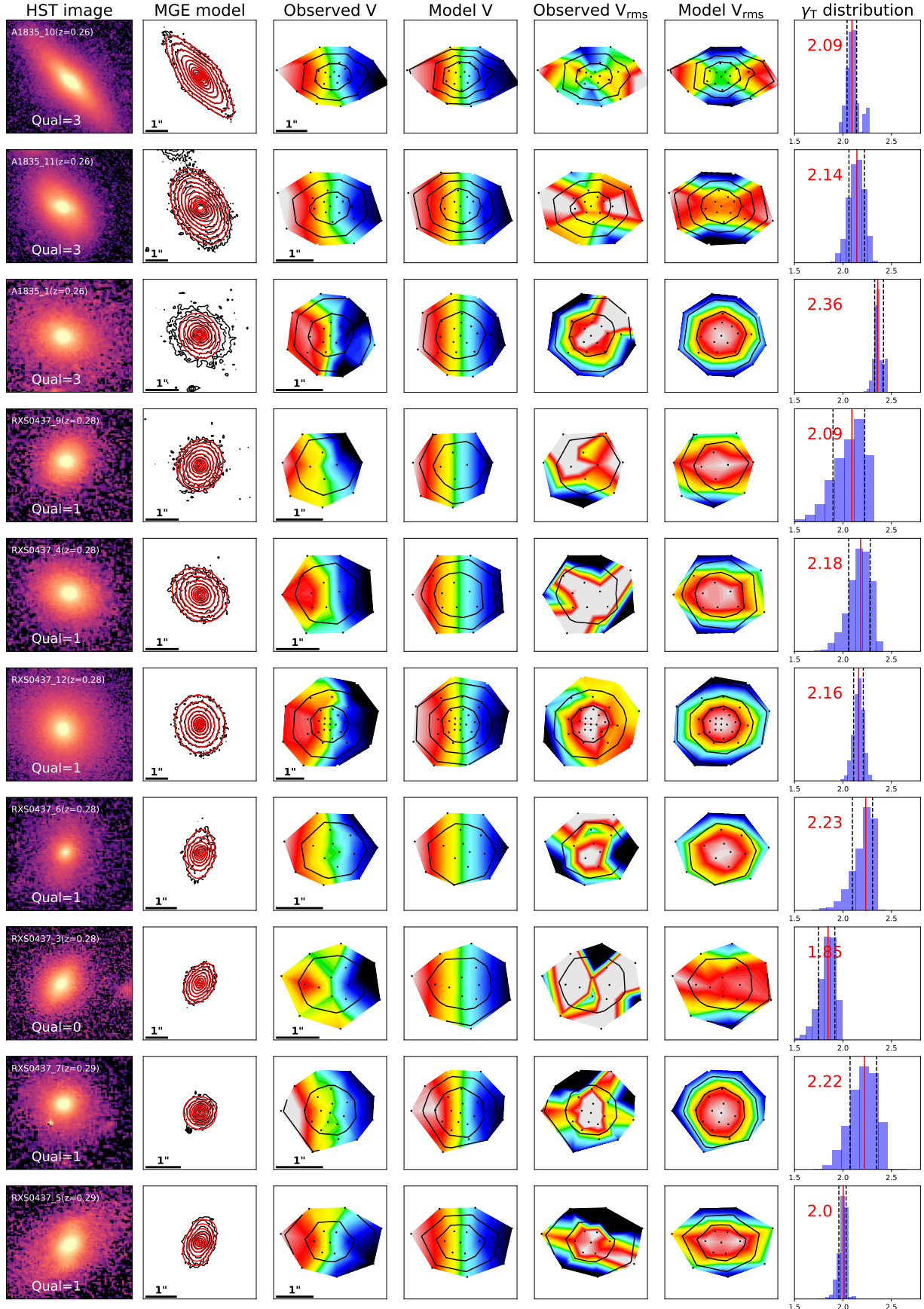


Figure 14. Same as Fig. 13

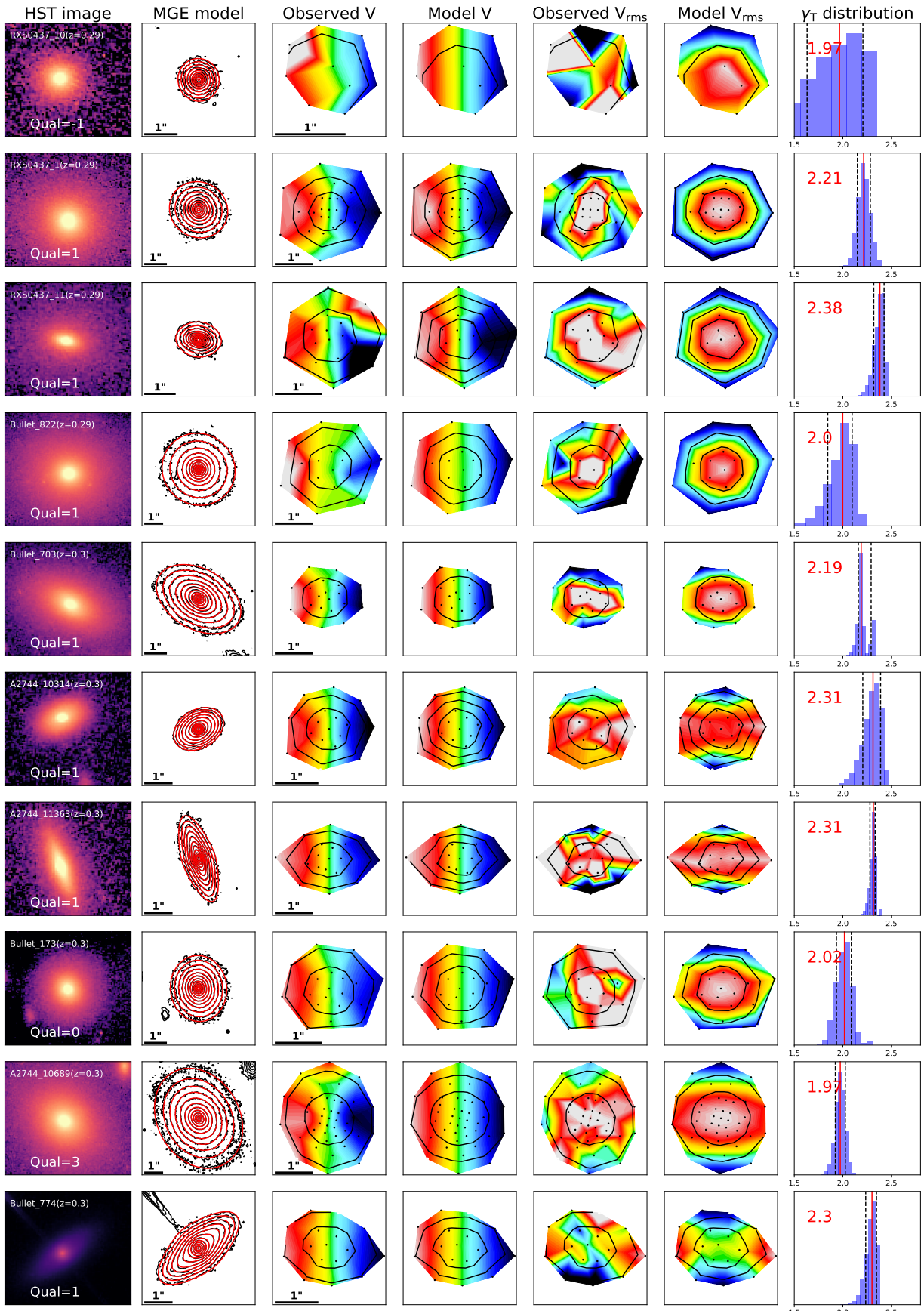


Figure 15. Same as Fig. 13

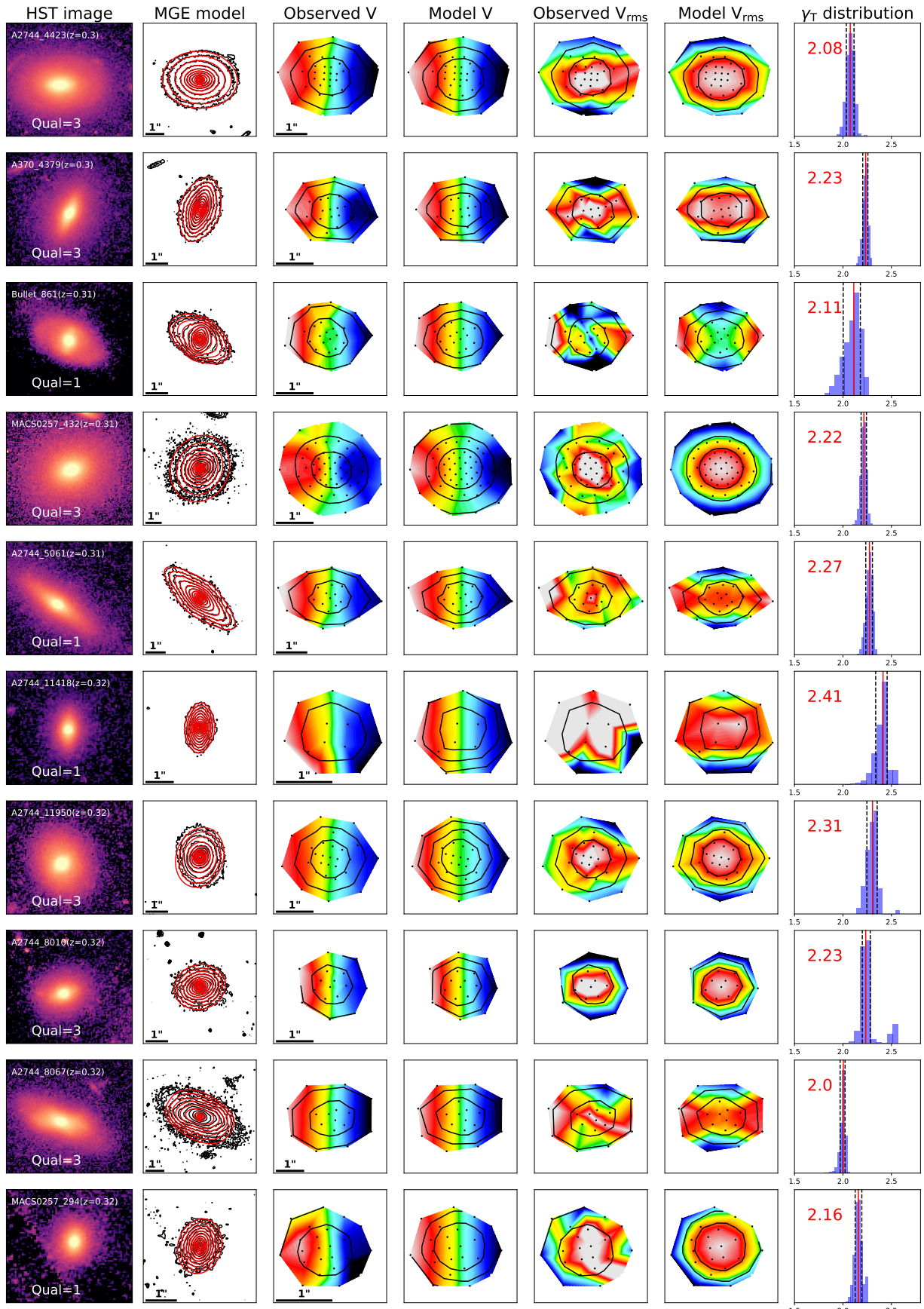


Figure 16. Same as Fig. 13

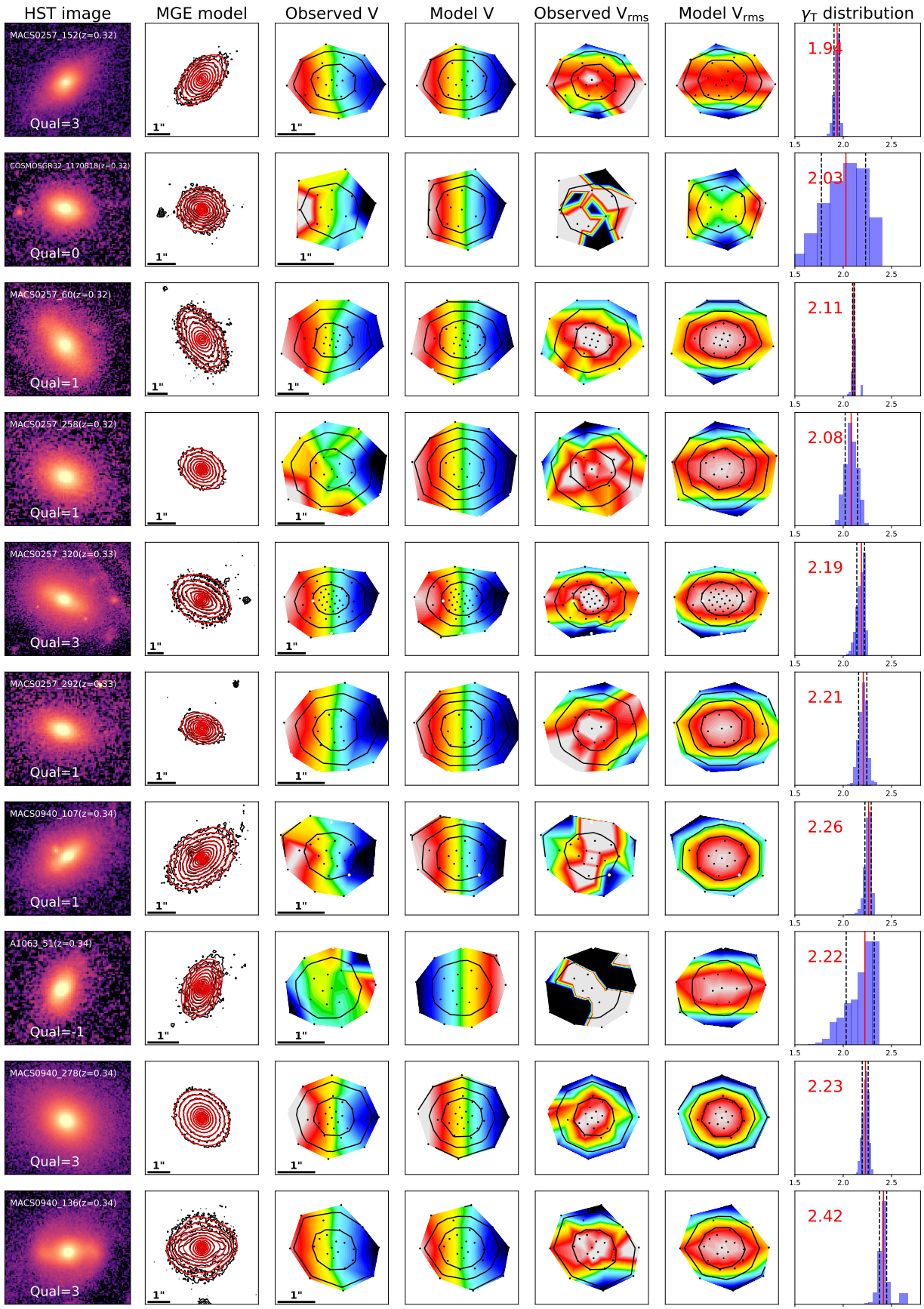


Figure 17. Same as Fig. 13

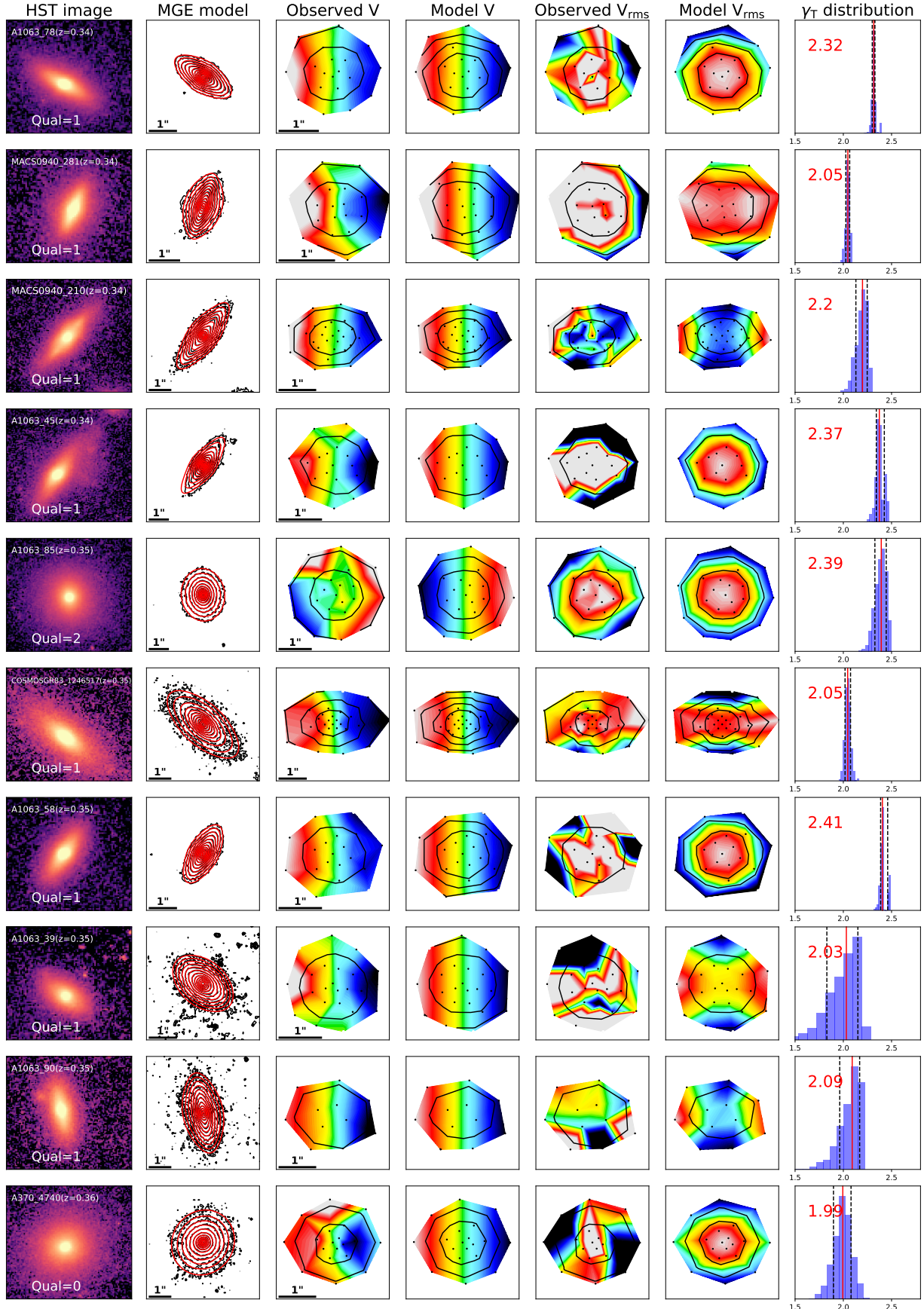


Figure 18. Same as Fig. 13

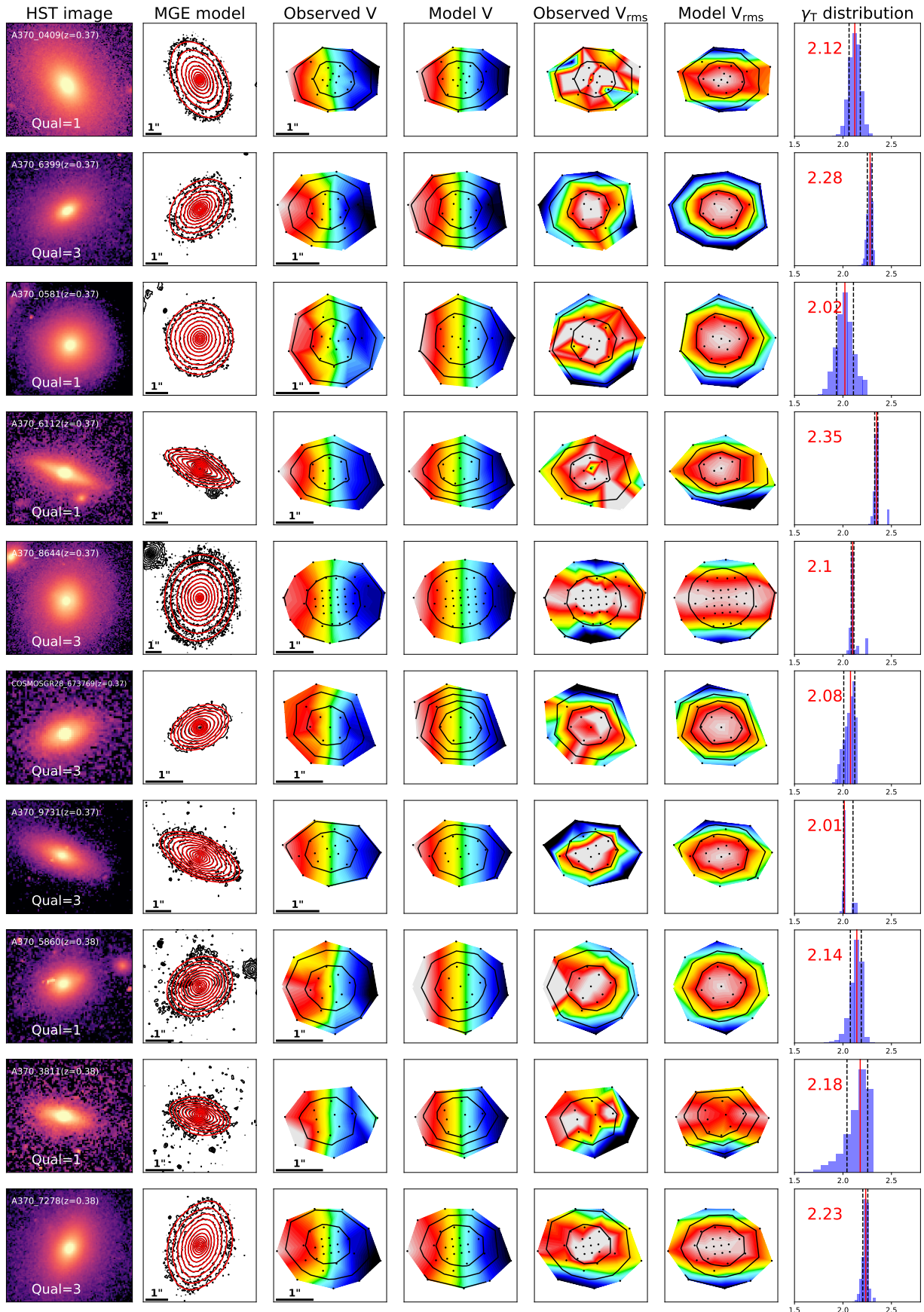


Figure 19. Same as Fig. 13

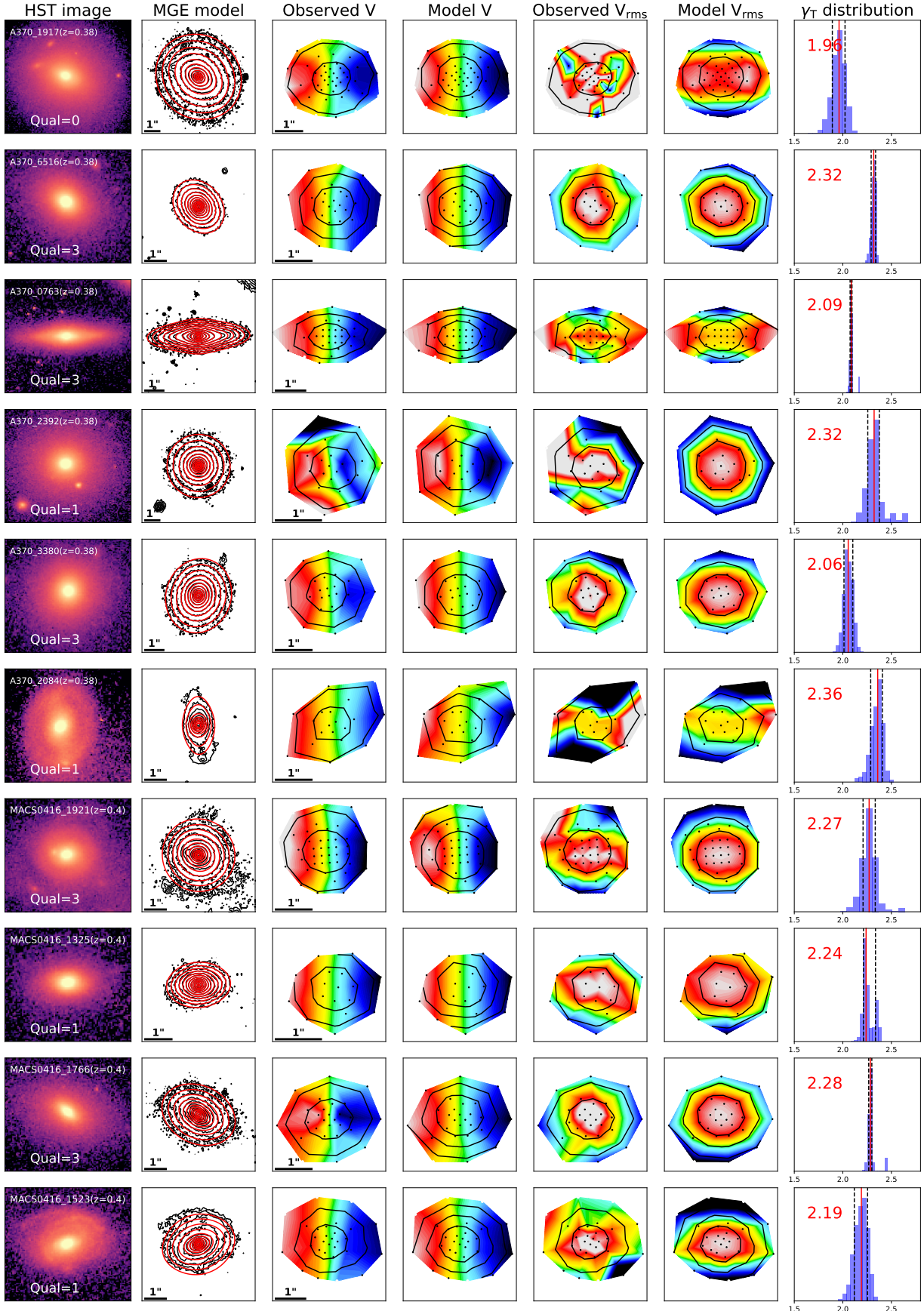


Figure 20. Same as Fig. 13

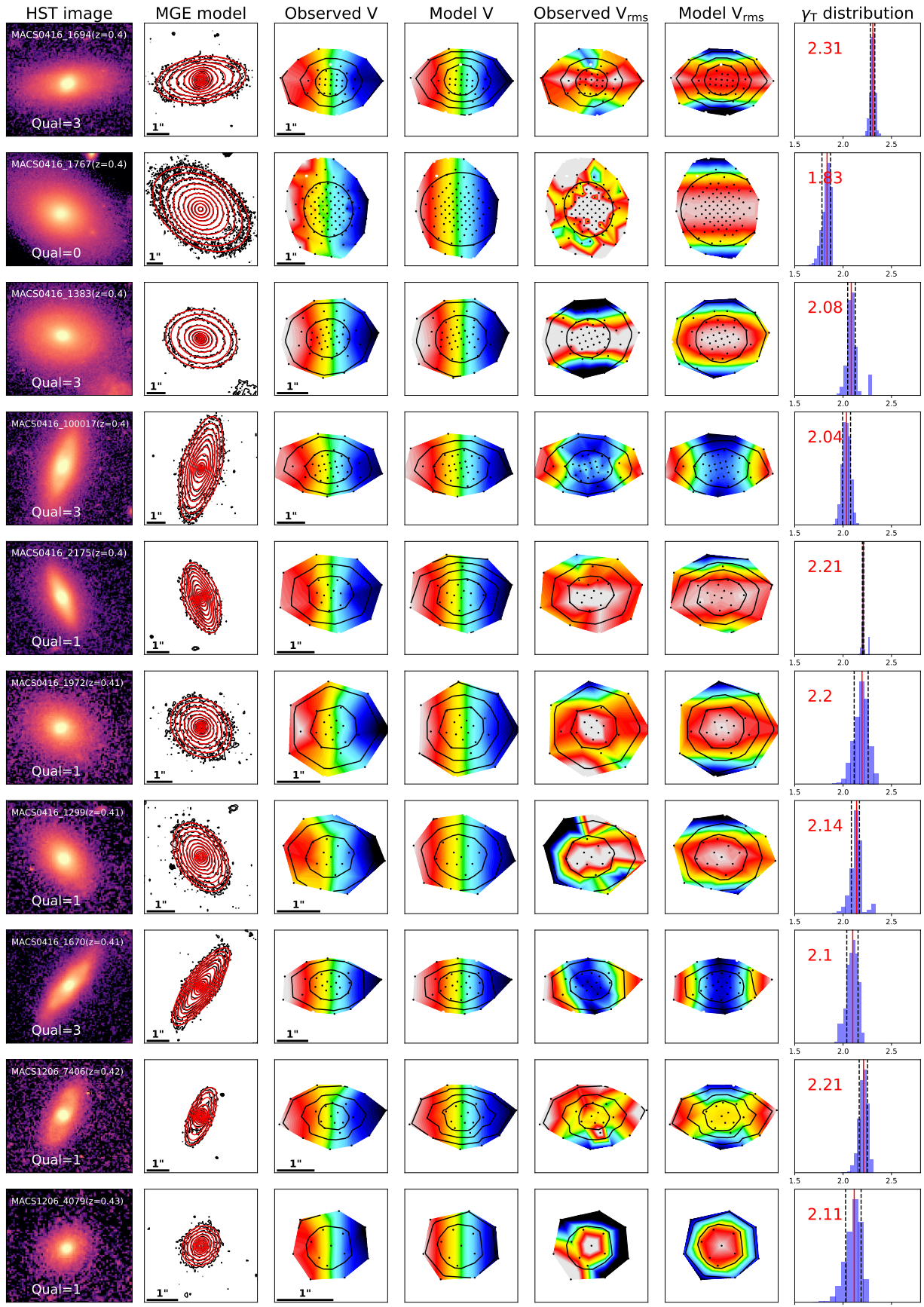


Figure 21. Same as Fig. 13

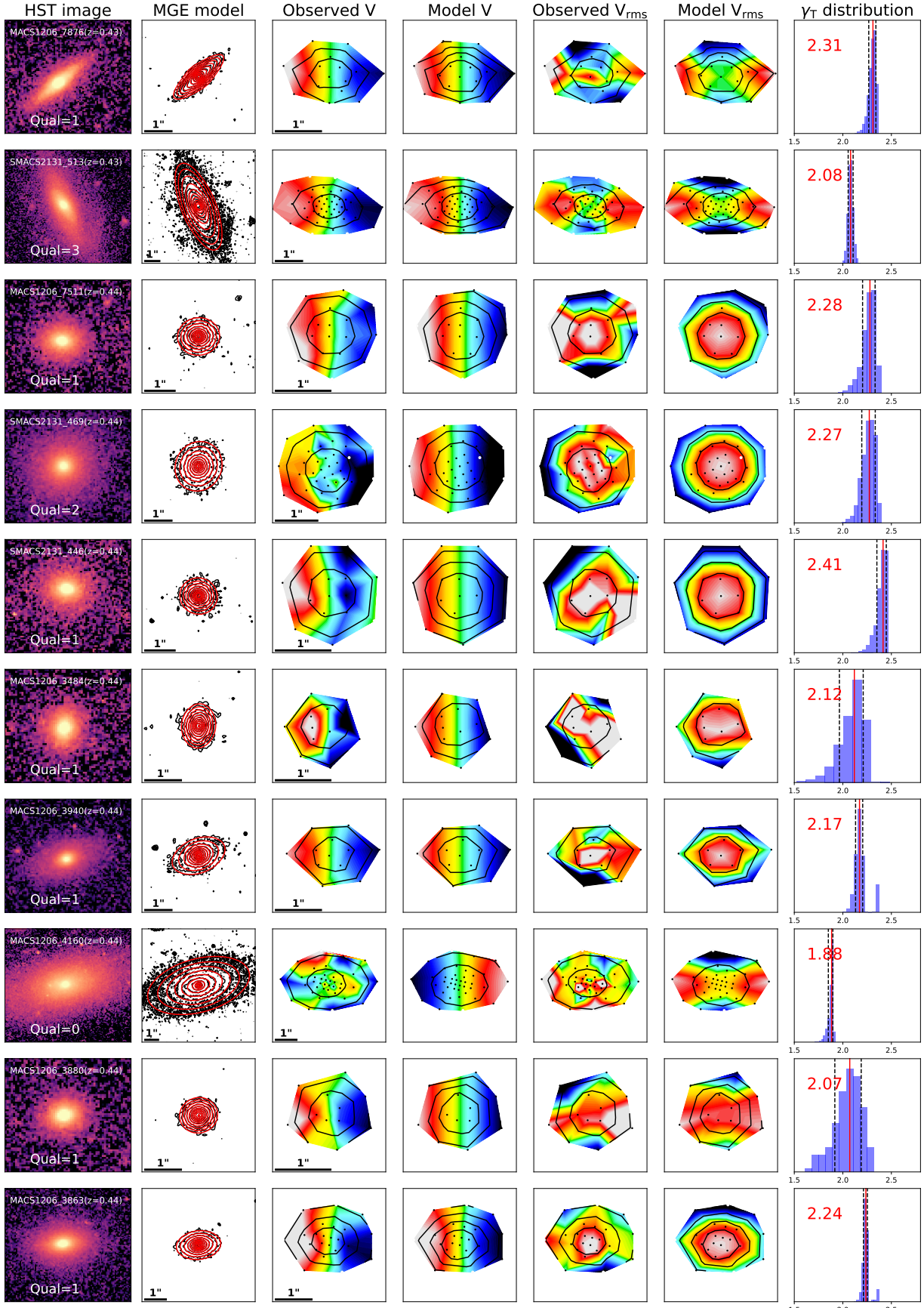


Figure 22. Same as Fig. 13

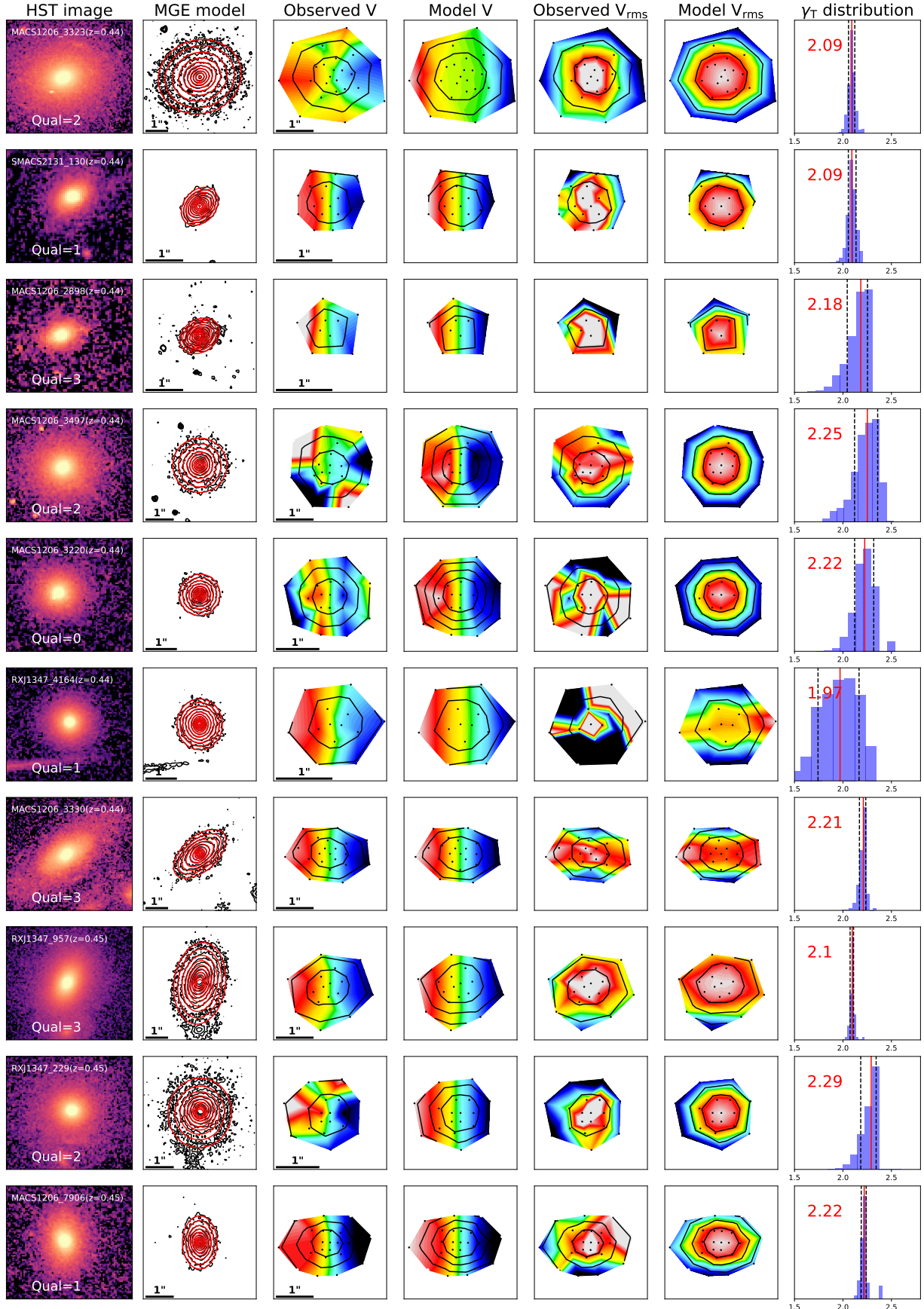


Figure 23. Same as Fig. 13

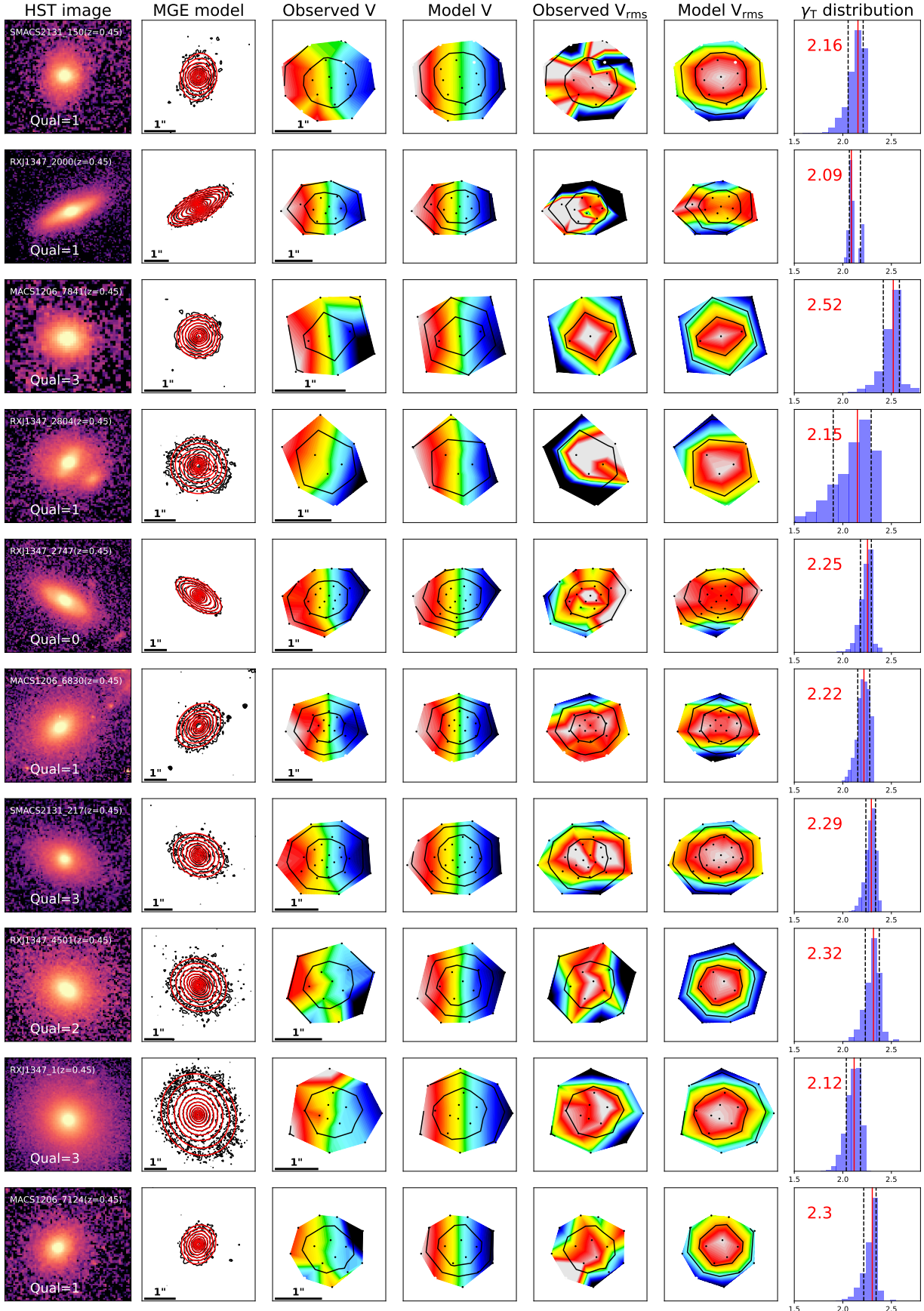


Figure 24. Same as Fig. 13

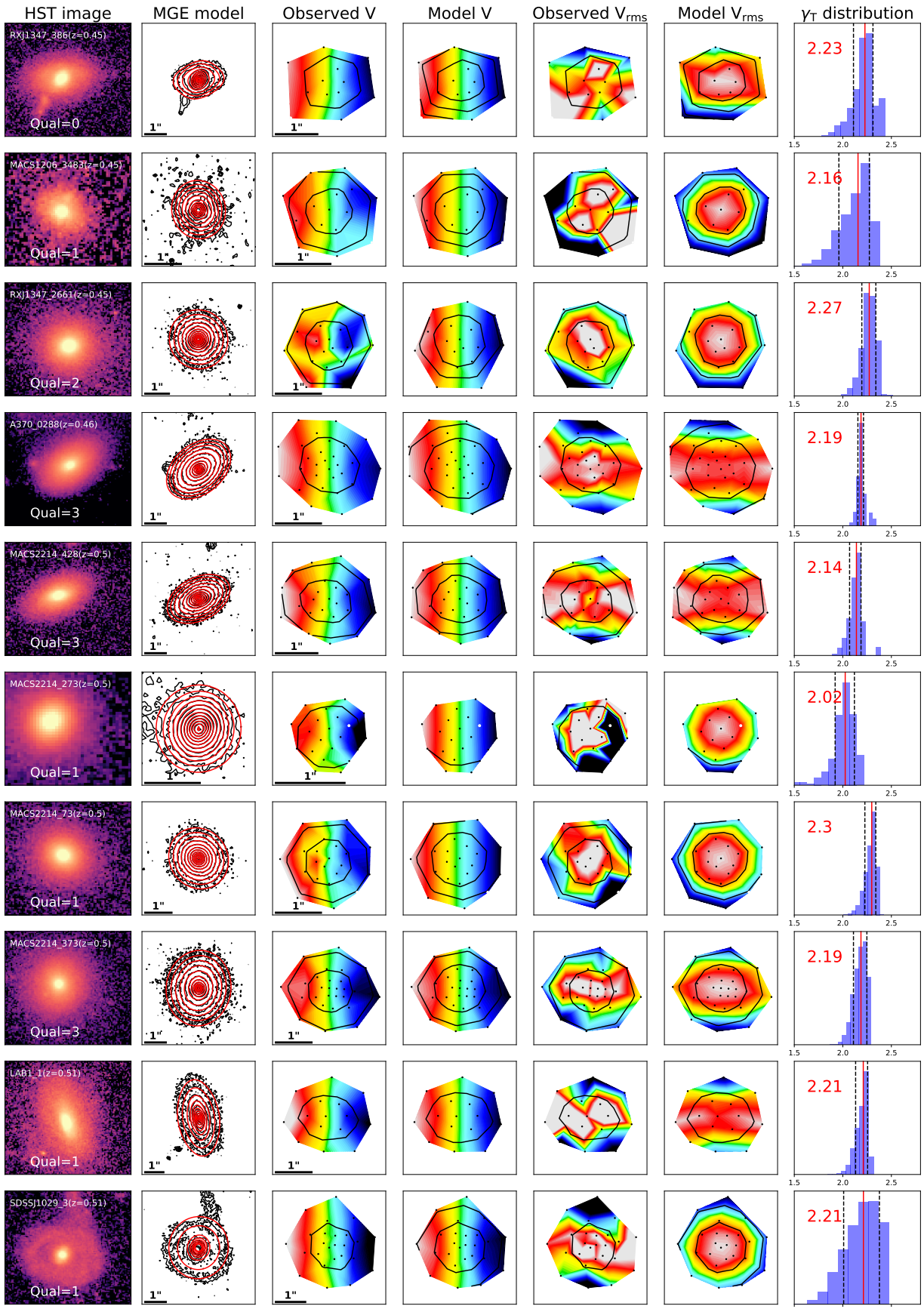


Figure 25. Same as Fig. 13

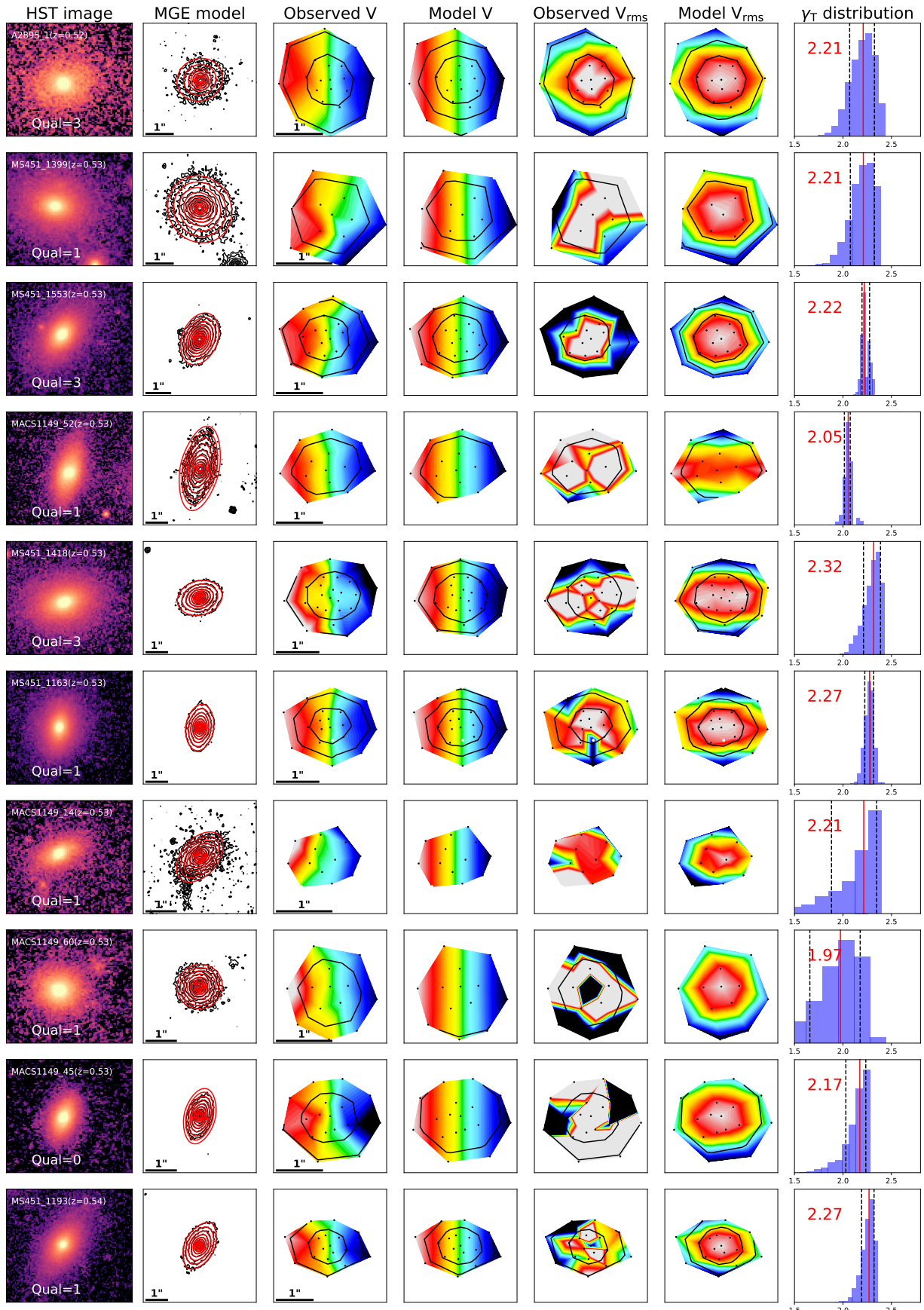


Figure 26. Same as Fig. 13

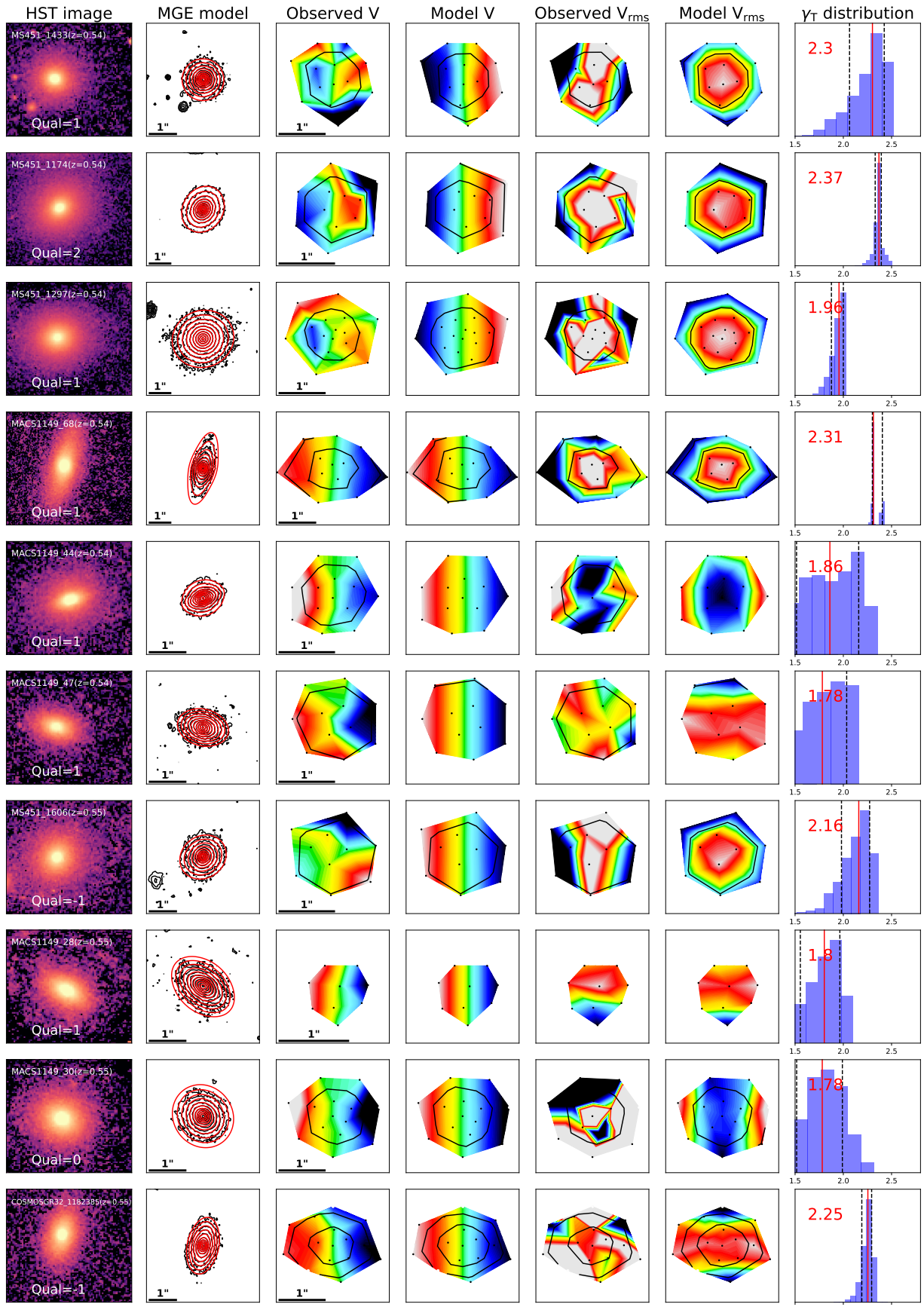


Figure 27. Same as Fig. 13

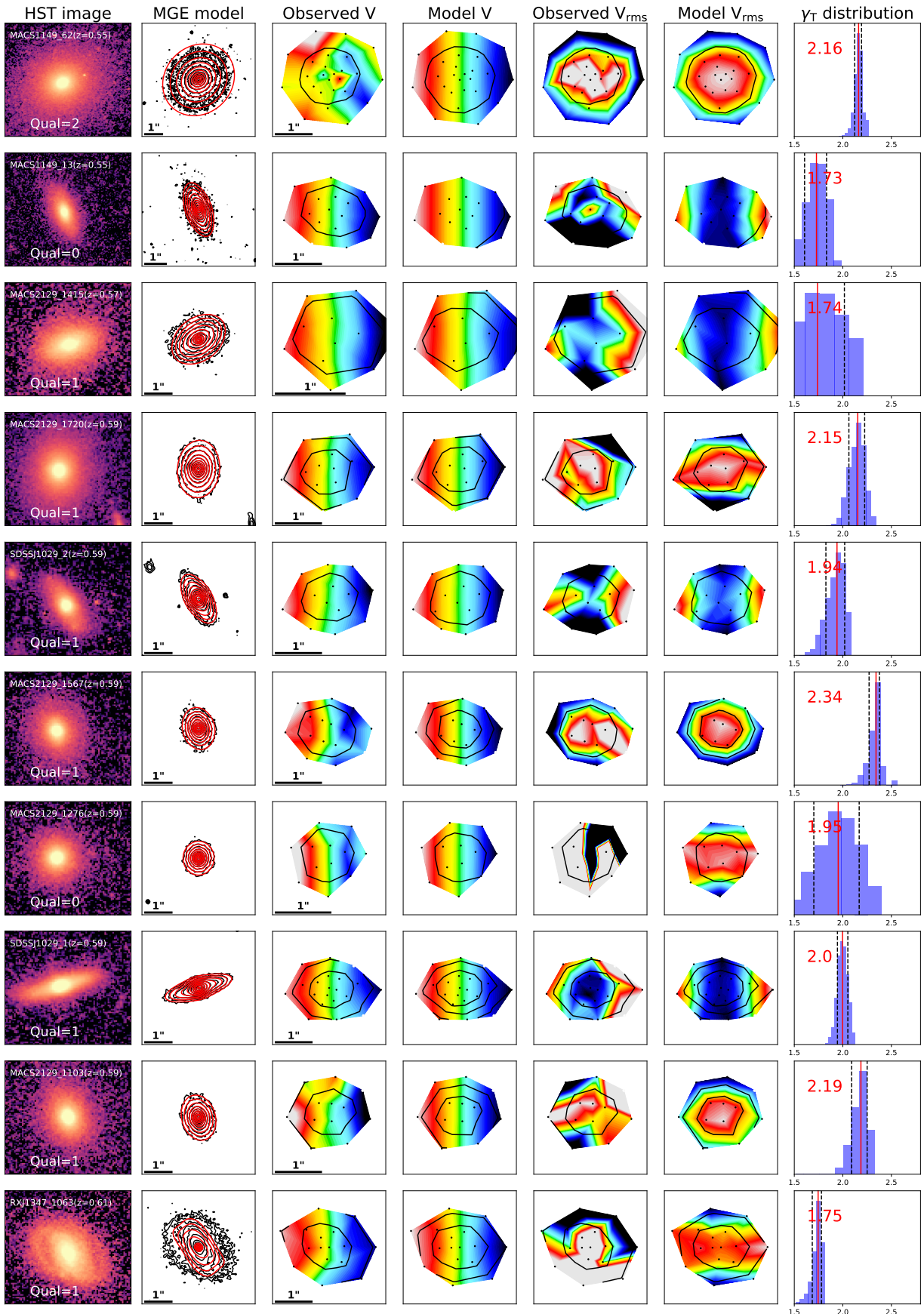


Figure 28. Same as Fig. 13

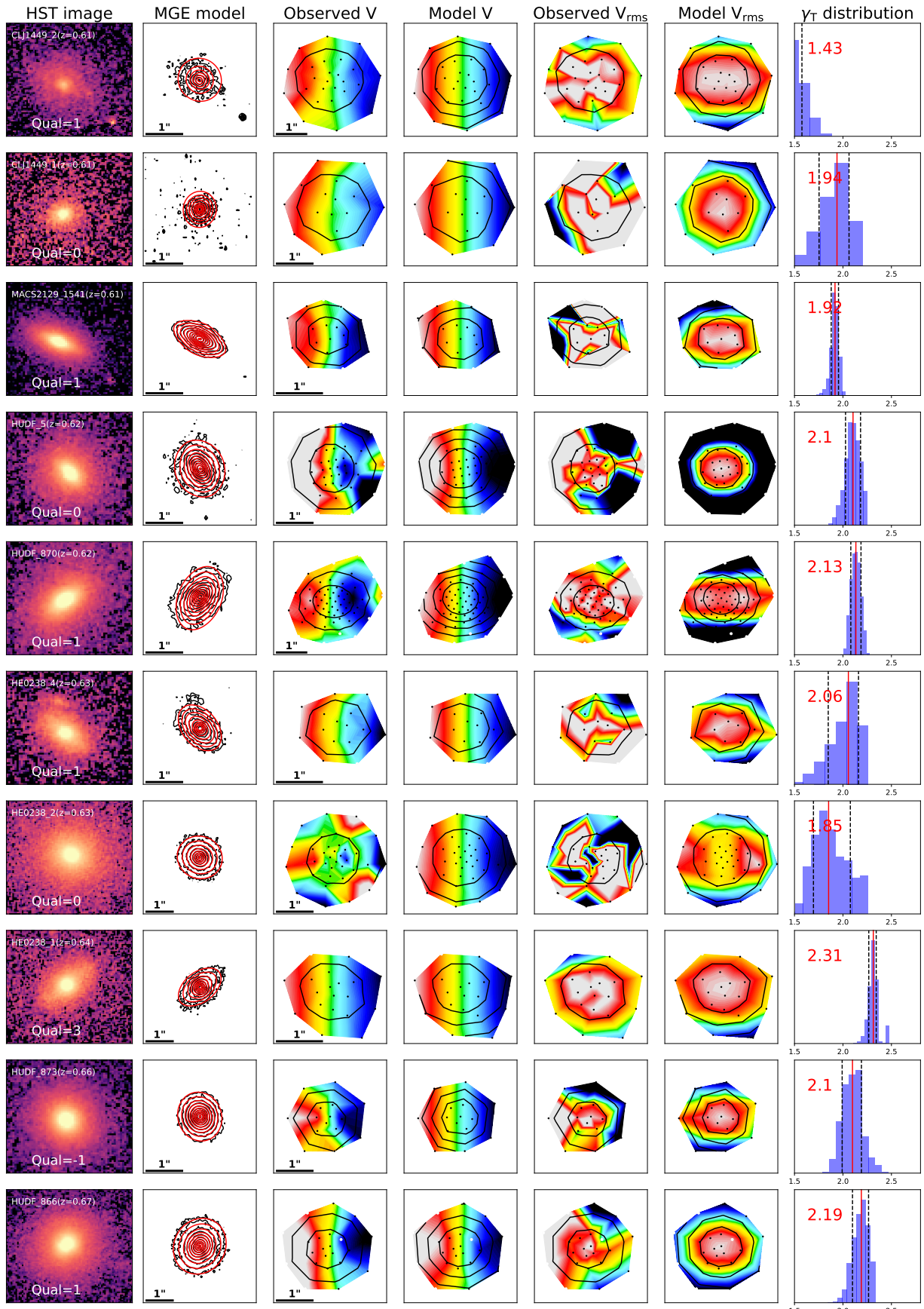


Figure 29. Same as Fig. 13

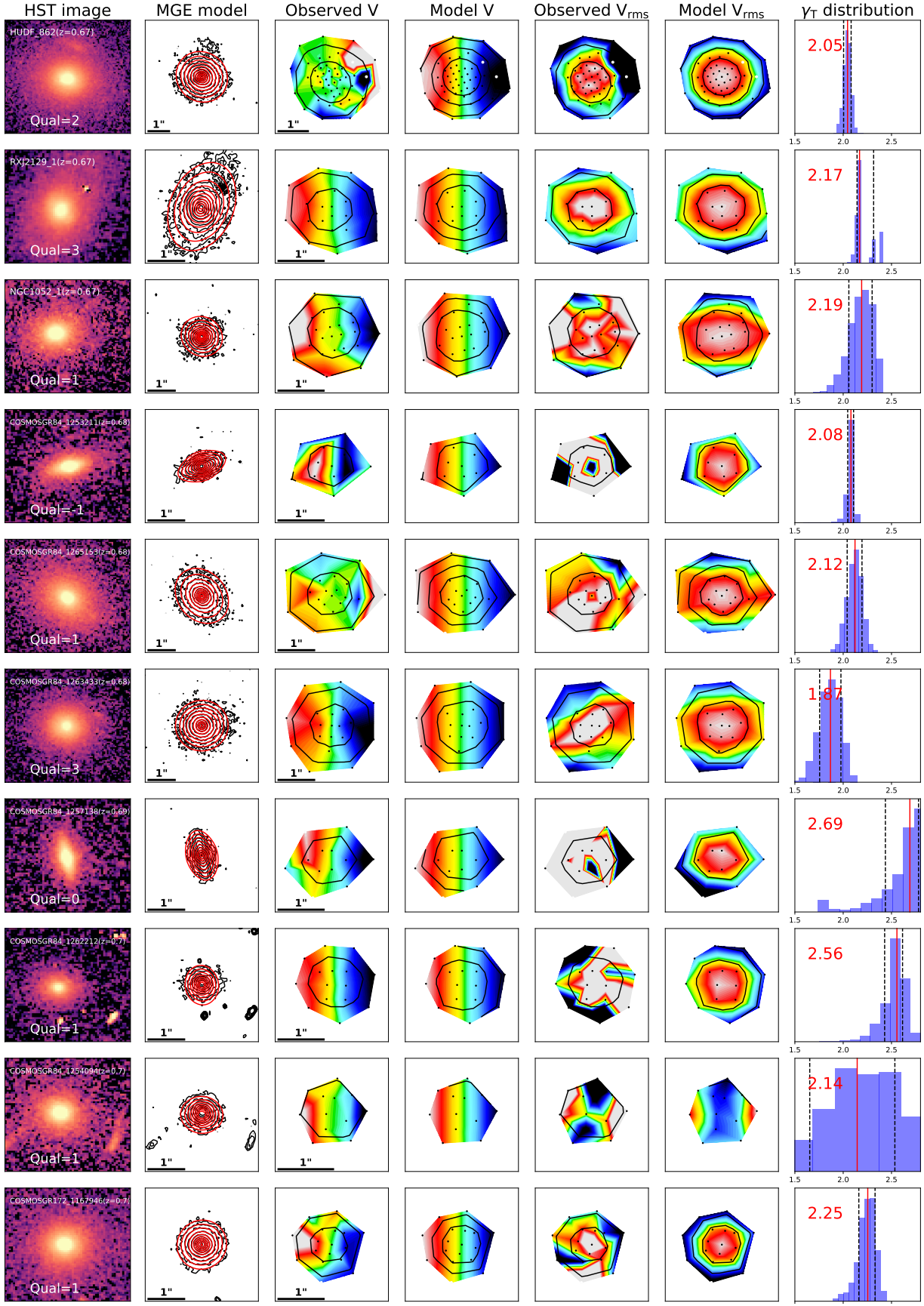


Figure 30. Same as Fig. 13

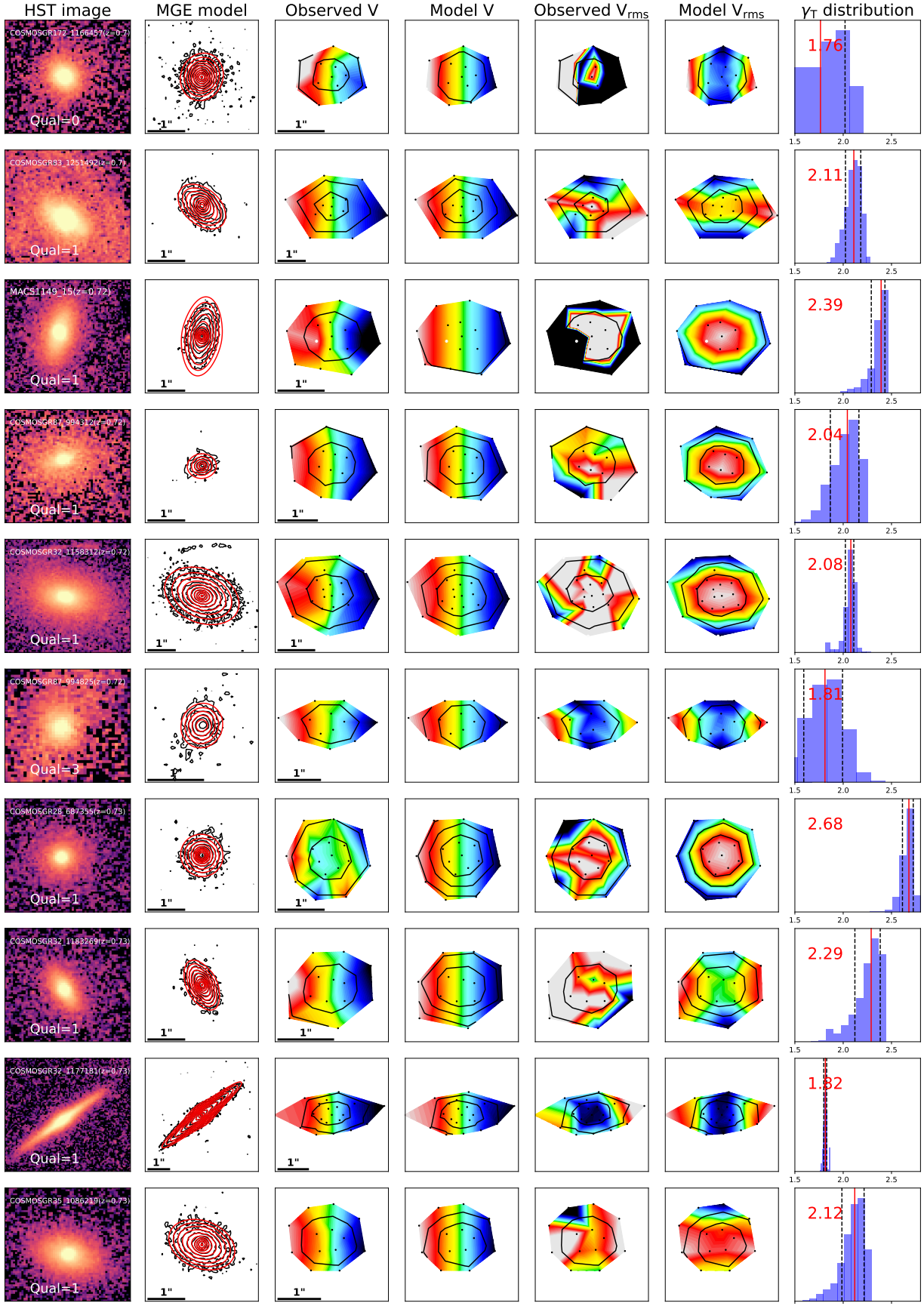


Figure 31. Same as Fig. 13

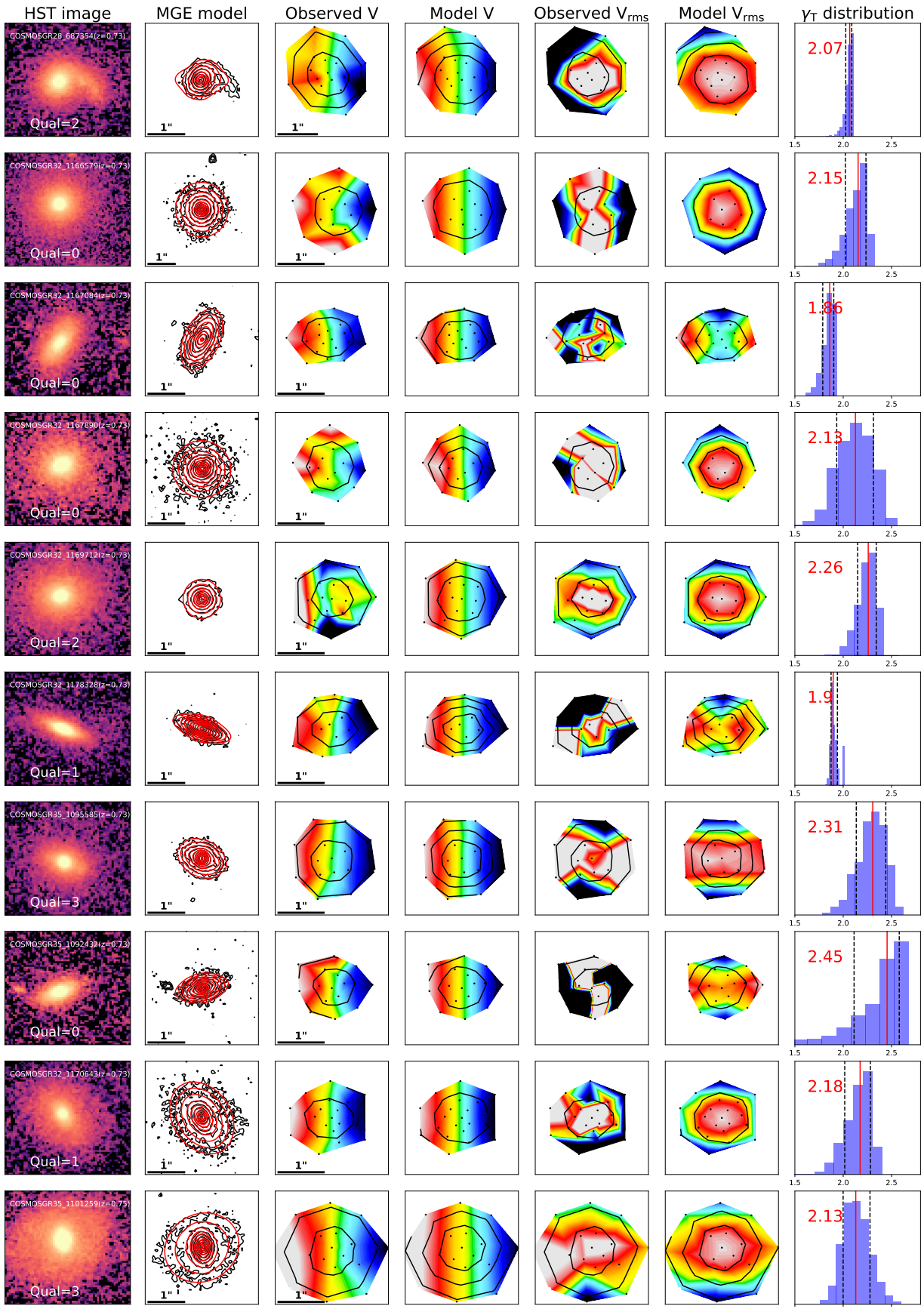


Figure 32. Same as Fig. 13

Table 3. Mass-weighted total density slope, γ_T from six dynamical models and visual quality classification of the models.

Galaxy	γ_T	γ_T	γ_T	γ_T	γ_T	γ_T	γ_T	Quality
ID	(power-law with JAM _{cyl})	(power-law with JAM _{sph})	(stars+NFW with JAM _{cyl})	(stars+NFW with JAM _{sph})	(stars+gNFW with JAM _{cyl})	(stars+gNFW with JAM _{sph})		
A1063_90	2.11 ^{+0.22} _{-0.21}	2.09 ^{+0.23} _{-0.21}	2.11 ^{+0.13} _{-0.07}	2.11 ^{+0.10} _{-0.07}	2.10 ^{+0.12} _{-0.07}	2.09 ^{+0.13} _{-0.08}	1	
A2744_11950	2.21 ^{+0.06} _{-0.08}	2.20 ^{+0.04} _{-0.06}	2.29 ^{+0.02} _{-0.02}	2.30 ^{+0.03} _{-0.02}	2.34 ^{+0.06} _{-0.25}	2.31 ^{+0.06} _{-0.04}	3	
A370_0409	2.10 ^{+0.06} _{-0.05}	2.12 ^{+0.07} _{-0.06}	2.10 ^{+0.06} _{-0.06}	2.11 ^{+0.05} _{-0.06}	2.11 ^{+0.08} _{-0.06}	2.12 ^{+0.06} _{-0.06}	1	
A370_7278	2.25 ^{+0.07} _{-0.07}	2.25 ^{+0.06} _{-0.07}	2.25 ^{+0.03} _{-0.12}	2.23 ^{+0.03} _{-0.02}	2.24 ^{+0.03} _{-0.03}	2.23 ^{+0.03} _{-0.03}	3	
A370_9731	2.39 ^{+0.07} _{-0.03}	2.40 ^{+0.08} _{-0.09}	2.00 ^{+0.05} _{-0.02}	2.01 ^{+0.00} _{-0.08}	2.00 ^{+0.05} _{-0.02}	2.01 ^{+0.00} _{-0.09}	3	
HE0238_1	2.34 ^{+0.09} _{-0.06}	2.30 ^{+0.13} _{-0.09}	2.31 ^{+0.04} _{-0.03}	2.32 ^{+0.05} _{-0.02}	2.31 ^{+0.05} _{-0.03}	2.31 ^{+0.04} _{-0.03}	3	
LAB1_1	2.30 ^{+0.14} _{-0.12}	2.31 ^{+0.15} _{-0.10}	2.20 ^{+0.08} _{-0.05}	2.21 ^{+0.08} _{-0.04}	2.21 ^{+0.07} _{-0.04}	2.21 ^{+0.08} _{-0.05}	1	
MACS1206_3863	2.33 ^{+0.08} _{-0.06}	2.36 ^{+0.07} _{-0.04}	2.23 ^{+0.03} _{-0.02}	2.23 ^{+0.02} _{-0.02}	2.23 ^{+0.02} _{-0.02}	2.24 ^{+0.03} _{-0.01}	1	
RXS0437_11	2.30 ^{+0.08} _{-0.08}	2.30 ^{+0.09} _{-0.08}	2.38 ^{+0.05} _{-0.04}	2.37 ^{+0.04} _{-0.04}	2.38 ^{+0.06} _{-0.04}	2.38 ^{+0.06} _{-0.04}	1	
SMACS2131_217	2.18 ^{+0.07} _{-0.08}	2.17 ^{+0.06} _{-0.07}	2.29 ^{+0.05} _{-0.05}	2.29 ^{+0.05} _{-0.05}	2.29 ^{+0.07} _{-0.05}	2.29 ^{+0.05} _{-0.05}	3	

Hopkins, P. F., Cox, T. J., Younger, J. D., & Hernquist, L. 2009, *ApJ*, 691, 1168, doi: [10.1088/0004-637X/691/2/1168](https://doi.org/10.1088/0004-637X/691/2/1168)

Knabel, S., Mozumdar, P., Shajib, A. J., et al. 2025, arXiv e-prints, arXiv:2502.16034, doi: [10.48550/arXiv.2502.16034](https://doi.org/10.48550/arXiv.2502.16034)

Koopmans, L. V. E., Treu, T., Bolton, A. S., Burles, S., & Moustakas, L. A. 2006, *ApJ*, 649, 599, doi: [10.1086/505696](https://doi.org/10.1086/505696)

Law, D. R., Cherinka, B., Yan, R., et al. 2016, *AJ*, 152, 83, doi: [10.3847/0004-6256/152/4/83](https://doi.org/10.3847/0004-6256/152/4/83)

Li, R., Shu, Y., & Wang, J. 2018, *MNRAS*, 480, 431, doi: [10.1093/mnras/sty1813](https://doi.org/10.1093/mnras/sty1813)

Li, R., Li, H., Shao, S., et al. 2019, *MNRAS*, 490, 2124, doi: [10.1093/mnras/stz2565](https://doi.org/10.1093/mnras/stz2565)

Li, S., Li, R., Zhu, K., et al. 2024, *MNRAS*, 529, 4633, doi: [10.1093/mnras/stae838](https://doi.org/10.1093/mnras/stae838)

Lotz, J. M., Koekemoer, A., Coe, D., et al. 2017, *ApJ*, 837, doi: [10.3847/1538-4357/837/1/97](https://doi.org/10.3847/1538-4357/837/1/97)

Lu, S., Zhu, K., Cappellari, M., et al. 2023, *MNRAS*, 526, 1022, doi: [10.1093/mnras/stad2732](https://doi.org/10.1093/mnras/stad2732)

Mozumdar, P., Cappellari, M., Fassnacht, C. D., & Treu, T. 2025a, arXiv e-prints, arXiv:2510.23863, doi: [10.48550/arXiv.2510.23863](https://doi.org/10.48550/arXiv.2510.23863)

Mozumdar, P., Cappellari, M., Fassnacht, C. D., & Treu, T. 2025b, arXiv e-prints, arXiv:2510.23888, doi: [10.48550/arXiv.2510.23888](https://doi.org/10.48550/arXiv.2510.23888)

Mozumdar, P., Knabel, S., Treu, T., et al. 2025c, arXiv e-prints, arXiv:2505.13962, doi: [10.48550/arXiv.2505.13962](https://doi.org/10.48550/arXiv.2505.13962)

Mukherjee, S., Koopmans, L. V. E., Metcalf, R. B., et al. 2021, *MNRAS*, 504, 3455, doi: [10.1093/mnras/stab693](https://doi.org/10.1093/mnras/stab693)

Naab, T., Johansson, P. H., & Ostriker, J. P. 2009, *ApJL*, 699, L178, doi: [10.1088/0004-637X/699/2/L178](https://doi.org/10.1088/0004-637X/699/2/L178)

Naab, T., & Ostriker, J. P. 2017, *ARA&A*, 55, 59, doi: [10.1146/annurev-astro-081913-040019](https://doi.org/10.1146/annurev-astro-081913-040019)

Navarro, J. F., Frenk, C. S., & White, S. D. M. 1996, *ApJ*, 462, 563, doi: [10.1086/177173](https://doi.org/10.1086/177173)

Nipoti, C., Treu, T., Auger, M. W., & Bolton, A. S. 2009a, *ApJL*, 706, L86, doi: [10.1088/0004-637X/706/1/L86](https://doi.org/10.1088/0004-637X/706/1/L86)

Nipoti, C., Treu, T., & Bolton, A. S. 2009b, *ApJ*, 703, 1531, doi: [10.1088/0004-637X/703/2/1531](https://doi.org/10.1088/0004-637X/703/2/1531)

Oser, L., Ostriker, J. P., Naab, T., Johansson, P. H., & Burkert, A. 2010, *ApJ*, 725, 2312, doi: [10.1088/0004-637X/725/2/2312](https://doi.org/10.1088/0004-637X/725/2/2312)

Patel, S. G., van Dokkum, P. G., Franx, M., et al. 2013, *ApJ*, 766, 15, doi: [10.1088/0004-637X/766/1/15](https://doi.org/10.1088/0004-637X/766/1/15)

Peirani, S., Sonnenfeld, A., Gavazzi, R., et al. 2019, *MNRAS*, 483, 4615, doi: [10.1093/mnras/sty3475](https://doi.org/10.1093/mnras/sty3475)

Pillepich, A., Springel, V., Nelson, D., et al. 2018, *MNRAS*, 473, 4077, doi: [10.1093/mnras/stx2656](https://doi.org/10.1093/mnras/stx2656)

Poci, A., Cappellari, M., & McDermid, R. M. 2017, *MNRAS*, 467, 1397, doi: [10.1093/mnras/stx101](https://doi.org/10.1093/mnras/stx101)

Remus, R.-S., Dolag, K., Naab, T., et al. 2017, *MNRAS*, 464, 3742, doi: [10.1093/mnras/stw2594](https://doi.org/10.1093/mnras/stw2594)

Ruff, A. J., Gavazzi, R., Marshall, P. J., et al. 2011, *ApJ*, 727, 96, doi: [10.1088/0004-637X/727/2/96](https://doi.org/10.1088/0004-637X/727/2/96)

Sahu, N., Tran, K.-V., Suyu, S. H., et al. 2024, *ApJ*, 970, 86, doi: [10.3847/1538-4357/ad4ce3](https://doi.org/10.3847/1538-4357/ad4ce3)

Salpeter, E. E. 1955, *ApJ*, 121, 161, doi: [10.1086/145971](https://doi.org/10.1086/145971)

Scoville, N., Aussel, H., Brusa, M., Capak, P., et al. 2007, *ApJS*, 172, doi: [10.1086/516585](https://doi.org/10.1086/516585)

Sonnenfeld, A., Treu, T., Gavazzi, R., et al. 2013, *ApJ*, 777, 98, doi: [10.1088/0004-637X/777/2/98](https://doi.org/10.1088/0004-637X/777/2/98)

Tan, C. Y., Shajib, A. J., Birrer, S., et al. 2024, *MNRAS*, 530, 1474, doi: [10.1093/mnras/stae884](https://doi.org/10.1093/mnras/stae884)

Treu, T., & Koopmans, L. V. E. 2002, *ApJ*, 575, 87, doi: [10.1086/341216](https://doi.org/10.1086/341216)

Treu, T., & Koopmans, L. V. E. 2004, *ApJ*, 611, 739, doi: [10.1086/422245](https://doi.org/10.1086/422245)

Valdes, F., Gupta, R., Rose, J. A., Singh, H. P., & Bell, D. J. 2004, *ApJS*, 152, 251, doi: [10.1086/386343](https://doi.org/10.1086/386343)

van Dokkum, P. G., Whitaker, K. E., Brammer, G., et al. 2010, *ApJ*, 709, 1018, doi: [10.1088/0004-637X/709/2/1018](https://doi.org/10.1088/0004-637X/709/2/1018)

van Dokkum, P. G., Nelson, E. J., Franx, M., et al. 2015, *ApJ*, 813, 23, doi: [10.1088/0004-637X/813/1/23](https://doi.org/10.1088/0004-637X/813/1/23)

van Houtd, J., van der Wel, A., Bezanson, R., et al. 2021, *ApJ*, 923, 11, doi: [10.3847/1538-4357/ac1f29](https://doi.org/10.3847/1538-4357/ac1f29)

Verro, K., Trager, S. C., Peletier, R. F., et al. 2022, *A&A*, 660, A34, doi: [10.1051/0004-6361/202142388](https://doi.org/10.1051/0004-6361/202142388)

Virtanen, P., Gommers, R., Oliphant, T. E., et al. 2020, *Nature Methods*, 17, 261, doi: [10.1038/s41592-019-0686-2](https://doi.org/10.1038/s41592-019-0686-2)

Wake, D. A., Bundy, K., Diamond-Stanic, A. M., et al. 2017, *AJ*, 154, 86, doi: [10.3847/1538-3881/aa7ecc](https://doi.org/10.3847/1538-3881/aa7ecc)

Wang, Y., Vogelsberger, M., Xu, D., et al. 2019, *MNRAS*, 490, 5722, doi: [10.1093/mnras/stz2907](https://doi.org/10.1093/mnras/stz2907)

Wang, Y., Vogelsberger, M., Xu, D., et al. 2020, *MNRAS*, 491, 5188, doi: [10.1093/mnras/stz3348](https://doi.org/10.1093/mnras/stz3348)

Weilbacher, P. M., Palsa, R., Streicher, O., et al. 2020, *A&A*, 641, A28, doi: [10.1051/0004-6361/202037855](https://doi.org/10.1051/0004-6361/202037855)

Westfall, K. B., Cappellari, M., Bershady, M. A., et al. 2019, *AJ*, 158, 231, doi: [10.3847/1538-3881/ab44a2](https://doi.org/10.3847/1538-3881/ab44a2)

White, S. D. M., & Frenk, C. S. 1991, *ApJ*, 379, 52, doi: [10.1086/170483](https://doi.org/10.1086/170483)

Wyithe, J. S. B., Turner, E. L., & Spergel, D. N. 2001, *ApJ*, 555, 504, doi: [10.1086/321437](https://doi.org/10.1086/321437)

Yıldırım, A., van den Bosch, R. C. E., van de Ven, G., et al. 2017, *MNRAS*, 468, 4216, doi: [10.1093/mnras/stx732](https://doi.org/10.1093/mnras/stx732)

Zhu, K., Lu, S., Cappellari, M., et al. 2023, *MNRAS*, 522, 6326, doi: [10.1093/mnras/stad1299](https://doi.org/10.1093/mnras/stad1299)

Zhu, K., Lu, S., Cappellari, M., et al. 2024, *MNRAS*, 527, 706, doi: [10.1093/mnras/stad3213](https://doi.org/10.1093/mnras/stad3213)